Compton Scattering and Warm Dense Matter Thermometry

Brian Mattern

A dissertation
submitted in partial fulfillment of the
requirements for the degree of

Doctor of Philosophy

University of Washington

2013

Reading Committee:

Gerald T. Seidler, Chair

George Bertsch

John J. Rehr

Program Authorized to Offer Degree:
UW Physics

University of Washington

Abstract

Compton Scattering and Warm Dense Matter Thermometry

Brian Mattern

Chair of the Supervisory Committee:
Professor Gerald T. Seidler
Physics

The purpose of this dissertation is to consider the level of detail required for proper theoretical description of non-resonant inelastic x-ray scattering (NIXS) experiments from warm dense matter (WDM). These experiments currently provide the primary means of diagnostic thermometry for low-Z elements of interest for inertial confinement fusion. In particular, I focus on the importance of non-perturbative ion-electron interactions and their effect on the NIXS spectrum. To this end, I have extended the real-space electronic structure code `FEFF` to both calculate the valence-electron contribution to the NIXS spectrum and to handle elevated electronic temperature. I have found that the ion-electron interaction, and in particular the constraint of orthogonalization between core and valence wavefunctions results in a significant broadening of the valence-electron NIXS spectrum. This effect, has a similar appearance as increasing both density and temperature in simpler models of the valence-electrons in WDM, and thus significantly affects the accuracy of thermodynamic parameters extracted from experimental data. Additionally, I have also demonstrated improved models for treating the core-shell contribution to the NIXS spectrum.

TABLE OF CONTENTS

LIST OF FIGURES

ACKNOWLEDGMENTS

I would like to express my sincere appreciation to everyone I have had the opportunity to work with and learn from during my time here at the University of Washington. This work would not have been possible without the support and guidance of my advisor Jerry Seidler and our close collaborator, John Rehr. I am extremely thankful to Josh Kas for shedding light on some of the darker corners of the `FEFF` code base, without whom the journey would have been much more perilous. For teaching me the way around a synchrotron, many thanks go to Joe Bradley. Further thanks go to the rest of my fellow graduate students who made the experience both enjoyable and memorable. Finally, and most importantly, I would like to thank my wife, Suzanne and our dear son, Andreas and my parents Mike and Angie for their loving support and understanding.

Chapter 1

INTRODUCTION

In this work, I will discuss the application of non-resonant inelastic x-ray scattering (NIXS) to the diagnostic determination of the thermodynamic state of materials in the *warm dense matter* (WDM) regime. The information about state (e.g, temperature, density, ionization) is primarily contained in the contribution from scattering off of delocalized electrons. I will develop a method of calculating this contribution, known as the Compton profile, using a real-space Green's function approach to the electronic structure. This treatment includes the full non-perturbative effects of the potential landscape in which the electrons live, which I find to have a significant affect on the width and shape of the Compton profile, and thus on the thermodynamic parameters extracted from experimental data.

To begin, it is important to understand the broad context within which this work is contained. Fig. 1.1 shows a map of thermodynamic phase space, adapted from Ref. [210]. Matter density is shown logarithmically along the horizontal axis, with mass density at the bottom and approximate electron density along the top. The vertical axis, gives the logarithmic temperature in units of kelvin on the left and electron volts on the right. Above and to the right of the dashed curve labeled "Pressure = 1 Mbar" is the realm of high-energy-density physics (HEDP), defined as the regime where applied pressures are comparable to the internal energy of room-temperature atoms and molecules[62]. At low densities, the pressure is radiation dominated and thus set by the temperature. As density increases, the thermal pressure of matter become dominant and the boundary slopes downward. As density is increased further, the Fermi-pressure of the electrons reaches 1 Mbar and the curve becomes vertical.

Three additional bounding curves are shown. The first gives a rough separation between ionized and un-ionized matter. For free atoms, ionization sets in when temperatures approach the binding energies of the outermost electrons, ~ 1 eV. As density increases to

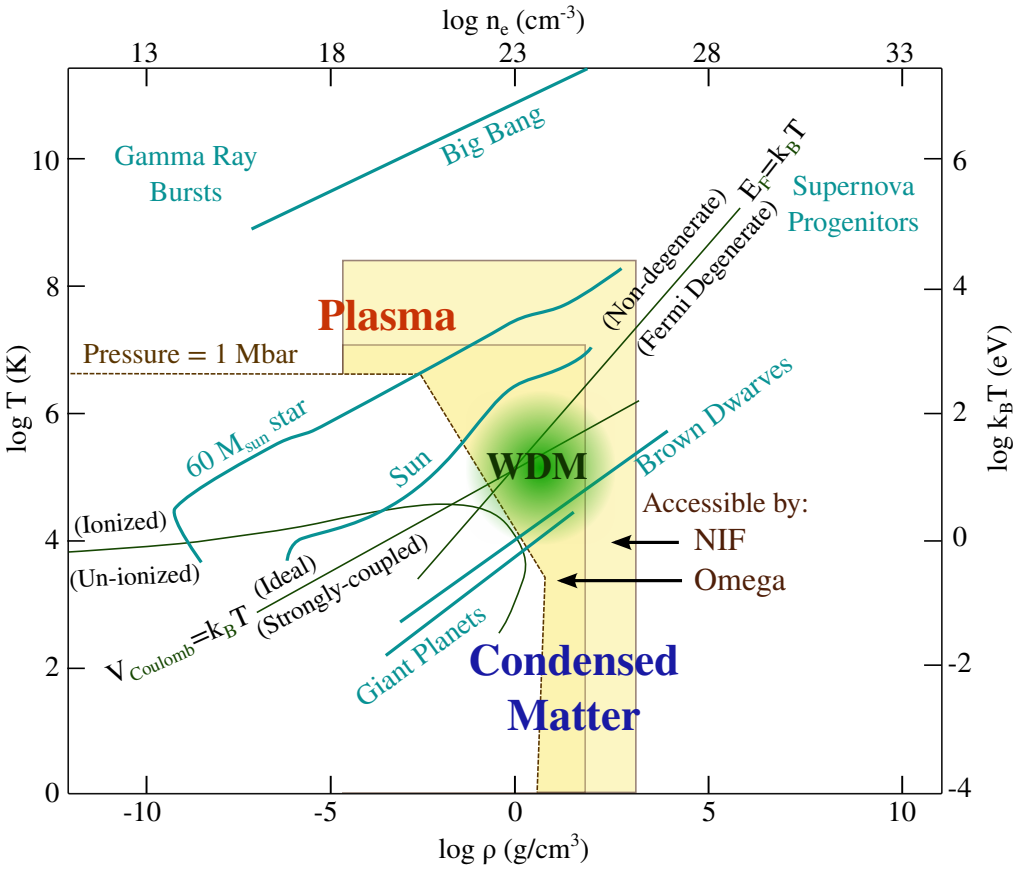

Figure 1.1: The universe, as seen by a high-energy-density physicist. See text for discussion.

~ 1 g/cc, the overlap between Coulomb potentials of neighboring atoms becomes sufficient for the outermost states to delocalize, as in the conduction bands of metals. The next bounding curve is located where the thermal energy $k_B T$ is equal to the average Coulomb interaction between constituent particles V_{Coulomb}. On the high-temperature side, interactions are weak and can either be neglected or treated perturbatively. The final bounding curve is located where the thermal energy is equal to the Fermi energy of the electrons dividing the region where quantum statistics plays an important role from that where it is not.

Far from these boundaries, it is straightforward to define the central, most salient microphysics on which to base fundamental theoretical treatments of matter. First, on the low-density, high-temperature side lies the realm of plasma physics, where classical statistical mechanics is the rule. One need not concern themselves with wavefunctions and quantum statistics is only relevant for the shape of the blackbody spectrum. Interactions between ions and electrons exist only as a weak perturbation to an ideal gas. Second, on the other hand, is the moderately-high-density, low-temperature realm of condensed matter. The story of 20th-century solid state physics shows an almost completely successful, necessarily quantum-mechanical treatment of nearly all thermodynamic and electronic properties This is not to say that all issues of implementation are understood or that all perturbative corrections have been identified, but rather that the overall approach is well-established: the electronic properties of cold, moderately dense matter (on the scale of Fig. 1.1) must be treated by many-body quantum mechanics of the electrons in a potential landscape dominated by electron-ion interactions.

Near the boundaries, however, the dominant microphysics and consequent theoretical approaches is much less clear and a matter of ongoing research[230, 261, 161, 162]. The purpose of this dissertation is to investigate the character of the theoretical treatment needed to describe the electronic properties of matter in the so-called *warm dense matter* (WDM) regime straddling the intersection of the bounding curves in Fig. 1.1. Although the definition of WDM is somewhat loose, the term is typically used to designate matter at solid-like or higher densities with temperatures comparable to the Fermi energy, where matter is partially ionized, yet still at least partially degenerate. As shown in Fig. 1.1, this region

encompasses several astrophysical phenomena, in addition to being a necessary transient in any experiment which produces plasma from the solid state. The latter is particularly important in the context of direct- or indirect-drive laser-driven compression and heating with the goal of obtaining inertially confined fusion[188].

Experiments in the WDM regime are, unfortunately, almost uniquely challenging. Laboratory production of WDM can proceed via several paths at an ever-increasing number of facilities. The dominant method at this time is through laser-shock compression at facilities such as the OMEGA laser at the Lab for Laser Energetics in Rochester, NY, where ramped laser pulses are used to simultaneously heat and compress samples on the nanosecond time scale, resulting in disordered systems that are typically considered to be in local thermal equilibrium[107]. Even higher energy densities are accessible at the National Ignition Facility (NIF) at Livermore National Labs[198]. Alternatively, x-ray free electron lasers (XFELs) such as the Linac Coherent Light Source (LCLS) or the upcoming European XFEL at DESY in Hamburg can been used to rapidly heat the electronic degrees of freedom (on femtosecond time scales) via significant core-shell ionization[200]. In such short-time-scale experiments, one expects that the lattice does not have time to respond, resulting in out-of-equilibrium matter with hot electrons and a cold, ordered lattice. However, there is some experimental evidence that has been taken as indicating rapid lattice melting at fs time-scales[126].

Although methods of producing WDM are now well understood, *characterization* of WDM is much more difficult. Although the bulk of the material is often expected to be in local thermal equilibrium, the production methods typically lead to formation of a hot surface plasma under vastly differing conditions from the bulk. Thus, optical probes are of limited utility due to the high opacity of dense systems. Likewise, at temperatures of a few eV, thermal black-body emission is limited to the surface layer. More penetrating probes, e.g., photons in the x-ray regime, are needed to characterize laboratory produced WDM.

In case where the elements are heavy enough to allow x-ray absorption or emission spectroscopies with photon energies sufficient to give bulk-like information, rich data exists. By rich, I mean having sufficient information content to directly challenge theoretical treatment. This is most clearly the case in the problem of the localization, or lack thereof, of the $3p$ orbital of Al. Fig. 1.2, reproduced from Levy, et al.[185], shows the x-ray absorption

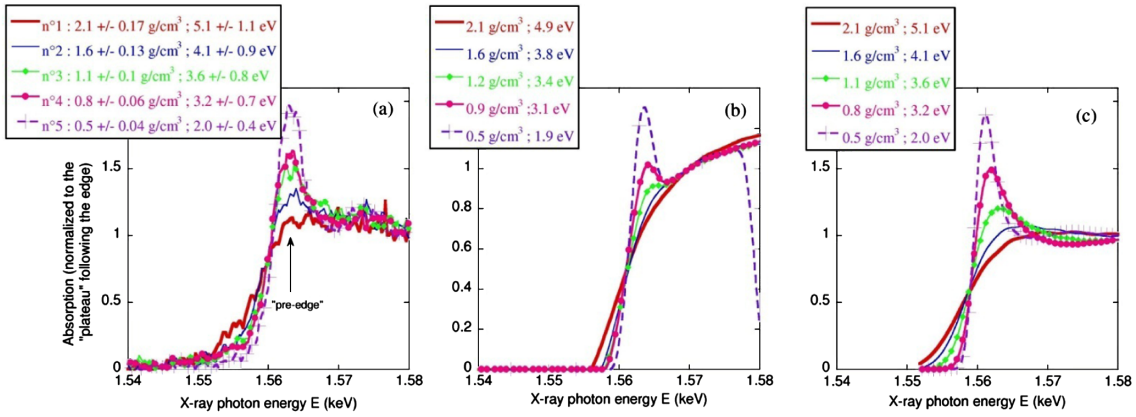

Figure 1.2: X-ray absorption spectra around the Al K edge from laser-shock-compressed Aluminum during expansion (from Levy, et al.[185]). (a) Experimental data. (b) *Ab initio* calculations. (c) Average atom in jellium calculations.

K-edge for expanding laser-shock-compressed Al under varying densities and temperatures (as determined from hydrodynamic simulations). Experimental data are shown in (a), and two theoretical calculations are shown in (b) and (c). The K-edge spectrum measures the unoccupied states of p-character, into which a $1s$ electron can be excited. As density and temperature decrease, the spectrum changes in two ways. First, the slope at the edge increases, as the cutoff in the Fermi distribution becomes sharper. Second, a sharp peak develops (labeled "pre-edge" in the Figure 1.2, more commonly refer to as the "white line"), which is indicative of a localized $3p$ state[38, 29]. At high densities due to overlap of neighboring ionic potentials, the $3p$ states are delocalized, and thus no white line is present in the data. As the system expands, however, the overlap decreases (and thus the barrier between neighboring atoms increases) resulting in a re-localization and increase in white-line intensity. This experiment gives direct observation of the Mott metal-insulator transition in Al[199].

Now, the validity of standard models for describing this phenomenon of *continuum lowering* (the result of which is often called *pressure ionization*) have recently been the subject of investigation and debate. Two recent experiments have come to conflicting conclusions

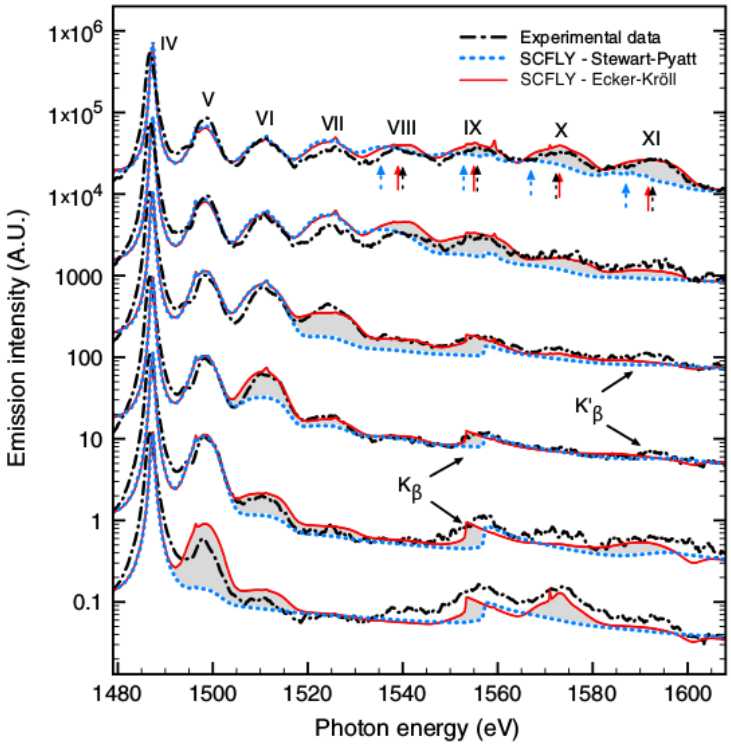

Figure 1.3: X-ray emission spectra from isochorically heated Al[44]. The incident photon energies are 1580, 1600, 1630, 1650, 1720 and 1830 eV from bottom to top. The roman numerals label $3p \rightarrow 1s$ emission from different ionization states.

in this regard. The first experiment, by Ciricosta, et al.[44], used LCLS to measure Kα emission ($2p$ electron filling a $1s$ core-hole) as a function of incident photon energy from Al isochorically heated to $\sim$ 100 eV. In doing so, they were able to directly measure the K-edge ($1s$ binding energy) for several ionization states of Al at ambient density, as shown in Fig. 1.3. The results were found to be in better agreement with a model by Ecker and Kröll (EK)[70] than a competing model by Stewart and Pyatt (SP)[273].

The second experiment, by Hoarty, et al.[135], used laser-driven shocks to compress Al to $\sim 3\times$ ambient density and $T \sim 600$ eV. At these elevated temperatures, ionization is high, with only one or two electrons remaining bound to a typical atom. They found that, the equivalent of $K\beta$ emission ($3p \rightarrow 1s$) from the Hydrogenic and He-like ions, which was

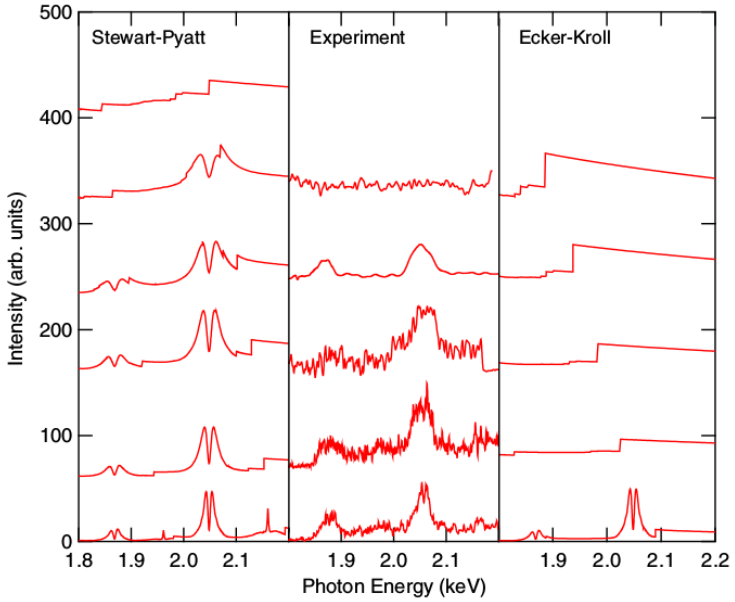

Figure 1.4: X-ray emission spectra from laser-shock-compressed Al.[135]. The curves correspond to mass densities of 1.2, 2.5, 4.4, 5.5 and 9 g/cc from bottom to top. All curves are for T $\sim$ 600 eV.

visible prior to compression, vanished after compression (as shown in Fig. 1.4) due to the $3p$ states becoming delocalized. This density dependence was much better described by the SP model than the EK model.

Note that these two experiments are themselves not logically in conflict, as different aspects of continuum lowering were studied. The first focuses on ionization-state dependence at fixed density and temperature, while the second focused on density dependence at fixed ionization and temperature. It is entirely possible that the two experiments combined simply rule out both EK and SP as accurate models of the ionization potential in warm dense systems. In any case, these examples demonstrate the feasibility of direct x-ray absorption and emission measurements of moderate-Z elements.

The situation is, unfortunately, more difficult for what must be called more important issues: the behavior of lower-Z plasmas, such as those based on Li or H as nuclear fuels, or based on Be or C-H plastic and formed in the early stages of compression in ICF exper-

iments. For such low-Z systems, the core-shell binding energy is too small (10 - 300 eV) for direct absorption or emission spectroscopy to be useful: photons of these energies will neither penetrate into nor escape from the target. Consequently, extensive work has gone into using higher-energy photon spectroscopies, i.e., nonresonant inelastic x-ray scattering (NIXS), generally called x-ray Thomson scattering (XRTS) in the plasma physics community to probe the electronic properties of low-Z WDM. The fact that his x-ray diagnostic, which is presently the leading experimental method being used to extract information about the equation of state of low-Z WDM, is explicitly and directly sensitive to electronic properties of the system then brings us back to the dichotomy of the extreme physical regimes introduced above. Specifically: what level of sophistication of quantum-mechanical treatment in necessary to encompass the dominant microphysics? This is the central question investigated in this dissertation.

With this question in mind, the introduction proceeds in three sections aimed at further motivating the completed research and placing the work into context of the contemporary scientific literature. First, in section 1.1, I review the general theoretical formalism for NIXS. The important conclusion is that NIXS is a direct probe of electronic material properties and that, in some regimes, it has especially straightforward interpretations with respect to the electronic properties of the sample. Next, in section 1.2, I survey the scientific literature by presenting selected results on NIXS/XRTS as applied to low-Z WDM at laser-shock facilities. This section establishes the overlap of pragmatic and theoretical issues: both a correct theoretical understanding of the valence electrons and also a correct theoretical treatment of the core-electron contribution to NIXS, including continuum lowering effects, are needed if the inferred free-electron densities and electronic temperatures are to have any accuracy. Finally, with this context provided, in section 1.3, I outline the remainder of this dissertation and the importance of my results. In particular, I find that existing, commonly-used theoretical treatments for each of the core- and valence-electron contribution to the measured NIXS spectra are substantially incomplete or simply incorrect.

1.1 X-ray Scattering Theory

1.1.1 General Formalism

In an x-ray scattering experiment an incident beam of photons with some incident angular distribution and energy spectrum are scattered resulting in a modified angular distribution and energy spectrum. Typically, the incident photons are well collimated and have a narrow energy bandwidth. Even if this is not the case, we can make use of the superposition principle and consider photons incident along a single path with a well defined energy. We can then consider detecting the intensity scattered into a small solid angle as a function of direction and scattered photon energy. This situation is shown in Fig. 1.5, where the primary kinematic variables are labeled. Here and throughout this document, I will use Hartree atomic units ($\hbar = m_e = 1$). The incident photons have energy ω_1, momentum $\mathbf{k}_1$, and polarization vector ϵ_1. The corresponding quantities for the scattered photons are labeled with the subscript 2. The angle between the incident and scattered momenta in the plane of scattering is labeled θ. The energy transferred from the x-rays into the sample is given by $\omega \equiv \omega_1 - \omega_2$, while the corresponding momentum transfer is $\mathbf{q} \equiv \mathbf{k}_1 - \mathbf{k}_2$. Energy conservation implies that $\omega = E_F - E_I$, where $E_{I,F}$ are the initial and final energies of the sample described by the states $|I\rangle$,$|F\rangle$ respectively.

The relative probability of scattering into a solid angle $d\Omega$ in a narrow energy band of width $d\omega$ about ω_2 is known as the double-differential scattering cross-section (DDSCS) $d^2\sigma/d\Omega d\omega$. Here, we will focus on the non-resonant inelastic x-ray scattering (NIXS) regime, where the incident photon energy is far from any characteristic energies of the sample under study. We will also consider the non-relativistic limit, where $\omega \ll mc^2$. Under these conditions, the DDSCS can be expressed in the first Born approximation as[251]

$$\frac{d^2\sigma}{d\Omega d\omega} = r_0^2 \left(\frac{\omega_2}{\omega_1}\right) |\epsilon_1 \cdot \epsilon_2^*|^2 \sum_{\mathrm{I,F}} g_I \left| \sum_j \langle F| e^{i\mathbf{q}\cdot\mathbf{r}_j} |I\rangle \right|^2 \delta(\omega - E_I - E_F). \tag{1.1}$$

Here, $r_0 \equiv e^2/mc^2$ is the classical electron radius. The index j runs over all individual electrons in the sample, and r_j is the position operator for the jth electron. The factor $g_i = Z^{-1}\exp(-E_I/k_BT)$ is the Boltzmann factor giving a thermal average over the initial

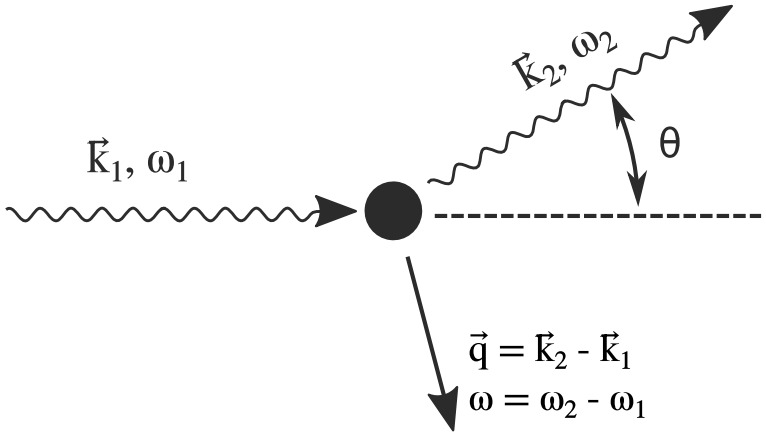

Figure 1.5: Kinematics of x-ray scattering. An incident photon with momentum and energy $\mathbf{k}_1$,ω_1 scatters at an angle θ. The scattered photon has momentum and energy $\mathbf{k}_2$,ω_2. The momentum and energy transferred to the sample are $\mathbf{q}$ and ω respectively.

state.

Eq. 1.1 factors into two quantities which describe different physical aspects. The Thomson scattering cross-section

$$\left(\frac{d\sigma}{d\Omega}\right)_{\mathrm{Th}} \equiv r_0^2 \left(\frac{\omega_2}{\omega_1}\right) |\epsilon_1 \cdot \epsilon_2^*|^2 \tag{1.2}$$

describes the interaction between the probe and a single electron. The sample-dependent properties are then encapsulated in the remain factor, the dynamic structure factor

$$S(\mathbf{q},\omega) \equiv \sum_{\mathrm{I,F}} g_I \left| \sum_j \langle F| e^{i\mathbf{q}\cdot\mathbf{r}_j} |I\rangle \right|^2 \delta(E_F - E_I - \omega). \tag{1.3}$$

Energy conservation is expressed by the final δ-function, while momentum conservation is implicitly given by the matrix elements of the momentum translation operator $\exp(i\mathbf{q}\cdot\mathbf{r}_j)$.

Eq. 1.3 contains both coherent/elastic scattering (for $\omega = 0$) and incoherent / inelastic scattering (for $\omega \neq 0$). For the remainder of this introduction we will be interested only in the incoherent portion of $S(\mathbf{q},\omega)$, which can be further separated into contributions from each of the tightly-bound core electrons and a contribution from the delocalized electrons in the valence/conduction band. In Fig. 1.6, we show experimental data along with theoretical calculations that illustrate this separation.

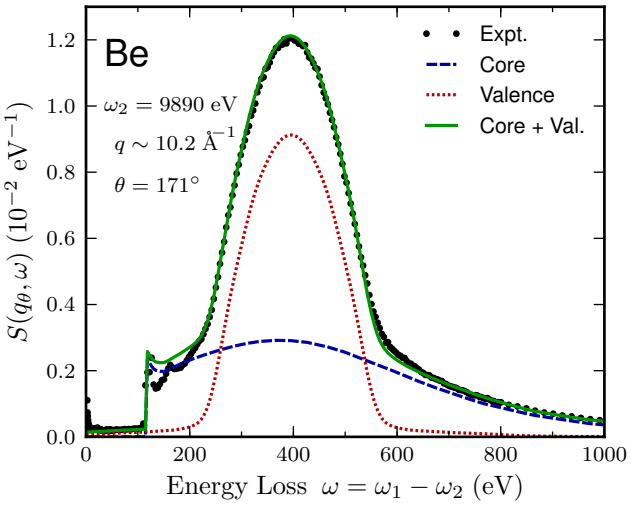

Figure 1.6: Experimental NIXS from polycrystalline Be under ambient conditions. The separate contributions from the tightly bound core electrons and the delocalized valence electrons are shown. The sharp cutoff in the core contribution at $\omega = 112$ eV is due to the binding energy of the $1s$ core electrons, below which there are no available final states to scatter into.

Upon formation of a condensed system, the core states are generally expected to retain their atomic-like character, provided that the overlap of wavefunctions from neighboring atoms is negligible. Theoretical methods for calculating the core contribution to NIXS are described in detail in chapter 7.

The nature of the valence-electron contribution to NIXS, on the other hand, is highly dependent on the magnitude of the momentum transfer which sets the length scale $2\pi/q$ being probed. At small scattering angles, and thus small q, long wavelength, collective excitations are probed. At large scattering angle and thus large q, short length-scale, non-collective physics is probed. In this limit, the interpretation of IXS becomes particularly simple in that the spectrum is directly related to the electronic momentum distribution. We now give a detailed description of this relationship.

1.1.2 Compton Scattering and the Impulse Approximation

Before continuing further, it is useful to consider the much simpler case of x-ray scattering from a single electron. In his seminal 1923 work, Arthur H. Compton had the insight to use simple relativistic kinematics to describe the process. Doing so for the case of an initially stationary electron, one finds

$$\omega_2 = \frac{\omega_1}{1 + \frac{\omega_1}{mc^2}(1 - \cos(\theta))} \tag{1.4}$$

Alternatively, one can use non-relativistic energy and momentum conservation, provided that $\omega_2 - \omega_1 \ll mc^2$ to obtain

$$\omega_{\mathrm{C}} \equiv \omega_2 - \omega_1 = \frac{q^2}{2m} \tag{1.5}$$

for the recoil energy. The magnitude of $\mathbf{q}$ is given by

$$q^2c^2 = \omega_1^2 + \omega_2^2 - 2\omega_1\omega_2(1 - \cos(\theta)). \tag{1.6}$$

We note that the prior two expressions give a quadratic equation for ω_2 as a function of θ, which are accurate to order $(\omega_1/mc^2)^2$.

In early x-ray scattering experiments, it was observed that, in addition to what Compton termed the modified line, an unmodified, elastically scattered line was present. Furthermore,

the modified line was observed to be broader than the unmodified line[48]. In 1925, Jauncey explained both of these effects qualitatively using the Bohr model for the atom[155].

If the scattering electron initially has a momentum $\mathbf{p}$, then one finds from energy and momentum conservation that

$$\omega = \frac{(\mathbf{p}+\mathbf{q})^2}{2m} - \frac{p^2}{2m} = \frac{q^2}{2m} + \frac{\mathbf{p}\cdot\mathbf{q}}{2m}. \tag{1.7}$$

Then, depending on where the electron is in its orbit when the scattering event occurs, the direction of its momentum, and thus its influence on the energy shift changes. Averaging over directions results in a broadening of the modified line. On the other hand, when the initial momentum is directed opposite to $\mathbf{q}$, it is possible for ω to be smaller than the binding energy of the electron. In this case, the electron remains bound and the atom as a whole recoils. Due to the much greater mass of the atom, the recoil energy becomes negligible resulting in the unmodified, elastic peak. The idea that the Compton peak was broadened by the electronic momenta was extended from the Bohr atom to arbitrary momentum distributions by DuMond in 1928[63, 64]. He considered the scattering of Mo Kα x-rays from a Be metal and compared the experimental spectra to Doppler-broadened Compton lines for several different theoretical models of the 2s electrons in Be metal. This comparisonshowed that the Bohr model, a free atom and a classical gas all gave momentum distributions which were too narrow to describe the spectrum. However, a degenerate gas of fermions gave a result of sufficient breadth. This provided some of the first experimental support for Fermi-Dirac statistics. For more details on the early developments, we recommend the excellent review by DuMond[65].

A rigorous theoretical footing for the description of inelastic x-ray scattering in terms of Doppler broadened Compton scattering did not come until 1970, when Eisenberger and Platzman gave a first-principles derivation of this so-called impulse approximation[71]. Here, we follow their derivation closely.

We will start with Eq. (1.3), and for simplicity drop the thermal averaging and consider only a single electron. By expanding the δ-function using the spectral representation

$$\delta(E_F - E_I - \omega) \equiv \frac{1}{2\pi}\int dt\, e^{i(E_F - E_I - \omega)t} \tag{1.8}$$

we find

$$S(\mathbf{q},\omega) = \frac{1}{2\pi}\int dt\, e^{-i\omega t}\sum_F \langle I|\, e^{-iE_F t}e^{-i\mathbf{q}\cdot\mathbf{r}}e^{iE_I t}\,|F\rangle\,\langle F|\, e^{i\mathbf{q}\cdot\mathbf{r}}\,|I\rangle \tag{1.9}$$

$$= \frac{1}{2\pi}\int dt\ \langle I|\, e^{-iHt}e^{-i\mathbf{q}\cdot\mathbf{r}}e^{iHt}e^{i\mathbf{q}\cdot\mathbf{r}}\,|I\rangle\,. \tag{1.10}$$

In the second line, we have made use of the fact that $|I,E\rangle$ are eigenstates of the Hamiltonian H, and the completeness relation $\sum_F |F\rangle\langle F| = 1$.

Now, we make use of the Baker-Campbell-Hausdorff relation to expand

$$e^{iHt} \simeq e^{iH_0 t}e^{iVt}e^{-(1/2)[H_0,V]t^2+\ldots} \tag{1.11}$$

Noting that due to the Fourier transform in Eq. (1.10), only contributions from $t \ll \omega$ will strongly contribute, we can drop the t^2 and higher terms in Eq. (1.11), provided that ω is much larger than any characteristic energies (e.g., binding energies) of the scattering electron.

Then, making use of the fact that the potential V commutes with the position operator, we can rearrange to obtain

$$S(\mathbf{q},\omega) = \frac{1}{2\pi}\int dt\, e^{i\omega t}\,\langle I|\, e^{-iH_0 t}e^{-i\mathbf{q}\cdot\mathbf{r}}e^{iH_0 t}e^{i\mathbf{q}\cdot\mathbf{r}}\,|I\rangle \tag{1.12}$$

$$= \frac{1}{2\pi}\int dt\, e^{i\omega t}\int d^3p\,\langle I|\mathbf{p}\rangle\,\langle\mathbf{p}|\, e^{-iH_0 t}e^{-i\mathbf{q}\cdot\mathbf{r}}e^{iH_0 t}e^{i\mathbf{q}\cdot\mathbf{r}}\,|I\rangle \tag{1.13}$$

$$= \frac{1}{2\pi}\int dt\, e^{i\omega t}\int d^3p\,\langle I|\mathbf{p}\rangle\, e^{-i(p^2/2m)t}e^{i((\mathbf{p}+\mathbf{q})^2/2m)t}\,\langle p|I\rangle \tag{1.14}$$

$$= \int d^3p\rho(\mathbf{p})\delta\left(\frac{q^2}{2m}-\frac{\mathbf{p}\cdot\mathbf{q}}{m}-\omega\right) \tag{1.15}$$

We note in the first line that we have canceled the two factors containing the potential. In the second line we have inserted a complete set of momentum states. In the third line, we use the fact that these are eigenstates of the free Hamiltonian H_0, and that $\exp(i\mathbf{q}\cdot\mathbf{r})\,|\mathbf{p}\rangle = |\mathbf{p}+\mathbf{q}\rangle$ In the final line we once again use Eq. (1.8), and the definition $\rho(p) = |\,\langle p|I\rangle\,|^2$. Eisenberger and Platzman stress that, although the potential appears to have vanished from Eq. (1.15), it still plays the very important role of determining the momentum distribution. Cooper[51] gives a derivation for the multi-electron case. The final result is identical, although an additional constraint arises, namely that $2\pi/q$ is much smaller than the average interparticle spacing.

The integral in Eq. (1.15) counts the relative fraction of electrons with a given projection of momentum onto the direction of momentum transfer. Thus, we see that the interpretation of NIXS as Doppler-broadened Compton scattering is accurate, provided that the momentum- and energy-transfer are larger than any characteristic momenta or energies of the system under consideration.

It is customary to extract the projected momentum distribution from Eq. (1.15) by rewriting the δ-function in terms of the variable $p_q \equiv wm/q - q/2$

$$S(\mathbf{q},\omega) = \frac{m}{q} J(p_q) \tag{1.16}$$

$$J(p_q) = \int d^3p \rho(p) \delta(\mathbf{p}\cdot\hat{\mathbf{q}} - p_q), \tag{1.17}$$

where $J(p_q)$ is known as the *Compton profile* (CP). From Eq. 1.17, it follows immediately that

$$\int J(p_q) dp_q = \int d^3p\ \rho(p) = N, \tag{1.18}$$

where N is the number of electrons in the normalizing volume V.

For the case of an isotropic (or spherically averaged) momentum distribution, $\rho(\mathbf{p}) = \rho(p)$, the angular integral in Eq. (1.17) can be performed to obtain

$$J(p_q) = 2\pi \int_{|p_q|}^{\infty} p\rho(p) dp. \tag{1.19}$$

This form can be inverted to obtain

$$\rho(p) = -\frac{1}{p}\frac{d}{dp_q} J(p_q)\Big|_{p_q=p}. \tag{1.20}$$

Thus, we see that, while in the general case only a projected momentum density is measured, for an isotropic system this determines the complete momentum density.

As an illustrative example, we will consider the case of a non-interacting gas of fermions. At zero temperature, the momentum distribution is given by $\rho(\mathbf{p}) = (2V/(2\pi)^3)\Theta(p_F - p)$, where the Fermi momentum $p_F = (3\pi^2 N/V)^{1/3}$. Fig. 1.7 (a) shows the radial momentum distribution, normalized to the number of electrons per momentum eigenstate $n(p) = ((2\pi)^3/V)\rho(p)$. In panel (b), the occupied Fermi sphere is shown along wit The occupied states in 3d fill the Fermi sphere, shown in panel (b). States in a plane perpendicular to $\hat{\mathbf{q}}$

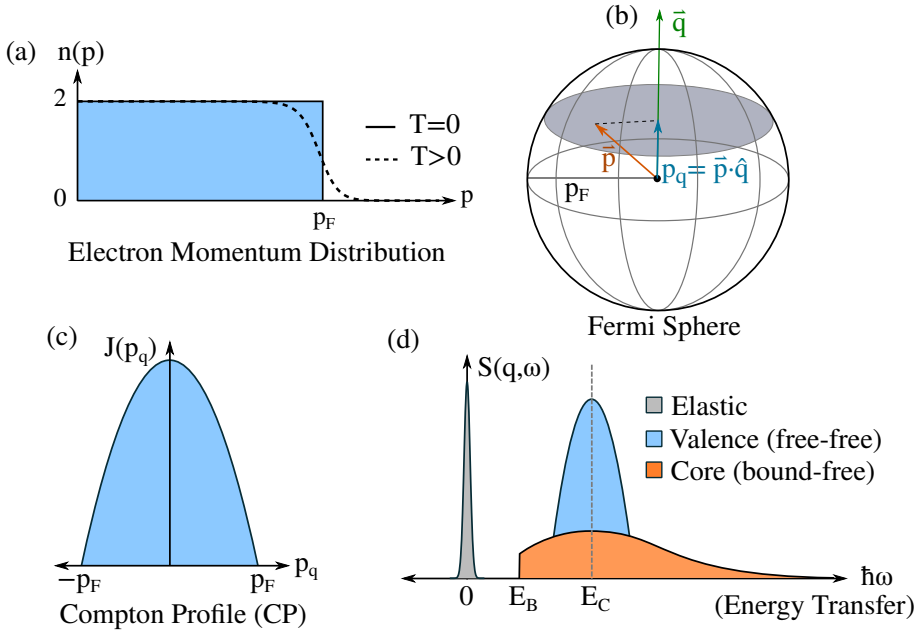

Figure 1.7: Illustration of the impulse approximation for a non-interacting Fermi gas. (a) The radial Fermi distribution. (b) The Fermi sphere. States within the shaded plane have the same projection onto **q**, and thus will scatter with the same energy transfer. (c) The Compton profile. (d) The dynamic structure factor including the contribution from states tightly bound to the ionic cores. The center of the peak is located at the Compton shift E_C. The sharp cutoff at the binding energy E_B is caused by the lack of unoccupied final states to scatter into.

all have the same projection onto **q**, so the area of the shaded intersection with the Fermi sphere as a function of displacement from the origin defines $J(p_q)$ geometrically. Alternatively, using Eq. (1.19), we find

$$J(p_q) = \frac{2}{\pi^2}\left(p_F^2 - p_q^2\right)\Theta(p_F - p)$$

, the truncated upside-down parabola shown in panel (c). Finally, in panel (d) we convert to $S(q,\omega)$ using Eq. 1.17 and include a representative contribution from core electrons.

In Fig. 1.8, we show the density dependence of both the momentum distribution and the CP for a non-interacting Fermi gas at T=0. As density increases, p_F increases and the

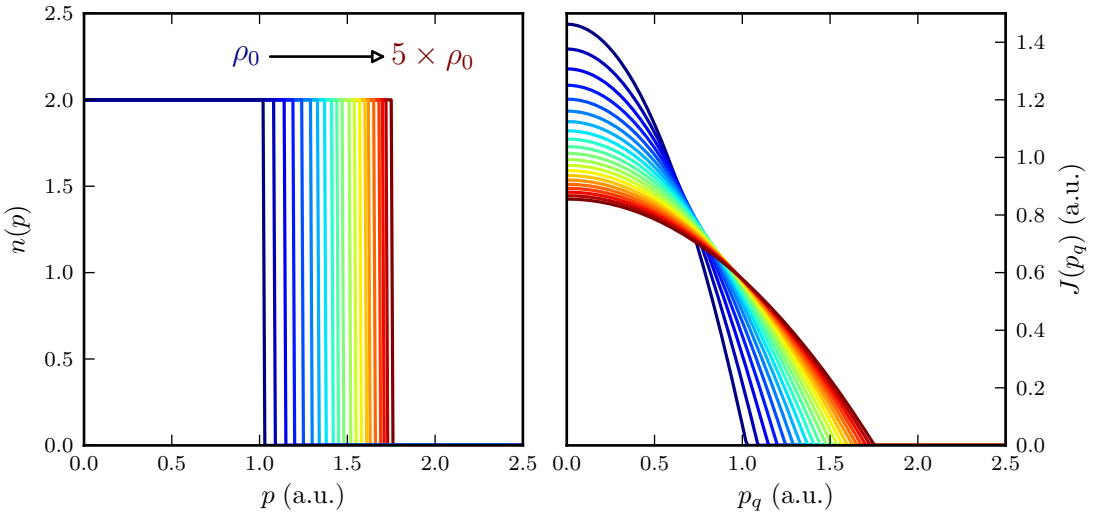

Figure 1.8: Density dependence of the momentum distribution (left) and Compton profile (right) for a non-interacting Fermi gas. The electronic density ranges from the average valence-electron density in ambient Be $\rho_0 = 0.036 a_0^{-3}$ to $5 \times \rho_0$.

CP becomes wider, while retaining its parabolic shape. Since the total integral is fixed (Eq. (1.18)), the peak height decreases.

Generalizing to finite temperature, the momentum density for the non-interacting gas is given by $\rho(p) = (2V/(2\pi)^3) f(p^2/2)$ where the Fermi distribution

$$f(E) = \left[e^{(E-\mu)/k_B T)+1} + 1 \right]^{-1}, \tag{1.21}$$

and the chemical potential is set by particle number conservation

$$N = \int d^3p \, \rho(p). \tag{1.22}$$

In Fig. 1.9, we show the temperature dependence of both the momentum distribution and the CP at fixed density. As temperature is increased, occupation is shifted smoothly from below p_F to above. Likewise, the CP becomes broader, but now departs from the parabolic shape, developing tails.

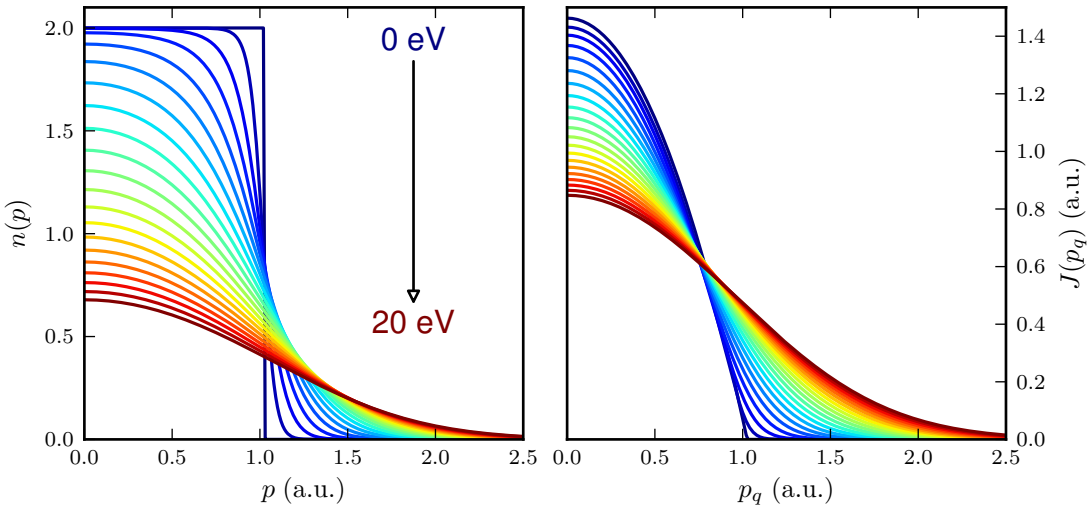

Figure 1.9: Temperature dependence of the momentum distribution (left) and Compton profile (right) for a non-interacting Fermi gas at $T = 0$.

1.1.3 The dynamic structure factor for a dense plasma

The standard starting point for calculating the dynamic structure factor for a dense plasma is the following form, from Chihara[42]

$$S(q,\omega) = |f_I(q) + f_e(q)|^2 S_{\rm ii}(q,\omega) + S_{\rm ff}(q,\omega) + S_{\rm bf}(q,\omega). \tag{1.23}$$

Here, the system is assumed to be isotropic, and so $S(\mathbf{q},\omega)$ depends only on the magnitude q. The first term gives quasi-elastic scattering from electrons surrounding the ions. $S_{\rm ii}$ is the ionic structure factor, f_I is the atomic form factor for bound electrons and f_e is the form factor for the screening cloud of free electrons which surrounds the ion. The free-free contribution $S_{\rm ff}$ contains inelastic scattering off of delocalized electrons and the bound-free term $S_{\rm bf}$ is scattering from tightly-bound core states (with final states in the continuum). Again, we are primarily interested in inelastics scattering, and will focus on the final two terms.

Although for hot plasmas, the bound-free term should be modulated by the ionic motion,

this is a small effect in WDM and is typically ignored[115]. Methods for calculating the bound-free term are discussed in chapter 7.

The free-free contribution $S_{\rm ff}(q,\omega)$ can be obtained using the fluctuation dissipation theorem[178]

$$S(\mathbf{q},\omega) = \frac{\epsilon_0 \hbar q^2}{\pi e^2 n_e} \frac{1}{1-e^{\hbar\omega/k_B T_e}} \mathrm{Im} \frac{1}{\epsilon(\mathbf{q},\omega)}, \tag{1.24}$$

where $\epsilon(\mathbf{q},\omega)$ is the dielectric function. The dielectric function for the WDM system is typically approximated using the *random-phase approximation* (RPA)[27] to ϵ for the *interacting* electron gas.

In some more recent studies, electron-ion interactions are included perturbatively as follows. The primary loss mechanism is assumed to be collisions between ions and electrons, which is incorporated using the Mermin ansatz[195, 107]

$$\begin{aligned} \epsilon(\mathbf{q},\omega) &= 1 + \\ &\frac{(1+i\nu/\omega)(\epsilon^{\rm RPA}(\mathbf{q},\omega+i\nu)-1)}{1+(i\nu/\omega)(\epsilon^{\rm RPA}(\mathbf{q},\omega+i\nu)-1)/(\epsilon^{\rm RPA}(\mathbf{q},0)-1)}. \end{aligned} \tag{1.25}$$

Here, $\nu = \nu(\omega)$ is a dynamic collision frequency, which is calculated in the Born approximation [255, 136, 107].

Now, the Mermin ansatz, while exact in the low-q limit is of questionable applicability at higher-q. In particular, in the non-collective regime, where the IA holds, the NIXS spectrum consists of a Compton peak centered at the Compton shift, $\omega_{\rm C} = q^2/2$. Now, the collision frequency ν takes on a density-dependent, nearly constant value for ω less-than the plasma frequency $\omega_{\rm pl}$. Above $\omega_{\rm pl}$, $\nu(\omega)$ decays to zero (see Fig. 7 of Glenzer and Redmer[107]). So, for $\omega_{\rm C} \gg \omega_{\rm pl}$, we expect $\nu(\omega)$ to be negligible. In this case, Eq. (1.26) reduces to $\epsilon(\mathbf{q},\omega) = \epsilon^{\rm RPA}(\mathbf{q},\omega)$. Thus, in the high-$q$ limit, the BMA approach reduces to simply using the RPA, which amounts to neglecting even the perturbative effects of the ionic potentials.

Furthermore, although this general response-function treatment should be reasonably accurate at lower momentum transfers, it is unclear whether the first-Born approximation is adequate at the solid-like (and higher) densities typical of WDM. An improved collision frequency calculated from projector-augmented wave (PAW) based MD-DFT simulations show a significant shift in the plasmon peak location and shape compared to the predictions of the BMA[220].

1.2 Experimental NIXS studies of WDM

The application of inelastic x-ray scattering as a diagnostic measurement of the thermodynamic state of WDM was first demonstrated by Glenzer, et al.[103], where the technique was termed *x-ray Thomson scattering* in analogy with the use of optical-Thomson scattering as a diagnostic in dilute plasmas [257]. In this pioneering experiment, non-collective (high-q) data from laser-heated Be was collected and analyzed by fitting the Compton peak using the RPA. This has been reproduced in Fig. 1.10. The peaks at 4.75 and 4.92 keV are the incident probe spectrum (He-α and Ly-α emission from a Ti disk plasma). The broad shoulder on the low-energy side is the downshifted Compton peak. The elastic lineshape was determined by directly measuring the source spectrum. The valence-electron contribution was calculated using the RPA and the core was (incorrectly) assumed to be a weak background and was neglected. Although the quantitative accuracy of this analysis is limited, the broadening of the inelastic spectrum upon heating and compressing is clearly noticeable in the data demonstrating at least the feasibility of NIXS for WDM thermometry.

This initial demonstration was followed by a series of NIXS studies of Be[181, 173, 96] and CH plastic[173, 92], both of interest as ablator materials for ICF.

We will now show representative data from one of these studies and give an overview of how various pieces of information are encoded in the inelastic spectrum

Fig. 1.11, reproduced from Kritcher, et al.[173], shows experimental NIXS data (black lines) collected from laser-shock-compressed Be at four different time delays between the heater pulse and the probe pulse. The peak from 8900 - 9050 eV is the elastically scattered source (Zn He-α emission). The red curves are best-fit theoretical calculations performed using the `XRTS` software package of Gregori, et al. [115, 114, 116, 107].

I have repeated these calculations in order to separate the individual contributions from the core and valence electrons, shown in Fig. 1.13 for the 3.9-ns data. The core contribution was calculated using the plane-wave form-factor approximation of Schumacher, et al.[252] with the Stewart-Pyatt continuum-lowering model[273]. The valence was calculated using the RPA. All curves have been broadened by the lineshape labeled "Source"[172].

The calculations are parameterized by electron density n_e, electron temperature T and

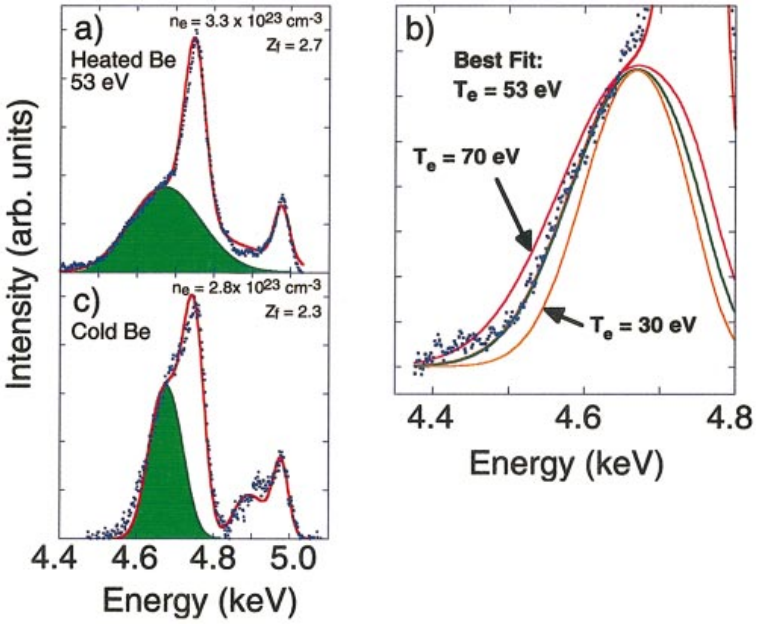

Figure 1.10: X-ray scattering data from laser heated Be[103]. The inelastic scattering peak significantly broadens upon heating.

ionization state Z_f (i.e., the number of free/delocalized electrons). Additionally, the data is known only in relative units, so an overall amplitude remains as a free parameter.

The ionization state can, in principle, be determined from the relative intensities of the core and valence contributions (using the Bethe f-sum rule[151]). The electron density and temperature are then determined by the width and shape of the valence-electron contribution. However, the situation is complicated somewhat by the lack of reliable modeling for continuum lowering which determines the location of the edge-step in the core profile.

The normalized RMS deviation between experiment and theory for calculations at fixed ionization $Z_f = 2$, reproduced from Kritcher, et al.[173], is shown in Fig. 1.12a, and representative fits along the low-energy tail are shown in Fig. 1.12b. The reported statistical errors for the best-fit values in this work are $\sim 20\%$ due to the large covariance between density and temperature (indicated by the elongated elliptical shape of the contours). This is particularly noticeable in panel (d), where the covariance is broken only by the low-energy

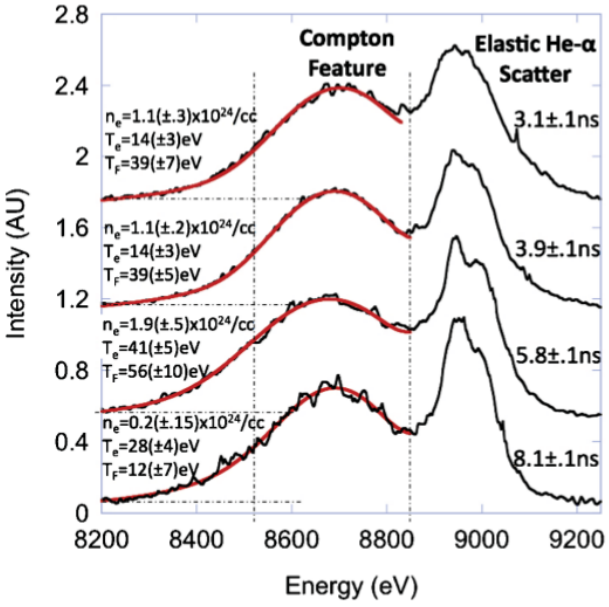

Figure 1.11: NIXS data from laser-shock-compressed Be[173] (black lines) at varying times during compression. Theoretical best fits are shown in red and used to extract electronic densities n_e and temperatures T.

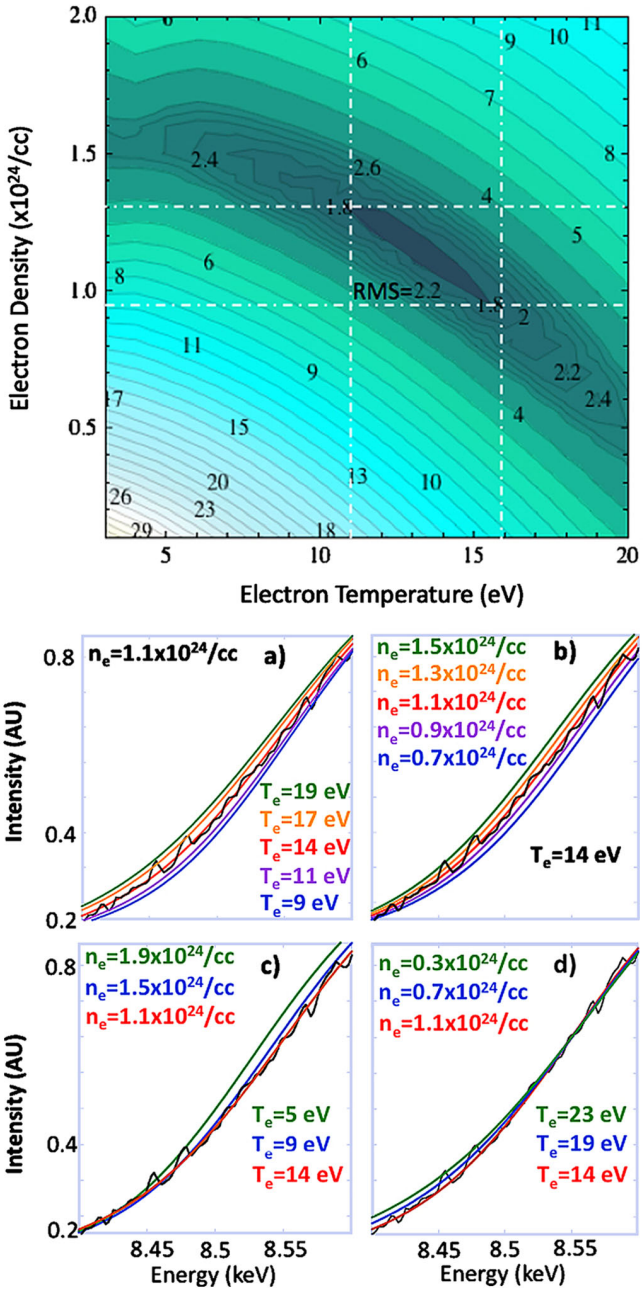

Figure 1.12: Top panel: RMS deviation between fits and 3.9-ns experimental data. Bottom panel: Detail of low-energy wing demonstrating quality of fits.

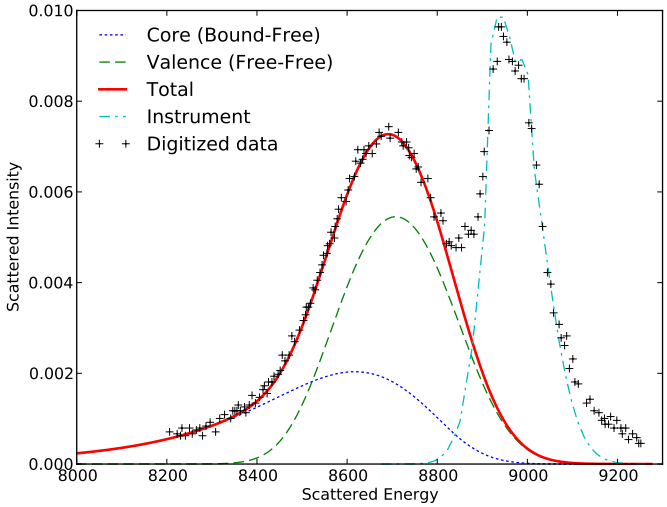

Figure 1.13: Core- and valence-electron contributions to the theoretical NIXS spectrum calculated using the `XRTS` package and overlayed on the 3.9-ns data digitized from Fig. 1.11. The total theoretical spectrum is identical to the best-fit curve shown in the previous figure.

tail. The variation of this tail is primarily due to the density-dependence of continuum lowering in the core-shell model.

1.3 Outline of the dissertation

The validity of thermodynamic state variables extracted from the fitting procedure described in the previous section is dependent upon the accuracy of the models used for each of the contributions to the NIXS spectrum. Agreement between parameterized models and low-resolution experimental data (for some value of the parameters) cannot by itself be taken as validation of model accuracy. Indeed, as I show in the remainder of this work, significant shortcomings exist in the modeling of both contributions. First, treatments of valence electrons which ignore non-perturbative effects of the ion-electron interaction, such as orthogonality between core and valence wavefunctions significantly underestimate the width of the valence peak. Second, the plane-wave form-factor model used for the core is simply unjustified theoretically and is in gross disagreement with high-resolution

experimental data taken under ambient conditions. We note that both of these limitations are due to the same conceptual error: the use of plane waves for the valence states.

In dense systems, it is essential to include the non-perturbative modifications of the valence-state wavefunctions caused by the presence of strong ionic potentials. In order to study this non-perturbative effect of ionic potentials on the valence-electron contribution to NIXS, I have extended the `FEFF` condensed-phase electronic structure code to first calculate Compton scattering spectra and to handle elevated electronic temperatures. In Chapter 2, I give an overview of the `FEFF` code and the techniques used to calculate the real-space Green's function. In Chapter 3, I describe the implementation of Compton scattering calculations and provide comparison with high-resolution synchrotron data and alternative theoretical methods. In Chapter 4, I describe the extensions necessary to handle elevated electronic temperatures. In Chapter 5, I use a simple one-dimensional orthogonalized plane-wave model to explore the qualitative effects of orthogonalization between core and valence states on the electronic momentum distribution. In Chapter 6, I present a study of the density dependence of the Compton profile, in which I find that the non-perturbative ion-electron interaction has a dramatic effect on the width of the Compton profile.

In Chapter 7, I give an overview of theoretical models used to calculate the core-electron contribution to NIXS. Here, I show that the plane-wave form-factor model that is used in NIXS studies of WDM is incorrect and provide alternatives. In Chapter 8, I further discuss issues with the theoretical formalism used in NIXS studies of WDM and the resulting systematic errors. In chapter 9, I give conclusions and future directions for this research.

I have also included in an appendix, unrelated work on instrumental design of a portable, miniature 3-d printed plastic x-ray emission spectrometer.

Chapter 2

FEFF: CALCULATING THE REAL-SPACE GREEN'S FUNCTION

In this chapter, we give a somewhat concise summary of the structure and methodology used by the `FEFF` x-ray scattering code to calculate the Real-Space Green's function. For further details of the the theory behind `FEFF` , we refer the reader to the manual[1], prior theses[5, 223], and the large body of published articles.

`FEFF` allows one to calculate a variety of spectroscopic quantities including x-ray absorption spectra (XAS), both near-edge (XANES) and the oscillatory extended fine-structure (EXAFS), x-ray emission spectra (XES), non-resonant inelastic x-ray scattering (NIXS) from both core and valence electrons. The unifying object, from which these quantities are calculated, is the single-particle real-space Green's function (RSGF) $G(\mathbf{r}, \mathbf{r}'; E)$, which is the Fourier-transform with respect to time of $G(\mathbf{r}, \mathbf{r}'; t, t')$. This latter form of the Green's function gives relative probability for an electron to propagate from $\mathbf{r}$ at time t to $\mathbf{r}'$ at time t'. We here give a practical, constructive description of the methods used by `FEFF` to calculate the RSGF.

We first discuss the primary approximations. The first, implied by the use of the single-particle Green's function, is the independent particle-approximation: it is assumed that single-particle solutions to an effective Hamiltonian provide a good representation of the many-body state. Spectroscopic quantities are then calculated from transition rates, as given by Fermi's golden rule[232]. Inter-particle interactions are handled via an exchange-correlation potential in the local density approximation (LDA)[168, 17]. Finally, and perhaps most importantly, the potentials are treated using a spherically-average muffin tin approximation. In the muffin-tin approximation, the potential about each atomic site is spherically averaged. In the interstitial regions (outside of some prescribed muffin-tin radius), the potential is approximated as a constant.

The calculation begins with the specification of a cluster of atoms, each identified by

atomic number, spatial coordinates. The `ATOMS` program[228], or its online version[229] can be used to generate the cluster specification for crystalline systems. A Dirac-Fock (i.e., relativistic generalization of Hartree-Fock) solver is used to determine the atomic orbitals for each species.[6] Electronic densities are calculated from the occupied atomic orbitals and then overlapped for all atoms in the cluster. After spherically averaging the densities within each muffin tin site, the radius of a sphere that contains a number of electrons equal to the atomic number is calculated. This radius of charge neutrality is known as the Norman radius. Next, potentials (including both direct Coulomb and LDA-based exchange/correlation) are constructed from the spherically-averaged density. Numerical solutions to the Dirac equation are calculated from the potentials and partial-wave phase shifts are determined by matching onto free-particle states (i.e., spherical Bessel functions) at the muffin-tin boundary. The Green's function is calculated using a multiple-scattering expansion which sums over all scattering paths in the cluster, using the free Green's function to propagate between sites and the phase-shifts to encapsulate the effects of scattering at each site. An updated density is given by the imaginary part of the Green's function integrated over occupied states. This procedure is iterated until convergence is obtained, a process termed the *self consistent field* (SCF) loop.

The site and angular-momentum expansion of the Green's function is[224]

$$\begin{aligned} G(\mathbf{r},\mathbf{r}',E) = \quad & -2k\Big[\delta_{n,n'}\sum_{L} H^E_{Ln}(\mathbf{r}_>)\bar{R}^E_{Ln'}(\mathbf{r}_<) \\ & +\sum_{L,L'} R^E_{Ln}(\mathbf{r}_n)e^{i\delta_{Ln}}\, g^E_{Ln,L'n'}\, e^{i\delta_{L'n'}}\bar{R}^E_{L'n'}(\mathbf{r}'_{n'})\Big]. \end{aligned} \tag{2.1}$$

The indices n and n' label the atomic sites nearest $\mathbf{r}$ and $\mathbf{r}'$, and $\mathbf{r}_n \equiv \mathbf{r} - \mathbf{R}_n$, where $\mathbf{r}_n$ is the center of the nth site. $R^E_{Ln}(\mathbf{r}) = i^l R^E_{Ln}(r)Y_L(\hat{\mathbf{r}})$ is the regular solution at site n with angular momentum L and energy E. $H^E = N^E - iR^E$ where N^E is the irregular solution. The overbar denotes complex conjugation of all parts except for the radial function, e.g., $\bar{R}^E_{Ln}(\mathbf{r}) = (-i)^l R^E_{Ln}(r)Y^*_L(\hat{\mathbf{r}})$. The partial-wave scattering phase shifts are denoted by δ_{Ln} and $g^E_{Ln,L'n'}$ is the full multiple scattering (FMS) matrix. The FMS matrix can be

expanded[5] as

$$
\begin{aligned}
g^E_{Ln,L'n'} &= \sum_{n_1,L_1} G^0_{Ln,L_1n_1} t_{L_1n_1} G^0_{L_1n_1,L'n'} && (2.2)\\
&+ \sum_{n_1,L_1}\sum_{n_2,L_2} G^0_{Ln,L_1n_1} t_{L_1n_1} G^0_{L_1n_1,L_2n_2} t_{L_2n_2} G^0_{L_2n_2,L'n'} && (2.3)\\
&+ \cdots && (2.4)
\end{aligned}
$$

Here, $G^0_{Ln,L'n'} = (1-\delta n, n')G^0_{L,L'}(\mathbf{R_n} - R_{n'})$ is a two-center free-propogator and $t_{Ln} = \exp(i\delta_{Ln})\sin\delta_{Ln}$. For a finite-sized cluster, this expansion can be summed to infinite order to obtain (dropping indices for clarity)

$$g = G^0(1 - tG^0)^-1, \tag{2.5}$$

which can be calculated by a single matrix inversion.

From the Green's function, we can define a density matrix

$$\rho(\mathbf{r},\mathbf{r}';E) = -\frac{1}{\pi}\,\mathrm{Im}\,G(\mathbf{r},\mathbf{r}';E), \tag{2.6}$$

. Integrating this over occupied states gives the real-space density matrix

$$\rho(\mathbf{r},\mathbf{r}') = \int_{\mathrm{occ}} \rho(\mathbf{r},\mathbf{r}';E)dE. \tag{2.7}$$

The electronic density is then given by the diagonal portion of the real-space density matrix

$$\rho(\mathbf{r}) = \rho(\mathbf{r},\mathbf{r}) \tag{2.8}$$

Alternatively, integrating the energy-dependent density matrix over the Norman sphere gives a local density of states (LDOS)

$$\rho_i(E) = \int_{|\mathbf{r}-\mathbf{R}_i|<R_{\mathrm{nrm}}} \rho(\mathbf{r},\mathbf{r},E)d^3r \tag{2.9}$$

At zero temperature, the occupied states are those with $E < E_F$. The Fermi level, E_F is determined by the constraint of charge neutrality

$$N = \sum_i \int_{E_C}^{E_F} \rho_i(E)dE. \tag{2.10}$$

In practice, the deeply-bound core states are frozen in their atomic form, and only the valence electronic properties are calculated self-consistently. The lower bound in Eq. (2.10) is a core-valence separation energy E_C. N is then the total number of valence electrons.

We note that, as a matter of practicality, due to the presence of poles just below the real energy-axis, integrals over $\rho(E)$ are typically computationally much less expensive if performed along a contour with a sizable imaginary part. In Fig. 2.1 we show an example of the LDOS for Be. Along the black integration contour, the integrand is much smoother, thus requiring fewer samples.

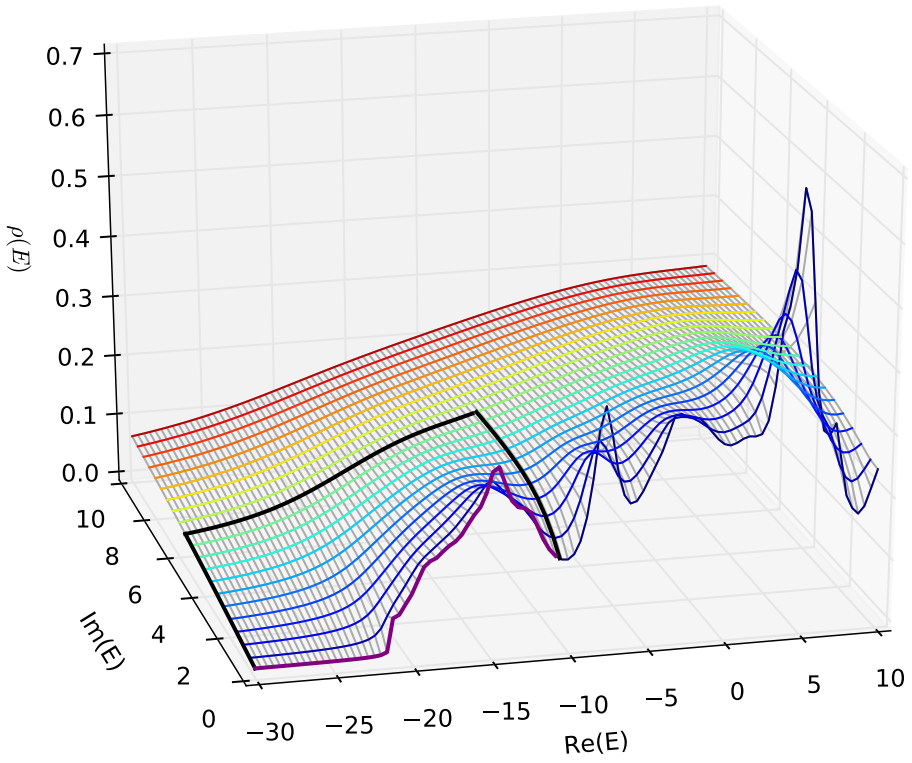

Figure 2.1: In the complex plane, the density of states $\rho(E)$ (shown here for hcp Be) is much smoother at energies with a finite imaginary part than along the real axis. Using the black integration contour requires many fewer samples of the integrand than would be required to integrate along the real axis.

Chapter 3

REAL-SPACE GREEN'S FUNCTION CALCULATIONS OF COMPTON PROFILES

(*Originally published as:* B. A. Mattern, G. T. Seidler, J. J. Kas, J. I. Pacold, and J. J. Rehr, Phys. Rev. B **85**, 115135 (2012).)

We report development of a first-principles, real-space Green's function method for calculation of Compton profiles in the impulse approximation. For crystalline Be, we find excellent agreement with prior theoretical treatments requiring periodicity; with prior experimental measurements of the Compton profile; and with new measurements of the dynamical structure factor via nonresonant inelastic x-ray scattering (often also called x-ray Thomson scattering in the plasma physics community). We also find good agreement with prior experimental results for the Compton profile of Cu. This approach can be extended to disordered and very high-temperature systems, such as 'warm dense matter', where theories presently used for the interpretation of inelastic x-ray scattering include condensed phase effects only at a perturbative level.

3.1 Introduction

Non-resonant inelastic x-ray scattering[59] (NIXS), often also called x-ray Thomson scattering (XRTS) in the plasma physics community, has long been used as a probe of material properties. For example, the Compton scattering cross-section, which is the large energy- and momentum-transfer limit of NIXS, was used in the earliest demonstrations of the particulate character of photons[47] and of Fermi-Dirac statistics.[68] Recently NIXS has seen a steady renaissance thanks to the development of third generation x-ray light sources and associated specialized x-ray spectrometers.[274, 246, 84, 281] Recent applications address many forefront issues in condensed matter physics,[247, 16] subtle questions of bonding in chemical physics,[15, 122, 123] solvation in mixtures,[160] and long-standing problems in quantum scattering theory.[33] Because NIXS makes possible studies of low-Z

edges without high-vacuum techniques, it provides an attractive alternative to and extension of traditional x-ray absorption spectroscopies.[30, 35, 79, 82, 90, 111, 250, 263, 23, 292, 291, 49, 80, 127, 118, 124, 171, 87, 39, 264, 12, 24, 21, 77] More recently, NIXS experiments have yet another venue. High-power laser facilities have created a new application of NIXS, wherein laser-pumped x-ray backlighter sources allow snapshot determinations of the state variables (density and temperature) of so-called 'warm dense matter' (WDM).[60, 76, 103, 108, 102, 105, 176, 104, 182, 99] Our goal in this work is to develop a quantitative treatment of the valence contribution to NIXS that is applicable in these various cases.

The wide parameter space of kinematic variables and initial states requires several different theoretical treatments of NIXS. The treatment of semi-core and core levels has been solved at essentially the same level of detail as x-ray absorption fine structure and with similar tools,[263, 127, 264, 118] whereas the theoretical treatment of NIXS involving valence excitations is still evolving. The difficulties in the latter case come from a significant sensitivity to the atomic and molecular potentials.[122, 207, 208, 123, 31] Hence they depend on an underlying conceptual issue: whether the scattering for given experimental conditions may be treated as nearly single-particle like, or collective, or requiring a more sophisticated treatment of many-body effects including thermodynamic considerations.[108, 105, 95, 97, 74, 230, 40] Such issues are central to NIXS studies of the state variables of WDM.[108]. The WDM sample has solid-like or sometimes higher densities but exists at temperatures that can be well in excess of the Fermi energy, and sometimes in excess of semi-core and eventually core-level ionization energies. These conditions can be generated at large-scale optical laser facilities such as the Laboratory for Laser Energetics (LLE)[60, 103, 102, 105, 104] or the National Ignition Facility (NIF),[198] in addition to being possible through direct, ultrafast x-ray stimulation at x-ray free-electron laser (XFEL) facilities such as the Free-Electron Laser in Hamburg (FLASH) and the Linac Coherent Light Source (LCLS).[201, 277, 278, 286, 284]

A first-principles theoretical treatment of NIXS for WDM must include a self-consistent determination of atomic potentials and ionization levels for a given range of state variables, while also being compatible with high-densities and varying degrees of disorder in atomic

positions. Our purpose here is to demonstrate an important first step in the development of such a theoretical treatment. More specifically, we aim to calculate the valence electron Compton profile in the impulse approximation using an extension of the real-space electronic structure and spectroscopy code `FEFF` .[232] This technique is quite appropriate for these studies since it does not require or depend on periodicity, and is thus applicable to aperiodic and disordered systems. However, we first present prototypical calculations and experimental results for cold, crystalline Be which serves as a well characterized test case.[141, 269, 143, 182] This application also serves as an anchoring reference system that validates and quantifies both our theoretical approach and implementation: indeed we demonstrate excellent agreement with experiment and with prior momentum-space methods designed for periodic structures. Similar agreement is found with experimental results for fcc Cu.

With this foundation, we can then consider applying the method to disordered and higher-temperature systems. Both the traditional condensed matter and the WDM communities have invested effort in understanding thermal effects in NIXS. In the former, comparison of empirical modelling of thermal effects and experimental data up to $\sim$ 800 K (i.e., $k_BT \sim 0.07$ eV) shows that the dominant source of thermal effects on the Compton profile is indirect, arising from the thermally-induced change of density of the simple metals investigated[268, 143]. Thermally-induced disorder is less important and the most direct thermal effect, smearing of the Fermi function or other reorganizations of the valence electron wavefunctions, is negligible because of the metallic nature of the systems studied and the low temperatures relative to the structure in the unoccupied density of states. In the WDM context, on the other hand, density and more direct thermal effects play a more equal role. Existing methods for calculation of NIXS spectra in WDM treat the valence electrons as fully ionized and include only spherically averaged collisional effects from the ionic cores.[41, 43, 136, 108] An improved theoretical treatment will, at a minimum, shed light on the accuracy of mean-field treatments, and may have direct impact on ongoing studies of WDM in relevant geophysical and astrophysical conditions,[198, 235] in inertial confinement fusion studies,[198] or in the unique nearly-ordered WDM states that can be achieved with XFEL illumination.[201, 286]

The remainder of this article is organized as follows: In Section 3.2, we survey the theoretical description of inelastic x-ray scattering. We then specialize to the high momentum-transfer regime in which the Impulse Approximation (IA) applies. It is in this regime that the NIXS spectrum is most clearly understood in terms of the Compton profile, which is directly related to the electronic momentum distribution. Here, we provide experimental data that illustrates the cross-over from low momentum-transfer, where collective excitations are visible, to high momentum transfer, where the spectrum is dominated by the Compton peak. Next, we detail how the electronic momentum density can be obtained from the real-space Green's function (RSGF) in the muffin-tin approximation. Section 3.3 contains details on the implementation of this theoretical framework. In Section 3.4, as demonstration of the technique, we present detailed results for ordered Be metal and give a comparison with both experimental data and momentum-space Koringa-Kohn-Rostocker[169, 167] (KKR) calculations. Although the real-space calculation is limited in momentum resolution by the size of the included cluster, we find very good agreement between with real-space calculation, experimental data taken at a similar momentum resolution, and the broadened KKR calculation. We next compare RSGF calculation of the valence Compton profile for Cu to experiment and prior KKR calculations, finding similarly good agreement. Next, in Section 3.4.2, we compare theoretical RSGF calculations of NIXS spectra with experimental data taken at lower momentum transfer, where the IA no longer holds for the core electrons. In Section 3.4.3, we briefly discuss the benefits of this approach compared to existing methods for treating NIXS from WDM. We then outline the steps we feel would be necessary to extend this work to these higher temperature, disordered systems. Finally, Section 3.5 contains a summary and conclusions.

3.2 Theory

3.2.1 Nonresonant Inelastic X-ray Scattering

In this work, we consider an experiment in which a narrow-bandwidth beam of X rays is incident on a sample and the intensity of scattered radiation is measured as a function of energy and scattering angle. This two-photon process is described by a double-differential

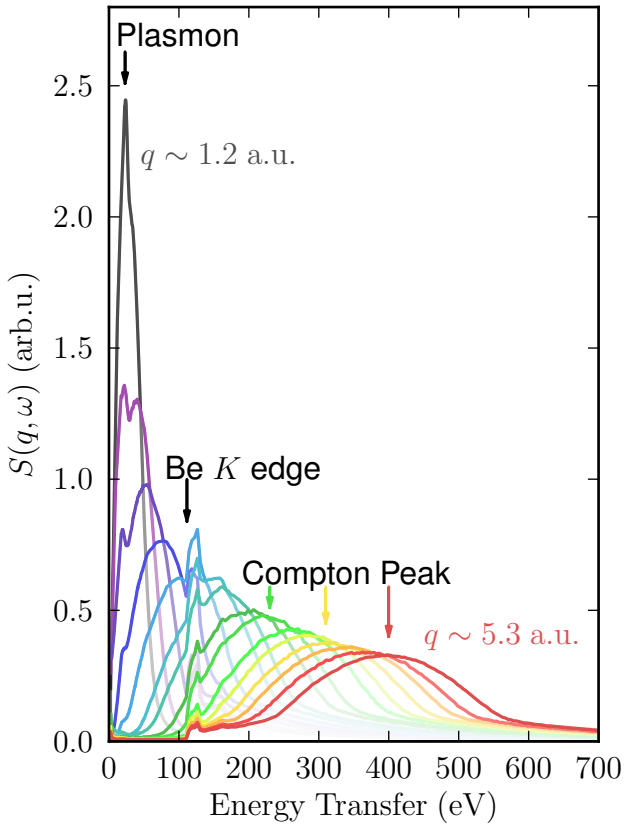

Figure 3.1: (Color online.) Experimental $S(q, \omega)$ for polycrystalline Be taken at 15 different fixed scattering angles. The average momentum transfer q for lowest and highest scattering angles is labeled. Features visible in the data are marked, including the collective plasmon excitation at smaller energy transfers, the Be K-absorption edge at 112 eV, and the Compton scattering peak, which disperses with q.

scattering cross section (DDSCS) $d^2\sigma/d\Omega d\omega_2(\mathbf{q},\omega)$, where Ω is the detected solid angle, ω_2 is the detected photon energy, and $\mathbf{q}$ and ω are the momentum and energy transferred to the sample in the scattering process. We will furthermore focus on the nonresonant inelastic x-ray scattering (NIXS) regime, in which the incident photon energy ω_1 is far from any electron binding energies in the sample. In this regime the dominant contribution to the DDSCS comes from the A^2 term in the interaction Hamiltonian at first order in perturbation theory. For $\hbar\omega$ well below the electron mass, where the non-relativistic limit applies, the DDSCS is given by[52]

$$\frac{d^2\sigma}{d\Omega d\omega_2} = \left(\frac{d\sigma}{d\Omega}\right)_{\mathrm{Th}} S(\mathbf{q},\omega). \tag{3.1}$$

This has been factored into the probe-specific Thomson scattering cross section

$$\left(\frac{d\sigma}{d\Omega}\right)_{\mathrm{Th}} = \frac{\omega_2}{\omega_1} r_0^2 (\hat{\epsilon}_1 \cdot \hat{\epsilon}_2^*)^2, \tag{3.2}$$

and the sample-specific dynamic structure factor

$$S(\mathbf{q},\omega) = \sum_F \left| \langle F| \sum_j \exp(i\mathbf{q}\cdot\mathbf{r}_j) |I\rangle \right|^2 \delta(E_F - E_I - \hbar\omega). \tag{3.3}$$

Here, $r_0 = e^2/mc^2$ is the classical electron radius and $\hat{\epsilon}_{1,2}$ are incoming and outgoing photon polarizations. I and F are initial and final states of the sample, with energies E_I and E_F, respectively, and $\mathbf{r}_j$ is the position operator for the jth electron.

The physical information in the dynamic structure factor depends on the regime of $\mathbf{q}$ and ω. For example, by expanding the exponential transition operator, one sees that at low q, this reduces to a dipole operator. In this limit, the NIXS spectrum is very similar to an x-ray absorption spectrum, and thus contains information about the unoccupied density of states.[24, 250] Here, we will instead be primarily interested in the regime of larger q and ω, in which the dynamic structure factor provides information about the ground state electronic momentum density. This will be described in the following Section.

First, however, to provide illustrative context, we present in Fig. 3.1 experimental NIXS data for polycrystalline Be taken at several different momentum transfers. We defer details of the experimental setup and data processing to Section 3.4.2. Two sharp features are visible: the plasmon excitation at 25 eV and the Be K edge at 111.5 eV. Although very

strong at low q, the collective plasmon peak quickly dies off as q is increased, indicating the onset of the single-particle excitation regime. Our focus in this work will be on the broad Compton peak, which disperses and broadens as q is increased. This latter behavior is most easily understood in terms of the Impulse Approximation, to which we now turn.

3.2.2 Impulse Approximation

For large energy transfer relative to the binding energy of an electron, and for large momentum transfer relative to the inverse electronic orbital size, Eisenberger and Platzman showed that, to a very good approximation, the NIXS from that electron can be described as Doppler-broadened Compton scattering. [72] In this approximation, known as the Impulse Approximation (IA), the single-electron potential before and after scattering cancels in the evaluation of the dynamic structure factor $S(\mathbf{q},\omega)$. The potential plays the simple role of determining the momentum distribution of the electronic ground state, and consequently the shape of the Doppler broadened peak. In other words, the IA assumes that the photon-electron interaction occurs fast enough that the potential felt by the electron is identical before and after the interaction. Thus, energy conservation implies that

$$\hbar\omega = E_f - E_i = \frac{\hbar^2 q^2}{2m} + \frac{\hbar \mathbf{p}\cdot\mathbf{q}}{m}, \tag{3.4}$$

where $\mathbf{p}$ is the electron's momentum. This result is identical to that for classical Compton scattering of a photon from an electron with momentum $\mathbf{p}$. For fixed $\mathbf{q}$, the energy transfer is determined by the projection of the electron's momentum along the direction of the momentum transfer, $p_q \equiv \mathbf{p}\cdot\hat{\mathbf{q}}$, where $\hat{\mathbf{q}} = \mathbf{q}/|\mathbf{q}|$. The dynamic structure factor, $S(\mathbf{q},\omega)$, must then be proportional to the number of electrons with a given value of this momentum projection. Indeed, one can show that in the IA,[72]

$$S(\mathbf{q},\omega) = (m/\hbar q) J(p_q), \tag{3.5}$$

$$J(p_q) \equiv \int \mathrm{d}^3 p\, \rho(\mathbf{p})\, \delta(p_q - (\omega m/q - \hbar q/2)), \tag{3.6}$$

where $\rho(\mathbf{p})$ is the one-particle electronic momentum density. $J(p_q)$, commonly referred to as the Compton profile (CP), gives precisely the average number of electrons with momentum-projection p_q. From eqs. (3.4), (3.5), and (3.6), we see that the resulting Compton peak

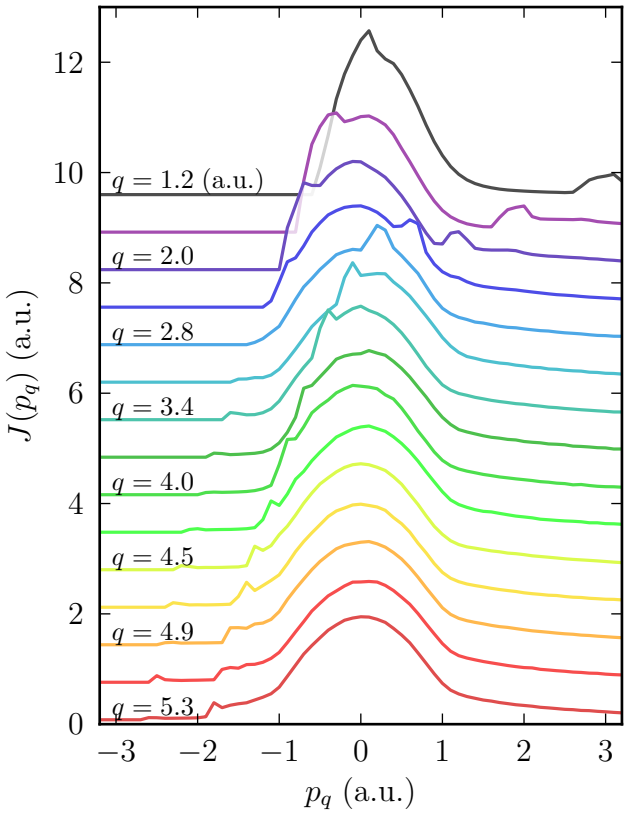

Figure 3.2: (Color online.) The same data as Fig. 3.1 after changing variables to $J(p_q)$. All momentum transfers q are in a.u. Above the Be K-absorption edge, the spectra are nearly identical showing the applicability of the Impulse Approximation in that regime. The sharp feature dispersing across the Compton peak for intermediate q is the Be K edge. The plasmon excitation peak is visible in the 4 curves with lowest q.

in the NIXS spectrum will be centered around $\omega = \hbar q^2/2m$ and have a width proportional to both the width of the one-electron momentum distribution and the momentum transfer. This explains the dispersion and broadening visible in Fig. 3.1.

In the independent-particle approximation, $S(\mathbf{q}, \omega)$ can be written as a sum over independent, non-interfering contributions from valence, semi-core and core electrons. Thus, the respective contributions to the CP can also be separated. For the valence contribution, the conditions of the IA are satisfied for all but the lowest q. On the other hand, for the core contribution, only the high energy transfer tail is correctly described by the IA. In Fig. 3.2, we show the Be NIXS spectra after switching variables from $S(\mathbf{q}, \omega)$ to $J(p_q)$. The Compton peak is centered about $p_q = 0$, consistent with vanishing average electron momentum. The valence contribution is sharper, extending between $\approx \pm 1$ a.u. The core contribution is broader, extending well above +3 a.u., with a low energy-transfer cutoff that is q-dependent. This cutoff occurs when the energy transfer is equal to the K-shell binding energy, and thus disperses from -2 to +3 a.u. as q decreases from 5.3 to 1.2 a.u. Additionally, the plasmon peak is seen at small negative p_q for the lowest values of momentum transfer. It is clear that once well above the K-absorption edge, the spectra are nearly identical, indicating the validity of the IA.

3.2.3 Real-space formalism for valence Compton Profile

If the IA holds, then, as seen in Eq. (3.6), the dominant ingredient required for calculation of the Compton profile is the one-electron momentum density $\rho(\mathbf{p})$. Several techniques exist to calculate $\rho(\mathbf{p})$. Existing methods for solids typically use a band-structure approach, and thus impose a requirement of periodic structure,[52] complicating the application to disordered systems. Some classes of disorder, such as substitutionally disordered alloys have been treated in KKR calculations by using the coherent potential approximation, in which the alloy is replaced by an ordered system with a single averaged effective site potential.[14] An early attempt at describing thermal effects in Li was based on calculating band structures for frozen configurations in 8-atom super-cells.[67] These calculations predicted a broadening of the CP with increased temperature. In contrast, subsequent experiments on Al, Li

and Be found instead that the CP became narrower as temperature increased.[268, 143] By comparing to a pseudopotential model that included thermal effects by scaling the plane-wave components by Debye-Waller factors, these authors attributed the dominant source of the effect to be from thermal expansion of the lattice. We seek to relax the constraint of periodicity by using a real-space analogue of KKR, as implemented in the `FEFF` code,[232] to calculate the Green's function in the muffin-tin approximation for an arbitrary cluster of atomic sites. This code builds in self-consistent potentials, quasi-particle effects, relativistic effects, and disorder and has been widely used for calculations of core-level x-ray spectroscopy. However, the extension of FEFF to the valence regime as discussed here is still developmental.[224]

Briefly the strategy of the code is as follows: Given the locations and species of atoms in a cluster, `FEFF` calculates atomic wavefunctions for each unique species using a Dirac-Hartree-Fock solver. Next, the atomic densities and cluster structure are used to form overlapped atomic potentials in the spherical muffin tin approximation. The real-space one-particle Green's function is then constructed including the full effects of multiple-scattering from other atoms within a specified radius. The density of states (DOS) is calculated by integrating the imaginary part of the Green's function over all space (as approximated by a sum over Norman spheres centered at each site[205]). The Fermi level is determined by integrating the DOS to give the appropriate number of electrons. The density is then recalculated from the Green's function, giving new potentials. This process is iterated until self-consistent.

The momentum-space density $\rho(\mathbf{p})$, is related to the real-space density matrix, $\rho(\mathbf{r}, \mathbf{r}')$ via a Fourier transform:

$$\rho(\mathbf{p}) = \int \mathrm{d}^3 r \, \mathrm{d}^3 r' \, e^{i\mathbf{p}\cdot(\mathbf{r}-\mathbf{r}')} \rho(\mathbf{r}, \mathbf{r}'). \tag{3.7}$$

Choosing the z-axis to lie along $\hat{\mathbf{q}}$, combining Eqs. (3.6) and (3.7) and integrating over p_x and p_y gives delta functions that set $x = x'$ and $y = y'$. After performing the x' and y' integrals we have

$$J(p_q) = \int \mathrm{d}x \, \mathrm{d}y \, \mathrm{d}z \, \mathrm{d}z' \, e^{ip_q(z-z')} \rho(\mathbf{r}, \mathbf{r}'), \tag{3.8}$$

where $\mathbf{r} = (x, y, z)$ and $\mathbf{r}' = (x, y, z')$.

Now, the real-space density matrix is related to Green's function by

$$\rho(\mathbf{r},\mathbf{r}') = -\frac{2}{\pi}\mathrm{Im}\int_{E_c}^{\infty} \mathrm{d}E\; G(\mathbf{r},\mathbf{r}',E) f_T(E), \tag{3.9}$$

where $f_T(E) = 1/(e^{(E-\mu)/k_BT}+1)$ is the Fermi distribution and μ is the chemical potential. For our purposes, we are interested in the valence CP, so the lower energy cutoff E_c is set in the gap between core and valence states (typically around -30 eV). In this paper, all calculations are at $T = 0$, so the Fermi distribution is replaced by $\Theta(E_F - E)$, where E_F is the Fermi energy. The factor of 2 comes from spin degeneracy (here we assume no spin dependence in G, although it is straightforward to generalize).

Finally, the Green's function can be expressed in the muffin-tin approximation as [224]

$$\begin{aligned} G(\mathbf{r},\mathbf{r}',E) = \quad & -2k\Big[\delta_{n,n'}\sum_{L} H^E_{Ln}(\mathbf{r}_>)\bar{R}^E_{Ln'}(\mathbf{r}_<) \\ & + \sum_{L,L'} R^E_{Ln}(\mathbf{r}_n) e^{i\delta_{Ln}}\, g^E_{Ln,L'n'}\, e^{i\delta_{L'n'}}\, \bar{R}^E_{L'n'}(\mathbf{r}'_{n'})\Big]. \end{aligned} \tag{3.10}$$

The indices n and n' label the atomic sites nearest $\mathbf{r}$ and $\mathbf{r}'$, and $\mathbf{r}_n \equiv \mathbf{r} - \mathbf{R}_n$, where $\mathbf{r}_n$ is the center of the nth site. $R^E_{Ln}(\mathbf{r}) = i^l R^E_{Ln}(r) Y_L(\hat{\mathbf{r}})$ is the regular solution at site n with angular momentum L and energy E. $H^E = N^E - iR^E$ where N^E is the irregular solution. The overbar denotes complex conjugation of all parts except for the radial function, e.g., $\bar{R}^E_{Ln}(\mathbf{r}) = (-i)^l R^E_{Ln}(r) Y^*_L(\hat{\mathbf{r}})$. δ_{Ln} gives the scattering phase shift and $g^E_{Ln,L'n'}$ is the full multiple scattering (FMS) matrix.[5] For a derivation of Eq. (3.10), we refer to the Appendix of Prange et al.[224] and references therein.

3.2.4 Core Contribution

The IA does not hold for the core contribution to $S(\mathbf{q},\omega)$ at the momentum transfers shown in Figs. 3.1 and 3.2 since the energy transfer is comparable to the core binding energy. In this case, it is possible to calculate the core NIXS contribution directly using the RSGF approach described by Soininen et al.[263] We give results using this approach below, in Section 3.4.2.

At higher momentum transfer (as would be accessible with higher incident photon energy), or when only interested in the high energy transfer portion of the spectrum, it is

possible to use the IA for the core contribution. Since solid-state effects on the localized core wavefunction are typically negligible, the core momentum density can be obtained directly from Fourier transformed atomic Hartree-Fock wavefunctions using $\rho(p) = \sum_i |\phi(p)|^2$. The core CP in the IA can then be obtained by combining this with Eq. (3.6).

3.3 Computational Details

We have extended `FEFF` to calculate the momentum density $\rho(p)$ in Eq. (3.7) and thence the Compton profile. Our procedure makes use of a subroutine `rhorrp` in FEFF, which calculates the density matrix $\rho(\mathbf{r}, \mathbf{r}')$ by combining equations (3.9) and (3.10). To calculate the CP from Eq. (3.8), we approximate the integral over $\mathbf{r}$ as a sum over Norman spheres centered at each atomic site. For a given term in this sum, $\mathbf{r}$ is constrained to lie within the Norman radius while z' is allowed to vary over all space (in practice, limited by the size of the cluster). In a periodic system with a monatomic unit cell each site is identical, so the integral need only be performed for a single site. This normalizes the integral of the resulting CP to the number of valence electrons per atom. In general, $\mathbf{r}$ must be integrated over each unique site in the system, e.g. every site in the cluster for a completely disordered system.

The sum over angular momenta in Eq. (3.10) is truncated at a configurable upper bound $l_{\max}$. Since the size the FMS matrix $g^E_{Ln,L'n'}$, scales as $(l_{\max}+1)^4$, it is desirable to keep this bound as low as possible. However, if the value used is too low, the density matrix becomes inaccurate away from the center of a site, leading to a discontinuity as z' moves from one site to another. In Fig. 3.3, we show a slice of the density matrix $\rho(\mathbf{r}, \mathbf{r}')$ with $\mathbf{r}$ fixed near the origin and $\mathbf{r}'$ varying along the $\hat{\mathbf{z}}$ axis. The discontinuity at the point marked "Cell Boundary" is clear for small $l_{\max}$ and decreases as $l_{\max}$ is increased. Typically the discontinuity is negligible for $l_{\max} \geq l_{\mathrm{v}}$, where l_{v} is the atomic valence orbital angular momentum (e.g. $l_{\max} = 4$ for transition metals).

Numerical integration of Eq. (3.6) is performed in cylindrical coordinates. At each z, z' point, the integral over the x-y plane is calculated. This reduced $\rho(z, z')$ is then Fourier transformed to obtain the CP. In some cases, the CP calculated in this fashion displays oscillatory aliasing effects from the finite range of the Fourier transform. A Hann

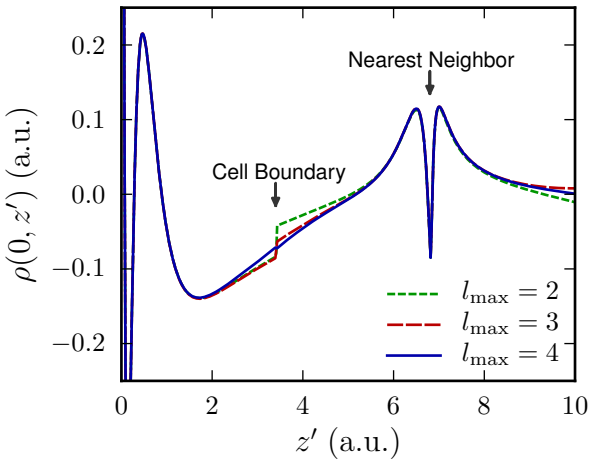

Figure 3.3: (Color online.) Dependence of Cu density matrix on angular momentum cutoff, $l_{\max}$. A slice of $\rho(r, r')$ with r fixed near the origin and r' varying along the z-axis is shown. The discontinuity at ~ 3.4 a.u. occurs as r' moves from one cell into another. As $l_{\max}$ is increased, the discontinuity decreases.

apodization function can be included to remove these. The finite range of z' has two further consequences. First, some momentum density is missed, resulting in the integral of the CP being less than the number of valence electrons per atom. This $\lesssim 5\%$ effect is corrected for by rescaling the CP. Second, the CP is broadened due to the convolution theorem, reducing the momentum resolution to $\sim \pi/z'_{\max}$. This latter factor is one key limitation of this technique: the number of atoms in a cluster scales as the cube of the radius, placing a practical bound on the attainable momentum resolution.

3.4 Results and Discussion

3.4.1 Valence Compton Profile

In order to validate our new framework, we have calculated the valence Compton profile (CP) for Be at ambient conditions with lattice constants $a = 4.3289$ a.u. and $c = 6.7675$ a.u. These calculations are compared to experimental data and momentum-space (KKR)

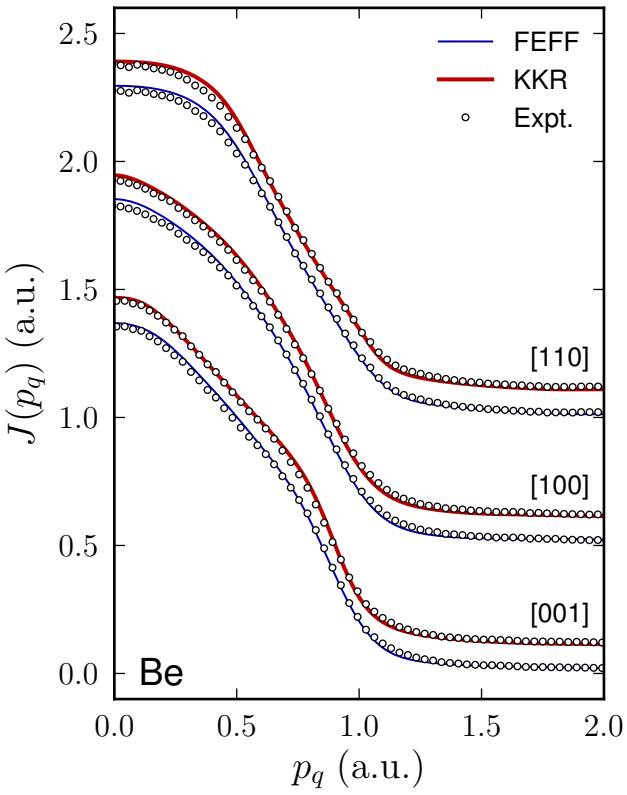

Figure 3.4: (Color online.) Be Compton profile. Experimental data from Huotari, et al.[141] is compared to a momentum-space (KKR) calculation from the same reference and our real-space (FEFF) calculation. The experimental data were taken at 56 keV and have had the theoretical core contribution and a small linear background subtracted. For each direction, the same experimental data is presented twice (once for each theory). The experimental statistical uncertainty is smaller than the symbol size. The Fermi surface is located at the inflection point of the CP, just below 1 a.u.

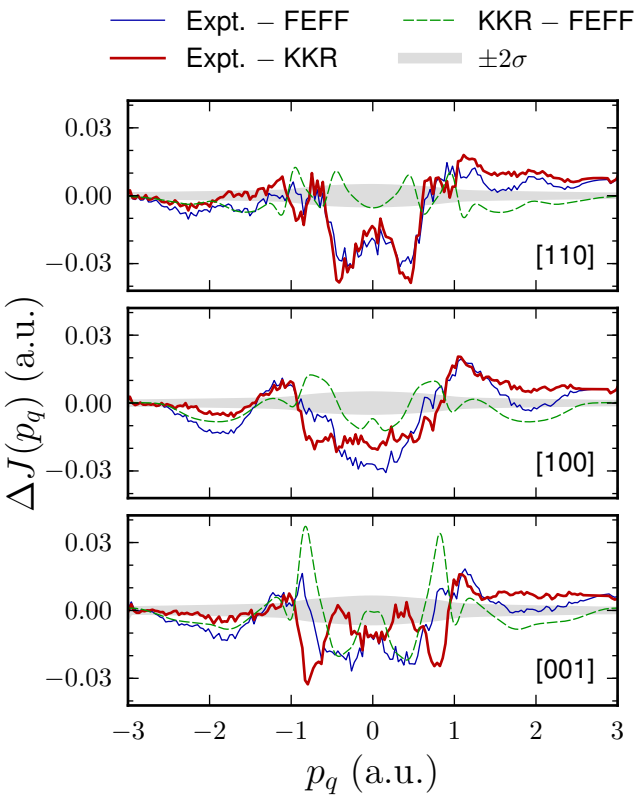

Figure 3.5: (Color online.) Be Compton profile differences. The solid curves show the difference between experiment and theory. The dashed curve is the difference between theories. These are superimposed on the $\pm 2\sigma$ range of experimental statistical uncertainty.

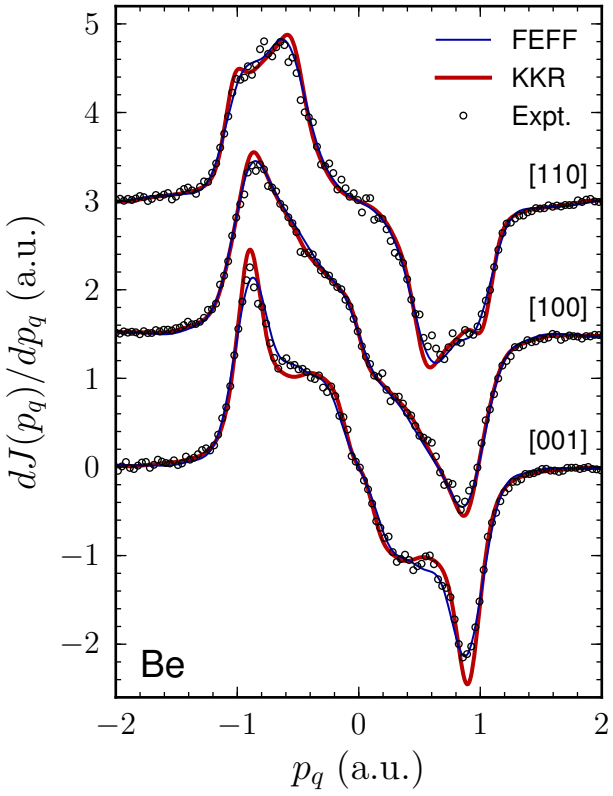

Figure 3.6: (Color online.) Be Compton profile derivative. The same experimental data and theoretical calculations as Fig. 3.4 are shown, but this time as first derivatives. The fine structure of the profile is more clearly seen here. Experimental statistical uncertainty is smaller than the symbol size. The Fermi surface is located at the extrema of the derivative.

theoretical calculations from Huotari, et al.[141] Comparisons are made for the three main crystallographic directions of the hexagonal close-packed structure ([100], [110] and [001], where the $\hat{\mathbf{a}}$ and $\hat{\mathbf{b}}$ basis vectors have been chosen to be 60° apart). In Fig. 3.4 we present the primary result of this work, showing very good agreement between the present real-space theory and momentum-space theory, and good agreement between both theories and experiment. We now give contextual details for the comparison.

The experimental data in Fig. 3.4 (reproduced from Huotari, et al.[141]) were taken at 56 keV with a momentum resolution of 0.16 a.u. The momentum-space theoretical calculations (also from Huotari, et al.[141]) were performed using the KKR[169, 167] methodology. Crystal potentials were calculated in the local density approximation (LDA), and exchange and correlation effects were approximated via the isotropic Lam-Platzman (LP) correction.[179]

Our real-space calculations were performed using a cluster of 522 atoms within a sphere of 10 Å radius with $l_{\max} = 2$. Increasing $l_{\max}$ beyond this value had no effect for this low-Z material. The density matrix was evaluated with $\mathbf{r}$ on a $32 \times 32 \times 32$ point cylindrical grid and z' at 144 points between ± 30 a.u. The range over which z' is integrated is limited by the cluster size. This limits the momentum resolution of the real-space theoretical CP to $\delta q = \pi/30 \simeq 0.1$ a.u. Lattice motion, which can be approximately treated by FEFF, has been neglected. The LP correction has not been applied to the real-space calculations.

As described by Huotari, et al.,[141] a linear background has been subtracted from the experimental data. Additionally, since it is our purpose to compare valence profile calculations, we have subtracted the theoretical core profile presented in the original reference.[141] The theoretical curves in Fig. 3.4 are offset for clarity and for each direction, the same experimental data is presented twice (once for each theory). Absolute differences between these curves are shown in Fig. 3.5. The two theories are in similarly good agreement with experiment. Significant systematic errors are introduced by the subtraction of the core CP, which most likely is the cause of the linear trend in the differences with experiment. The FEFF calculations slightly overestimate the momentum density in in the range $1 < |p_q| < 2$. It is unclear whether this is a numerical artifact or a consequence of the muffin-tin approximation. The largest discrepancy between the two theories is at $|p_q| \sim 0.9$ in the [001] direction, and is below the 5% level. Given the analogous nature of the KKR and RSGF

methods, one would expect the two theoretical results to differ by the LP correction, which was only applied to the KKR theory. This discrepancy may be due to differing muffin-tin radii. The KKR calculation assumes non-overlapping muffin tins, while the RSGF calculation uses overlapping muffin tins.[232] As pointed out in Huotari, et al.,[141] the residuals with experiment are similar in shape to the LP correction, suggesting that were it included in the RSGF calculation, the agreement would be even better. Finally, in order to more clearly see the fine-structure, we show the derivative of the CP in Fig. 3.6. Here, the experimental data were numerically differentiated using a 3-point derivative, with no additional smoothing. The overall similarity between the two theoretical curves further validates our implementation of the RSGF technique.

Given the good agreement with Be, it is natural to ask if the RSGF method extends to other simple metals that are well described in the muffin-tin approximation. We have included a calculation of the valence CP for crystalline Cu with $\hat{\mathbf{q}}$ along the [110] direction. In Fig. 3.7, we compare the FEFF calculation with KKR and with two different experiments. The KKR calculation and experiment labeled Sakurai are reproduced from Sakurai, et al.[245] The experimental data was taken using 59.38 keV X rays with a momentum resolution of 0.12 a.u. Additionally, we include a gamma-ray measurement (412 keV incident, 0.41 a.u. momentum resolution) from Pattison, et al.[215] The FEFF calculations were performed using a cluster of 176 atoms within a sphere of 8-Å radius with $l_{\max} = 4$. The density matrix was evaluated with $\mathbf{r}$ on a $48 \times 48 \times 48$ point cylindrical grid and z' at 256 points between ± 20 a.u. Again, the FEFF and KKR calculations are similar. Even after accounting for momentum resolution, the two experiments are not in agreement with each other. This disagreement has been attributed to systematic errors introduced while correcting for multiple Compton-scattering events.[245] These errors are expected to be smaller in the Sakurai dataset, but the agreement between theory and the supposedly erroneous Pattison dataset is impressive, and suggest that a reinterpretation of the experimental data may be appropriate.

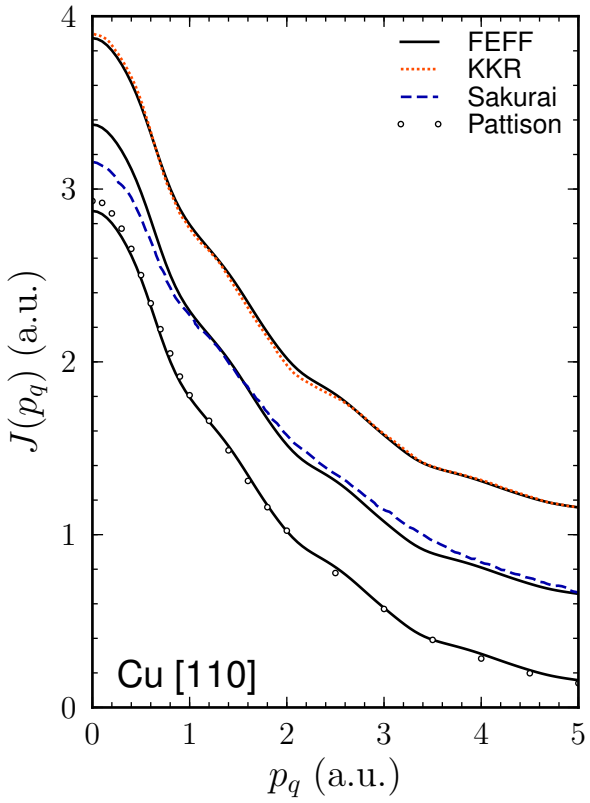

Figure 3.7: (Color online.) Cu [110] valence Compton profile. Curves have been offset by 0.5 a.u. for clarity. The KKR calculation and x-ray scattering data (59.38 keV incident, 0.12 a.u. momentum resolution) from Sakurai, et al.[245] For comparison we have included a gamma-ray dataset (412 keV incident, 0.41 a.u. momentum resolution) from Pattison, et al.[215]

3.4.2 Comparison of FEFF with NIXS data.

In the prior Section, we have focused on experimental data taken for the explicit purpose of studying the CP, and thus taken well into the regime of applicability of the IA. Often, as in NIXS studies of WDM, the energy- and momentum-transfer regimes accessible are more intermediate. The IA typically does not apply to scattering from the core electrons, and at lower momentum transfer breaks down even for the valence electrons. Our purpose in this Section is to find the limits of applicability of the RSGF technique in this intermediate regime.

Experimental data in this Section (also presented in Figs. 3.1 and 3.2) were collected using the recently upgraded LERIX instrument at beamline 20-ID at the Advanced Photon Source.[84, 254] The instrument consists of 19 spherically bent Si crystal analyzers on a 1-m radius semi-circle. The incident beam is polarized normal to the plane of the semi circle, so the polarization factor from Eq. (3.2) is unity for all analyzers. Each analyzer selects a narrow band of radiation around 9890 eV at a fixed scattering angle. The incident beam energy is varied to cover the energy loss region of interest. The energy loss scale is independently calibrated to within 0.1 eV for each analyzer using the center of the elastic scattering peak and points withing each spectrum are normalized to the incident flux measured measured by an ion chamber upstream of the sample.

For fixed scattering angle θ, the magnitude of q is given by

$$q^2 = \omega_1^2 + \omega_2^2 - 2\omega_1\omega_2\cos(\theta). \tag{3.11}$$

Combining this with Eq. (3.6), it is straightforward to convert from the valence CP to $S(\theta, \omega)$. Since the IA does not apply for the core, we use the `FEFFq` package[263] to calculate the directionally averaged core contribution to $S(q, \omega)$. This is done for a fine mesh of q values, which are interpolated between using Eq. (3.11) to obtain the fixed-angle $S(\theta, \omega)$.

We have subtracted a small linear background from the data. Although it is possible to apply f-sum normalization to $S(q, \omega)$, the same is not true for $S(\theta, \omega)$. For this reason, the overall normalization of the data was left as a free parameter. The results for several different scattering angles are shown in Fig. 3.8. Close to backscatter ($\theta \gtrsim 110°$), the agreement is very good. In our calculations of the core contribution, this detailed near-edge

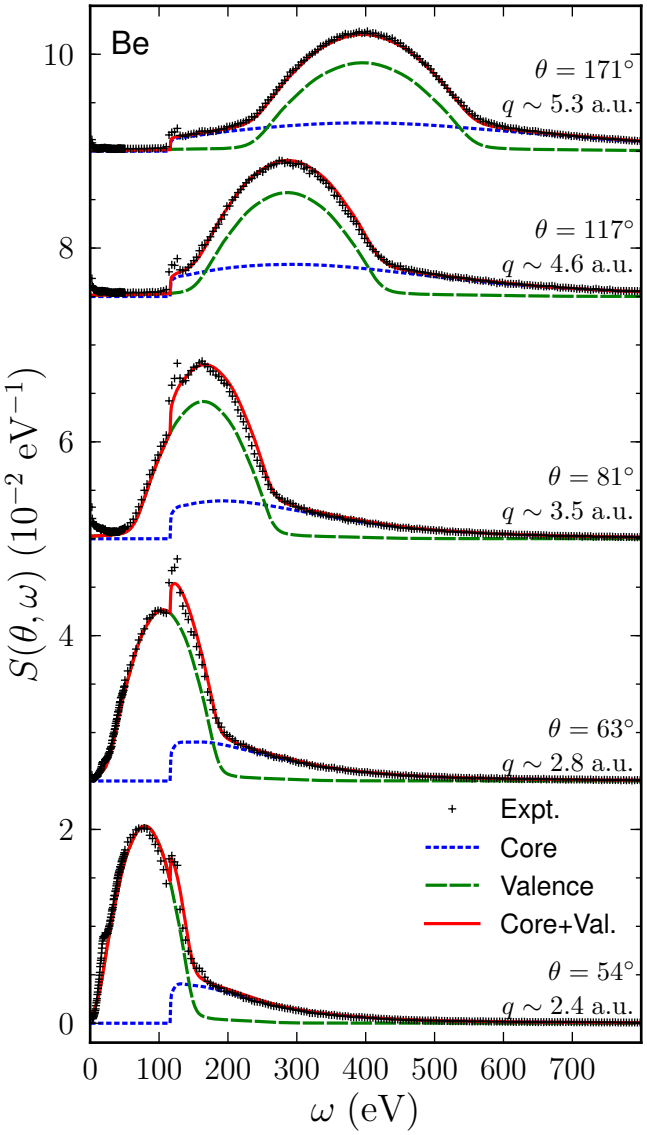

Figure 3.8: (Color online.) Comparison with NIXS data for polycrystalline Be at 5 different values of momentum transfer q. The core contribution to the spectrum is calculated using `FEFFq` package.[263] The valence is calculated using the techniques described in this paper and averaged over the three main crystallographic directions. At the lowest two values of momentum transfer, a plasmon excitation is visible at $\sim$ 25 eV. This signals the onset of the collective regime and the breakdown of the IA for the valence electrons.

structure (XANES) was not included, leading to the noticeable differences at the Be K edge. As q is decreased, the IA becomes less valid and some discrepancies emerge. Additionally, the collective plasmon excitation is present in the experimental data for the lowest q value shown (at $\omega \sim 20$), which is not modeled in the RSGF theory.

3.4.3 Application to WDM

Before concluding, we recall that a long-term goal of this work is to extend its application to high temperature and/or disordered systems, as in the case of WDM. Present methods for treating NIXS from WDM calculate the valence-electron contribution to the dynamic structure factor within the random phase approximation (RPA) from the dielectric function using the fluctuation-dissipation theorem.[41, 43, 136, 108] The valence electrons are treated as free, with effects of collisions with ionic cores included perturbatively in the Born-Mermin approximation (BMA)[136]. At lower densities, collisions are infrequent and the BMA approach is unlikely to omit quantitatively important aspects of the behavior of unbound electrons. However, at solid-like and higher densities, any perturbative treatment of the dominant physical presence in the system, the ionic cores, will clearly benefit from independent validation against more complete theoretical treatments. By contrast, the approach present in this work includes all orders of valence electron scattering caused by such condensed phase effects.

The most complete extension of the RSGF approach to calculations of WDM phases will require several steps beyond the present work. First, thermal and static structural disorder can be treated approximately by including Debye-Waller factors in the FMS calculation.[5] More general structural disorder can be treated by averaging over configurations taken from finite-temperature, molecular dynamics simulations. These disorder effects tend to dampen the fine structure in the density function. Second, the smearing of the Fermi distribution can be handled as in Eq. (3.9); the Fermi function should be included self-consistently in the calculation of the Green's function and density matrix. Finally, for the WDM case with temperatures comparable to or larger than the Fermi energy, a more appropriate, finite-temperature exchange-correlation potential is called for, which will likely affect the width

of the Compton profile.

3.5 Conclusions

We have demonstrated a real-space Green's function technique for calculating valence Compton profiles for Be and Cu. We find close agreement with high momentum-transfer experimental measurements and prior theoretical calculations for these systems, validating the implementation. Furthermore, we have shown that the technique can be used at moderate momentum-transfer as long as the core contribution to the dynamic structure factor is properly treated. Although periodic systems were chosen for the comparison, the technique does not require periodicity and thus should be readily applicable to disordered systems. This lays the groundwork for first principle calculations of high momentum-transfer NIXS from WDM, where disorder in potentials, ionization and atomic structure is expected to be relevant.

Chapter 4

EXTENDING FEFF TO FINITE ELECTRONIC TEMPERATURES

4.0.1 Thermal occupation in the SCF loop

The primary change necessary to generalize FEFF to finite electronic temperature is to use the Fermi function for the occupation of states. That is, we replace Eq. (2.10) by

$$N = \sum_i \int_{E_C}^{\infty} \rho_i(E) f(E) dE \tag{4.1}$$

$$f(E) = \frac{1}{e^{(E-\mu)/kT} + 1}, \tag{4.2}$$

where the chemical potential μ is now determined by this constraint.

The Fermi function $f(E)$ is periodic in the complex plane with In the complex plane, with $f(E + i * 2\pi kT) = f(E)$, and is analytic except for simple poles at $E_n = \mu + i\omega_n$, where $\omega_n = (2n + 1)\pi kT$ are the Matsubara frequencies. The residue at the poles is equal to kT. Fig. 4.1 shows $\mathrm{Re}\, f(E)$ for a small region of the complex energy plane, in which the periodicity and pole structure are evident.

We define an integration contour C that follows the path $E_C + 0i \rightarrow E_C + iE_1 \rightarrow E_2 + iE_1 \rightarrow E_2 + 0i$, where $E_1 = 2nkT$. For now, the value of the integer n is left as arbitrary choice. Formally $E_2 \rightarrow \infty$, although in practice any finite value can be used provided $f(E_2)$ is negligible at the desired level of accuracy. Let C_0 be the contour along the real axis from $E_C \rightarrow E_2$. Then, for any function $g(E)$ that is analytic in the upper half plane, Cauchy's integral theorem implies

$$\int_{C_0} f(E)g(E)dE = \int_{C} f(E)g(E)dE \sum_{j=1}^{n} (-2\pi i)kTg(\mu + i\omega_j). \tag{4.3}$$

If we directly apply this to Eq. (4.2), the poles give a suspect imaginary contribution to the number of electrons. We must instead integrate the complex density of states defined as in Eq. (2.9), except without taking the imaginary part. Only after integrating over energies

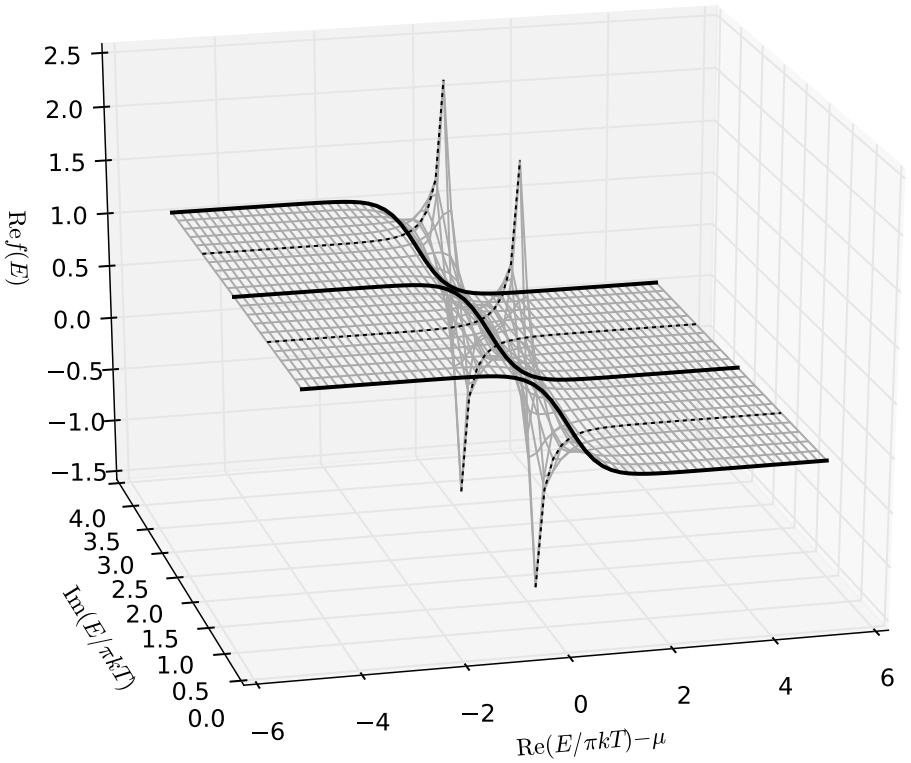

Figure 4.1: The Fermi function $f(E)$ in the complex plane.

can we take the imaginary part to obtain the number of electrons. In the following we will implicitly take $\rho(E)$ to be the complex density of states.

Starting with an initial guess for μ (e.g., that for a Fermi gas with the average density), we can then use Eqs. (4.3) and (4.2) to numerically solve for the actual μ. Since evaluation of $\rho(E)$ is computationally expensive, we proceed by first calculating $\rho(E)$ on a grid of points along the contour C, which can be performed in parallel. Note that the final leg can be ignored since $f(E_2)$ is negligible. For a given guess at μ, $\rho(E)$ need then only be calculated at the Matsubara poles contained within the integration contour. We can then numerically minimize to solve for μ. The value of E_1 must be chosen to balance the smoothness of $\rho(E)$ along the contour C and the number of Matsubara poles that must be calculated at each step in this final minimization. The minimization to solve for μ is currently performed serially using the secant rule to generate the next guess from the prior ones. This could be improved by a parallel algorithm which tries a grid of μ values and uses a higher-order polynomial to update to the next guess. However, we have found that the minimization converges after a small number of steps ($\lesssim 10$), and thus this is a low priority.

Once μ has been determined, the real-space density can be calculated by combining Eqs. 2.7) and (4.3), again with the caveat that the imaginary part must be taken only after the integral over energies.

4.0.2 A finite temperature exchange-correlation potential

The ground-state exchange-correlation potential of von Barth and Hedin[17] is of questionable validity when thermal excitation become significant. As an initial attempt to remedy this, we have added support for the finite-temperature exchange-correlation potential of Perrot and Dharma-Wardana[218]. In Fig. 4.3, we show the finite-T $V_{\rm xc}$ as a function of temperature and r_s, the average inter-particle spacing in atomic units. For high densities and for $T \lesssim 10$ eV, this potential differs only slightly from the ground-state potential, shown by the filled circles. We note that the interpolating formula used appears to be innaccurate at very low temperatures. We have not made a systematic study of the effect of the finite temperature potential, however, for Be at or above solid density, we have found negligible

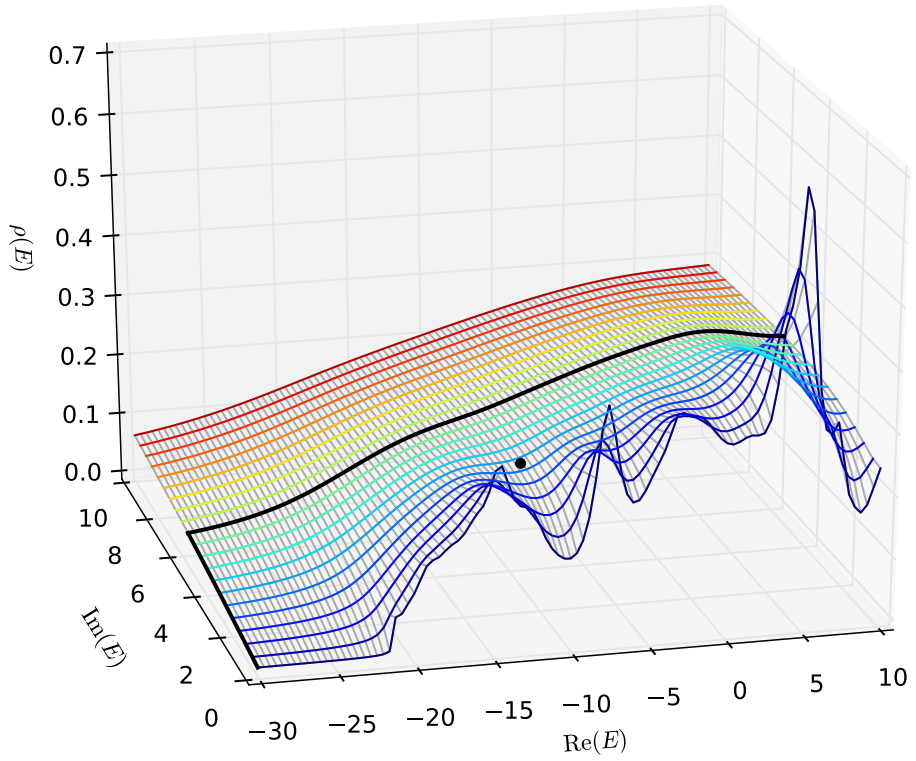

Figure 4.2: Integration contour used to integrate over the density of states at finite temperature. The Fermi function (not shown here) has a single pole within the contour, at the location indicated by the black dot.

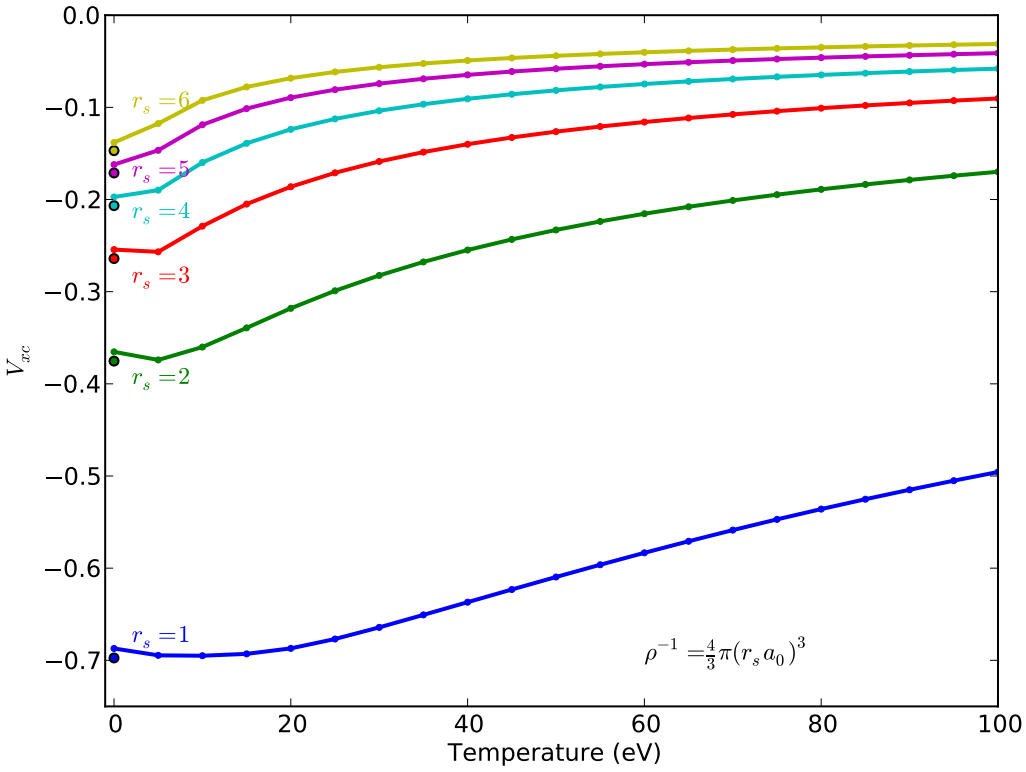

Figure 4.3: The finite-temperature exchange-correlation potential of Perrot and Dharma-Wardana, calculated for several different densities. The circles at T=0 give the value of the ground-state LDA potential for the same density.

differences in Compton profiles calculated using the two different potentials for $T < 15$ eV.

4.0.3 Going forward

So far, only the SCF loop and valence-electron Compton profile calculations have been extended to finite temperature. Modifications of other spectroscopic calculations remain to be made.

We note that a practical upper bound on the electronic temperature that can be treated exists. A configurable cutoff $L_{\max}$is used to limit the angular momentum expansion of the

Green's function in Eq. (2.1). Higher-L terms contribute only at larger energies, and thus, the occupied DOS for low temperatures can be accurately calculated with a relatively low cutoff. However, as temperature is increased and higher energy states become occupied, the angular momentum cutoff will need to be increased.

Finally, at present, we only treat the elevated temperature of the electrons. The lattice itself is frozen. For nanosecond scale laser-shock experiments, where lattice disorder is expected to be signficant, a proper high-temperature calculation would require averaging over an ensemble of frozen configurations obtained from, e.g., molecular dynamics simulations. This should be straightforward, albeit computationally expensive.

Chapter 5

THE EFFECT OF CORE-ORTHOGONALIZATION ON THE VALENCE ELECTRON MOMENTUM DISTRIBUTION

In dense systems, the electronic states typically separate into deeply bound core states, which are highly localized and retain their atomic character, and the delocalized valence states, which are much more free-electron like in character. This separation is often exploited to simplify the theoretical treatments of electronic structure, most notably in highly successful use of pseudopotentials. In a pseudopotential treatment, one removes the core states entirely from the picture and replaces the ionic potential with an effective potential chosen to reproduce the valence states outside of some radius. This method accurately reproduces the real-space density away from the ions by construction, but clearly cannot simultaneously reproduce momentum space quantities. In particular, the psuedo-wavefunction is smooth near the ionic core, containing none of the nodes and corresponding oscillations that would otherwise be present due to the requirement of orthogonalization between the valence and core states.

In the early 70s, Pandey and Lam proposed a simple modification of pseudo-wavefunctions to include the effect of orthogonalization[214]. Using simple plane waves to approximate the pseudo-wavefunctions for metallic Na (for which the psuedopotential is rather small) and subtracting off the projection onto a Hartree-Fock 1s wavefunction, they found that the effect of core-orthogonalization on the Compton profile (CP) was non-negligible and resulted in much better agreement with experimental data. Shortly thereafter, Cooper used Pandey and Lam's treatment to calculate the CP for Al, also finding reasonably good agreement[50]. Examples of explicitly orthogonalizing pseudo-potential wavefunctions to the core states can be found for Be[238] and Li[19]. In all cases, the orthogonalization results in a decrease in the height of the Compton profile, and an increase in the high-momentum tails.

In this chapter, we explore the effects of orthogonalization as a function of the relative

size of the core state to the atomic volume using a simple one-dimensional version of Pandey and Lam's model.

5.1 A simple one-dimensional model

Consider plane-wave states within a periodic super-cell of size L

$$\langle x|k_j\rangle = L^{-1/2}\exp(ik_jx) \tag{5.1}$$

$$k_j = \frac{2\pi j}{L}, j \in \mathbb{Z} \tag{5.2}$$

We assume that within this cell are a set of N atomic cores modeled by normalized Gaussian wavefunctions with common width-parameter σ, centered at the locations $x_{ii=1,N}$.

Initially, we take the cores to be uniformly spaced, i.e. $x_i = L/N(i-1/2)$.

$$\langle x|c_i\rangle = \pi^{-1/4}\sigma^{-1/2}e^{-(x-x_i)^2/2\sigma^2} \tag{5.3}$$

Later, we will consider the effects of disorder.

The plane wave states are orthogonalized to the core states by subtracting off the projection onto each core and renormalizing to unity. That is,

$$|\psi_j\rangle = A_j(|k_j\rangle - \sum_i |c_i\rangle\,\langle c_i|k_j\rangle), \tag{5.4}$$

where the normalization constant A_j is chosen so that $\langle\psi_j|\psi_j\rangle = 1$.

After orthogonalization, a momentum distribution is calculated by summing over occupied states (we assume two electrons, one of each spin per site).

$$\rho(p) = \frac{2a}{2\pi}\sum_{j=-N/2}^{N/2} |\,\langle p|\psi_j\rangle\,|^2. \tag{5.5}$$

Here, a is the lattice spacing and the factor of 2 is due to spin degeneracy. The prefactor has been chosen for comparison with the continuum (large-L) limit, i.e., $\int dp\rho(p) = N_e$, where N_e is the number of electrons per site. For the free gas (in the absence of core-orthogonalization) the momentum distribution is given by $\rho_0(p) = (a/\pi)\Theta(p_F - |p|)$, where the Fermi momentum $p_F = N_e\pi/2$.

In Fig. 5.1, we present the momentum distribution after orthogonalization with an ordered lattice of core states. Here, and throughout the remainder of the chapter, we will

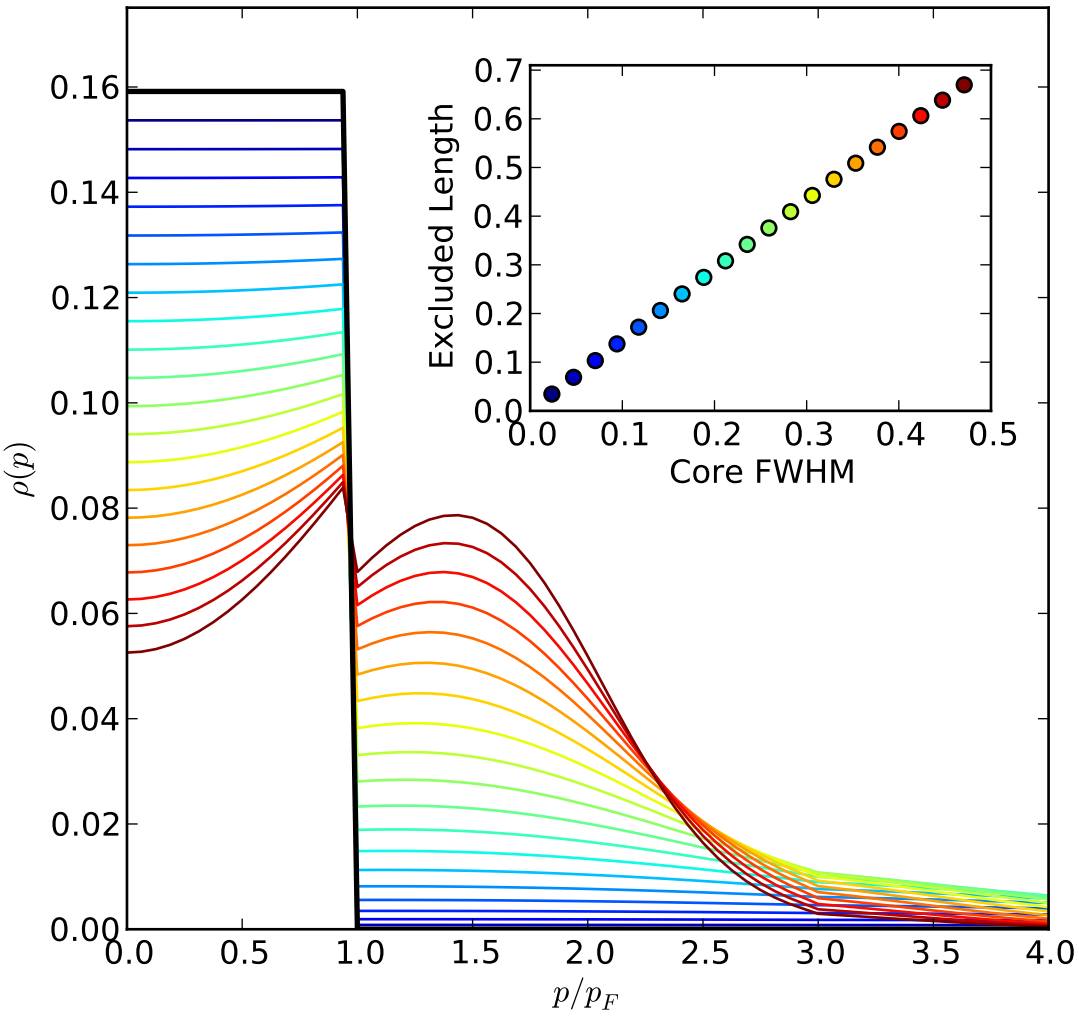

Figure 5.1: Effect of core-orthogonalization on the momentum density. The thick, black curve is the momentum density for a 1-d Fermi gas in the absence of core states. The remaining curves have been orthogonalized against a regular lattice of Gaussian core states of progressively larger width. The inset shows the effective excluded length as a function of the full-width half-max of the core states (both in units of the lattice spacing).

use the lattice spacing a as the unit of length, and consider a system with two delocalized electrons per site. The calculations were performed for 32 Gaussian core states with σ in Eq. (5.3) varying from 0.01 to 0.2 in uniform steps of size 0.01. The thick, black curve gives the numerical result in the absence of orthogonalization, which agrees with the analytical result discussed earlier. For narrow core states, orthogonalization results in a nearly uniform decrease in $\rho(p)$ for $|p| < p_F$, with a corresponding increase for $p > p_F$. As the width of the cores increases, the strength of this effect increases.

The requirement of orthogonalization constrains the degrees of freedom available to the free states. As a somewhat simplistic interpretation, we define an effective unit-cell length a^* by the relation $\rho(0) \equiv a^*/\pi$. From this, we can then define an excluded length $l_{\rm ex} \equiv a - a^*$. As shown in the inset, this excluded length is linearly related to the width of the core state. The effect of core-orthogonalization on the low-p momentum distribution is similar to that of excluding the free electrons entirely from the region occupied by core electrons. We note that this interpretation is not consistent with the effect at or above p_F (if a region of space were truly excluded, one would expect the Fermi momentum to increase), or with the real-space density (which develops sharp peaks at the core sites). For this reason, we prefer to interpret the effect of orthogonalization as an excluded *phase space*.

In Fig. 5.2, we explore the effect of disordering the core locations. We consider two types of disorder. Initially, we displace the cores from their lattice locations by displacing each x_i in Eq. (5.3) by a random amount drawn from a Gaussian distribution of adjustable width σ. The result of averaging over 32 configurations is shown in Fig. 5.2, where the lighter shading about each line gives the standard deviation. As we increase the σ, the value of $\rho(0)$ increases progressively, i.e., the effect of core-orthogonalization decreases partially. However, in the limit of strong disorder, the effect only partially vanishes. We also include a calculation for core locations that are drawn randomly from a uniform distribution over the super-cell. Calculations for Gaussian disorder with large σ converge onto the uniform-disorder case. We have also checked that further increasing the super-cell size has a negligible effect on the results, confirming that the effect is not influenced strongly by residual long-range order.

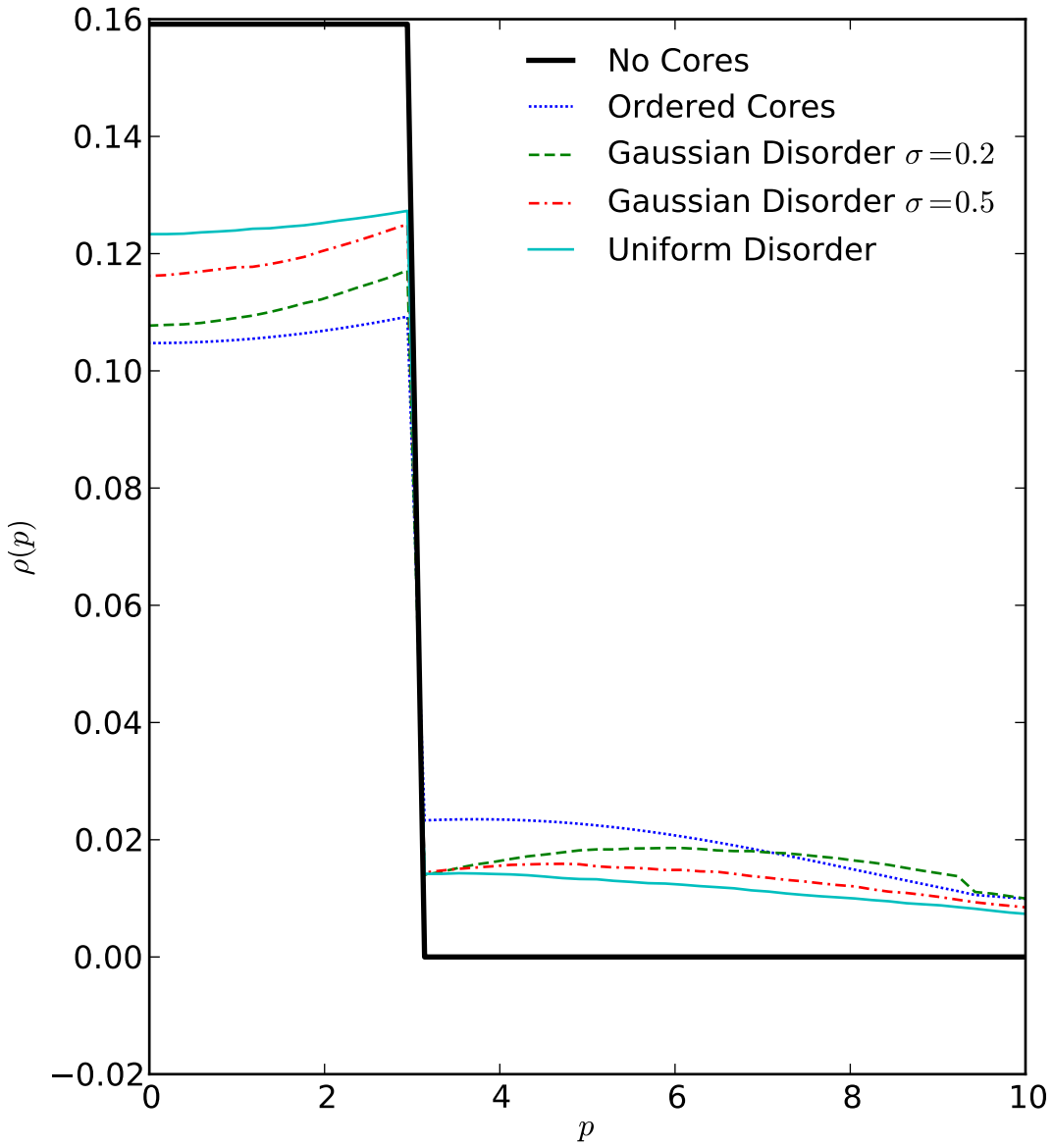

Figure 5.2: The effect of disorder on the modification of the momentum distribution by core-valence orthogonalization. The thick black line is the T=0 Fermi distribution.

5.2 Qualititative effect on Compton profiles

We will now assume that core-orthogonalization has a similar effect on the radial momentum distribution in three dimensions. In particular, for modest sized cores, occupation is uniformly decreased for $p < p_F$ and a tail is introduced for $p > p_F$. Conservation of particle number requires that $\int p^2 \rho(p) dp$ remains constant. We consider the effect of this modification on the isotropic Compton profile, given by Eq.(1.19). Since the integral contains only a single factor of p, it is clear the the value of $J(0)$ necessarily must decrease, and a tail will develop for $p > p_F$. This would have the appearance, especially in low resolution experiments of an additional broadening of the CP, which could be misinterpreted as an increase in either the density or temperature of the system. We explore this further in the following chapter.

Chapter 6

CONDENSED PHASE EFFECTS ON THE ELECTRONIC MOMENTUM DISTRIBUTION IN THE WARM DENSE MATTER REGIME

(*Submitted for publication* Phys. Rev. Lett. Aug. 2013)

We report *ab initio* calculations of the valence electron momentum distribution function $n(p)$ and dynamic structure factor for warm dense Be at Mbar pressures. We observe an unexpected, strong reshaping of the Compton profile upon increasing density, even well before any significant core-wavefunction overlap or electride behavior occurs. We propose that this nonperturbative effect, which is due to a growing influence on $n(p)$ of the orthogonalization of valence and core electron wavefunctions with increasing density, is observable by inelastic x-ray scattering at x-ray free-electron lasers and large-scale laser-shock heating facilities, and may also be more generally important for thermodynamic properties of dense, partially-ionized plasmas.

There is growing interest in dense states of matter intermediate between traditional condensed phase systems and fully-ionized dense plasmas. These "warm dense matter" (WDM) states present unique scientific opportunities with special relevance to planetary and stellar conditions[150, 3, 236, 297], with obvious importance for the early stages of compression in inertial confinement fusion (ICF)[188], and with additional broad, long-term scientific potential when considered as the next-stage of evolution of the available thermodynamic parameter space for the condensed phase community.

As with any new material regime, one must determine the dominant microphysics that establishes the resulting (macroscopic) thermodynamic and statistical properties. For WDM, this is complicated by the lack of simplifying features present in either the cold, ordered limit of condensed matter or the hot, non-degenerate limit of fully-ionized dilute plasmas; unsurprisingly, at present, no broadly-applicable, first-principles treatment of WDM is available.

One must instead combine methods from these opposing limits[107, 231, 261, 161, 162] and then seek comparison with the limited, but growing, body of WDM experimental results.

As a case in point, a common theoretical approach to WDM[115, 114, 107] treats free or ionized electrons in the random phase approximation (RPA)[27] with perturbative corrections for the electron-ion scattering via the Born-Mermin approximation (BMA)[255, 195]. This approach necessarily assumes a weak electron-ion interaction and has seen extensive use in the interpretation of inelastic x-ray scattering from WDM[181, 173, 96, 190].

By contrast, in crystalline materials and other condensed-phase systems it is the electron-ion interaction, both through the Coulombic potential and orthogonalization between core and valence electrons, that plays the dominant role in the overall electronic structure[25, 8, 7]. In addition, at elevated densities, where core wavefunctions begin to overlap, an interesting combination of free-energy effects constrained by valence-core orthogonalization (VCO) can lead to structural changes and novel phases known as electrides in which the valence electrons re-localize in the interstitial spaces between atomic sites[202, 203, 241]. This behavior at low temperatures hints at the possibility of strong influence of the electron-ion interaction, and in particular VCO, on the electronic structure of WDM. This conclusion, which runs contrary to the commonly stated perspective that the electron-ion interaction becomes progressively less important at high plasma densities[180], is further supported by the growing use in WDM molecular dynamics simulations of modern density-functional theory methods, such as projector-augmented wave calculations, that substantially include VCO effects[220, 290].

Here, we report a detailed theoretical study of the valence electron momentum distribution $n(p)$ for warm dense Be. In addition to being a candidate ablator material for ICF, and thus undergoing extensive study in the WDM context[181, 173, 96], Be has seen thorough high-resolution synchrotron study[152, 142, 144, 149]. Our results illustrate that VCO, which has a long history in the context of electronic structure calculations[134, 26] and which plays an important role in determining the ambient momentum distribution of Be and other materials[214, 50, 238, 19], steadily grows in importance upon increasing density. This observation may have significant consequences for calculation of the equation of state or thermodynamic susceptibilities (e.g., compressibility) for WDM but here we focus

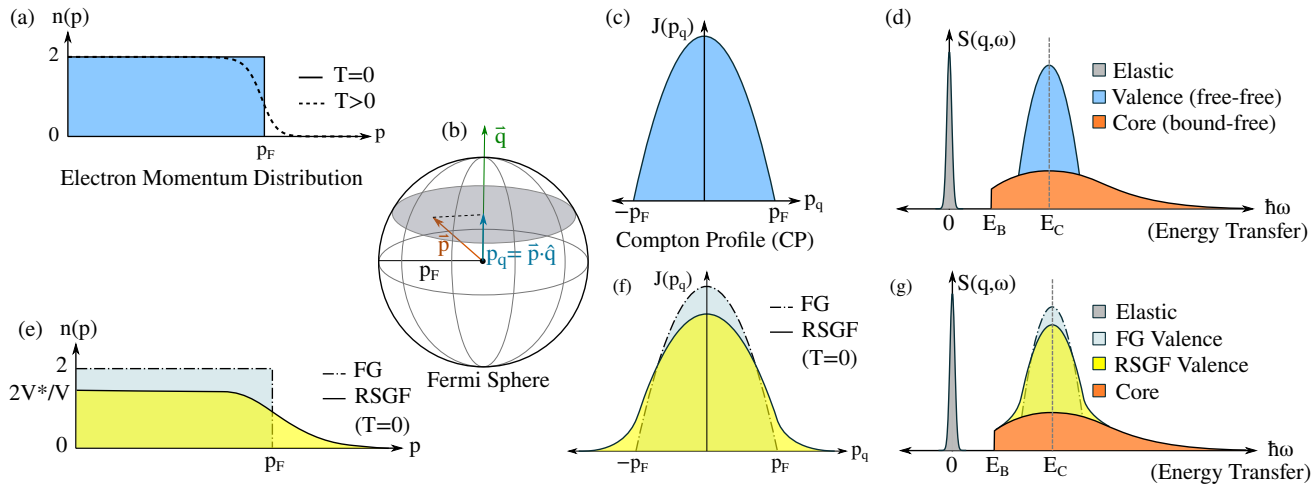

Figure 6.1: Relationship between electronic momentum distribution and nonresonant IXS spectrum in the impulse approximation. (a)-(d): a non-interacting electron gas. (e)-(g) an electron gas with strong electron-ion interaction, such as due to valence-core orthogonalization (VCO). See the text for discussion.

on an issue of central experimental importance: $n(p)$ is a primary experimental observable, appearing as a direct contributor to the dynamic structure factor measured by non-resonant inelastic x-ray scattering (NIXS) in the noncollective scattering regime and subsequently used to infer temperature and density of WDM[107].

NIXS experiments measure the dynamic structure factor $S(q,\omega)$ which determines the relative probability of transferring momentum $\hbar q$ and energy $\hbar\omega$ from the probe radiation to the sample in the scattering process[251]. At large q, the interpretation of NIXS simplifies due to the impulse approximation (IA)[71] wherein the potential before and after the scattering process cancel implying that

$$\hbar\omega = \frac{\hbar^2 q^2}{2m} + \frac{\hbar \mathbf{q}\cdot\mathbf{p}}{m}, \tag{6.1}$$

where $\mathbf{p}$ is the scattering electron's initial momentum. This Doppler broadened Compton scattering is entirely determined by the electronic momentum distribution $n(p)$.

In Fig. 6.1 (a-d), we illustrate the relationship between $n(p)$ and the NIXS spectrum using a simple Fermi gas model for the valence electrons. In panel (a), we show the Fermi radial momentum distribution. This corresponds to the Fermi sphere shown in panel (b). In the shaded intersection between the Fermi sphere and a plane perpendicular to $\mathbf{q}$, the Doppler shift, and thus energy transfer, is identical. The area of this intersection as a function of displacement from the origin $p_q \equiv \mathbf{p} \cdot \hat{\mathbf{q}}$ defines the Compton profile (CP) $J(p_q)$, shown in panel (c). According to Eq. (6.1), the CP is displaced by the Compton shift $E_{\mathrm{C}} = \hbar^2 q^2 / 2m_e$ and stretched by $\hbar q/m$ to obtain $S(q, \omega)$. In panel (d), we show this along with a representative contribution from tightly-bound core electrons (E_B is the core-state binding energy)[193].

Each of temperature, free-electron density, electron-electron interactions and electron-ion interactions influences $n(p)$. As shown in Fig. 6.1(e), interactions, if strong, have a global impact on $n(p)$ and the shape of the CP by moving occupation from states below the single-electron Fermi level to states above, even at $T = 0$. For an interacting Fermi gas at the density of ambient Be, electron-electron correlations result in a promotion of 5% of electrons to states above the Fermi level[163] (See Supplemental Information). As density increases, this effect diminishes. On the other hand, we show here that electron-ion interactions, which already have a stronger influence on electron occupation at ambient conditions[142, 238] (with 20% of electrons promoted above p_F, see Supplemental Information) have a growing, dramatic impact on $n(p)$ as density increases. This effect, and its consequences are shown schematically in Fig. 6.1 (e)-(g) and are presented in detail in the remainder of this letter.

In Fig. 6.2, we present calculations of the spherically-averaged radial momentum distribution $n(p)$ for hcp beryllium at $T = 0$ as a function of atomic density using a real-space Green's function (RSGF) method[194, 234, 233] that treats the electron-ion interaction non-perturbatively, including the effects of VCO. This is compared to calculations for a non-interacting Fermi gas (FG) and to calculations that include electron-ion interactions perturbatively via the BMA[255]. The distribution function shown in Fig. 6.2 is the number of electrons per momentum eigenstate $n(p)$, which is related to the momentum density $\rho(p)$ by $n(p) = ((2\pi)^3/V)\rho(p)$. The abscissa in Fig. 6.2 has been rescaled by the Fermi momentum, p_F to capture the complete density-dependence of the Fermi gas n(p). The

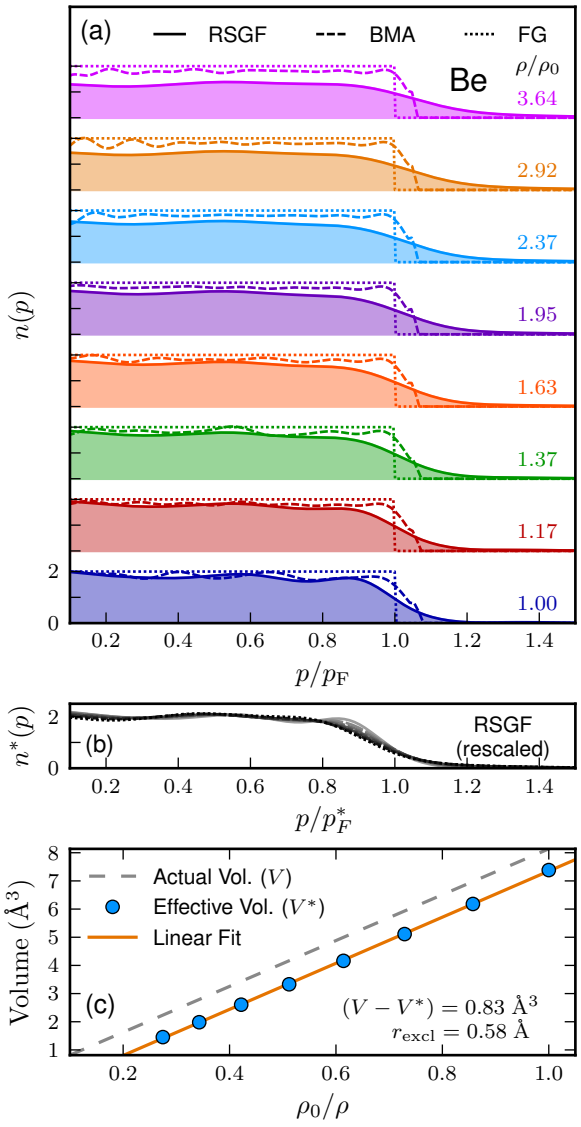

Figure 6.2: Theoretical electronic momentum density of hcp Be as a function of atomic density ρ in terms of ambient density ρ_0. The highest density shown corresponds to a pressure of ~ 8 Mbar[20]. (a) Comparison between calculations using the non-perturbative real-space Green's function method (RSGF), the perturbative Born-Mermin approximation (BMA) and the non-interacting Fermi gas (FG). The momentum p is scaled by the Fermi momentum $p_{\rm F}$. (b) RSGF calculations rescaled by an effective volume determined by the average occupation at low momenta. Curves at higher density are drawn darker. (c) The effective volume per atom as a function of inverse compression.

perturbative electron-ion interaction in the BMA results in a slight decrease in occupation at all momenta compensated for by increased occupation above p_F. Evidently, the bulk of the BMA density dependence is also captured by the rescaling by p_F. The RSGF calculations, on the other hand, show a marked density dependence differing from that of the free or weakly interacting FG. We note two primary features. First, $n(p)$ is nearly uniformly decreased at low p and this depletion gets stronger with increased density. Second, the relative weight of the tail above p_F increases with density.

In Fig. 6.3, we show Compton profiles that correspond to the momentum distributions from Fig. 6.2. The slight reshaping of the RSGF CP relative to the FG at ambient density is in good agreement with high-resolution experimental data[194]. As density increases, the differences between RSGF and FG become quite dramatic: the electron-ion interaction results in a significant reshaping of the CP, shifting weight from the peak out into the high-momentum tails.

The broad, nearly uniform depletion of valence occupation for $p < p_F$ indicates gross changes in the available phase space. Interestingly, these effects have a simple relationship to atomic density that suggests an overwhelming importance of VCO for $n(p)$ of solids or partially-ionized plasmas at high densities. In Fig. 6.2b we show a simple rescaling of all RSGF $n(p)$ by the apparent effective free volume per atom inferred from $\bar{n}$, the average occupancy of $n(p)$ at low p (see Fig. 6.2c), i.e., $V^* = \bar{n}V/2$. The simple offset in the effective volume V^* indicates that the overall phenomenon can be discussed, at least qualitatively, as an excluded volume effect encompassing the strong constraint imposed by VCO on the valence electron wavefunctions in the vicinity of the ion core. Numerically, $V_{\rm excl} = 0.83$ Å^3, which is the volume in which 98% of the $1s$ electrons are contained. There are clear similarities between these results, where VCO with Hartree-Fock bound states has been imposed, and the simpler hard-sphere model introduced by Rousseau and Ashcroft as a heuristic tool for electride formation in Na[241]. In each case, the key physical insight is a substantial constraint on the valence electron wavefunctions over a fixed volume per atom, independent of overall atomic density.

These results establish that calculations of the momentum density function for WDM must necessarily include nonperturbative effects of the electron-ion interaction at the level

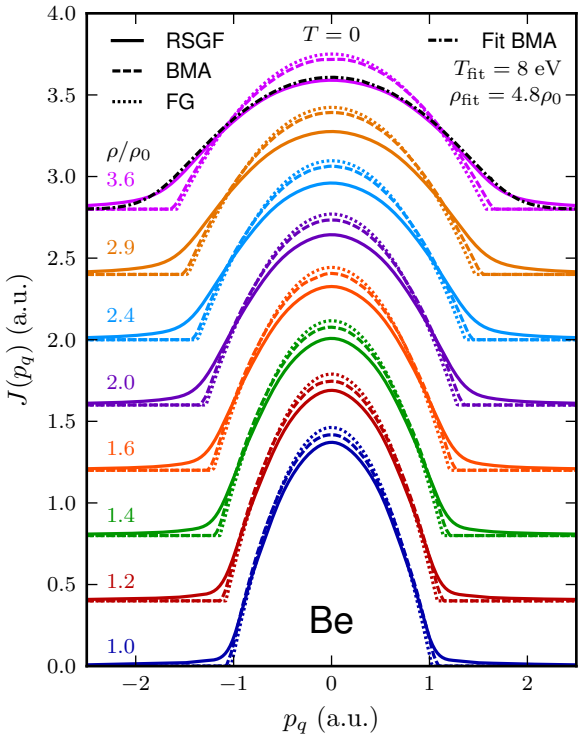

Figure 6.3: Theoretical Compton profiles for Be metal as a function of density at T=0. The real-space Green's function (RSGF, solid curves) is compared to the Born-Mermin Approximation (BMA, dashed lines) and the Fermi gas (FG, dotted lines). In addition, for the highest density, we show the result of fitting a BMA calculation with adjustable temperature and density to the RSGF curve.

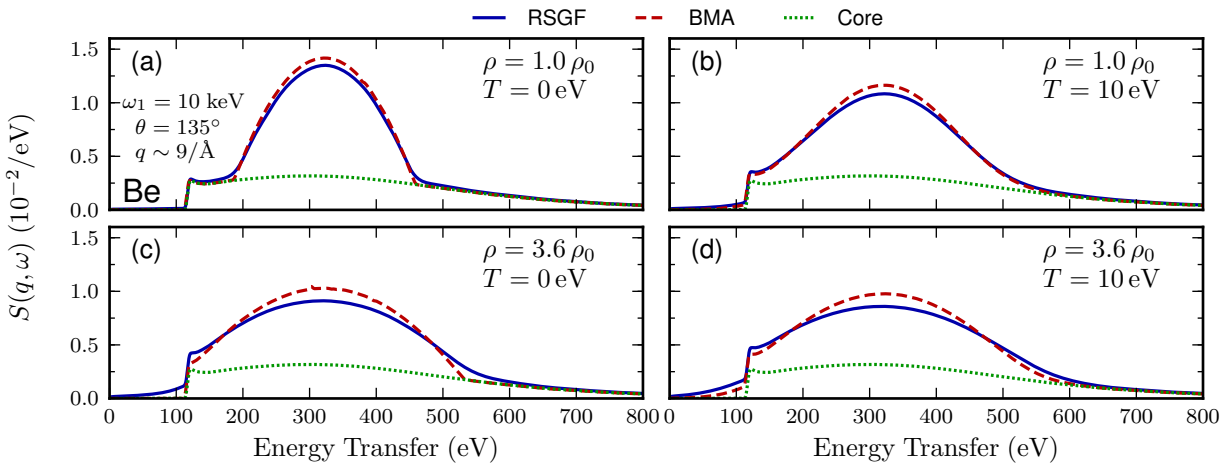

Figure 6.4: Simulated NIXS spectra. (a) Ambient density and temperature (b) Isochoric heating (c) Adiabatic compression (d) Shock Compression/Heating. All curves are for a 10-keV incident energy at 135° scattering angle and include 5-eV broadening.

of wavefunctions or Green's function propagators even well before electride formation is reached. We now discuss the consequences of this observation. First, a full understanding of the consequences of VCO on the EOS or thermodynamic susceptibilities, especially the compressibility, will require further work. That being said, the strong non-free-electron-like modification of $n(p)$, and thus also the kinetic energy[73], with compression makes it clear that its consequences cannot, *a priori*, be ignored.

Second, moving to experimental consequences, we return to Fig. 6.3 where, for the highest-density calculations, we show a fit to the RSGF predictions using the BMA with adjustable ρ and T. The large weight in the RSGF tail is reproduced by the BMA model only when increasing the density by 30% and increasing the temperature from 0 to 8 eV. While the exact consequences for interpretation or reinterpretation of experiment will require further work, the message is clear: failure to include the effects of VCO will result in a systematic overestimate of either T, n_e, or both.

In Fig. 6.4 we compare RSGF and BMA valence contributions to synthetic NIXS spectra under the following four thermodynamic conditions: (a) ambient, (b) isochoric heating, (c) isothermal compression, and (d) shock-compression/heating. High-temperature RSGF calculations were performed by using a finite-temperature exchange-correlation potential[218] and using the Fermi distribution for the occupation of states both in the self-consistency loop and in the final calculation of the Compton profile.[192] The ionic lattice was kept ordered. All curves have been broadened by a 5-eV FWHM Gaussian. At this resolution, which is attainable using the seeded source at LCLS, the effects of VCO on the Compton profile should be measurable.

One interesting future direction is to investigate the corresponding momentum-space phenomenon associated with the real-space segregation of valence charge density in proposed electride phases. It may be the case that electride formation can be more easily observed, especially in disordered systems, by its influence on $n(p)$ rather than by its slight modification of the static structure factor $S(q)$ in elastic scattering.

In conclusion, we have shown that non-perturbative effects of the electron-ion interaction, such as core-valence orthogonalization, play an increasingly important role in determining the momentum distribution of free electrons in ordered dense matter as density is increased. This will have a profound effect on the interpretation of NIXS-based diagnostic measurements of WDM, and may also be relevant for thermodynamic properties of dense, partially ionized plasmas.

6.1 Supplemental Information

In Fig. 6.5, we give compare the RSGF momentum distribution with that for an interacting electron gas at the corresponding density. Occupation numbers for the interacting electron gas were calculated by integration of the electron spectral function. Correlation effects were included using a cumulant expansion for the electron Green's function[163], where the cumulant function was derived to first order in the screened coulomb interaction. The calculations assumed a free electron gas with a Wigner-Seitz radius $r_s = 1.87$ for Be at ambient density, and $r_s = 1.22$ for 3.6× ambient density. The RSGF calculations neglect electron-electron correlations.

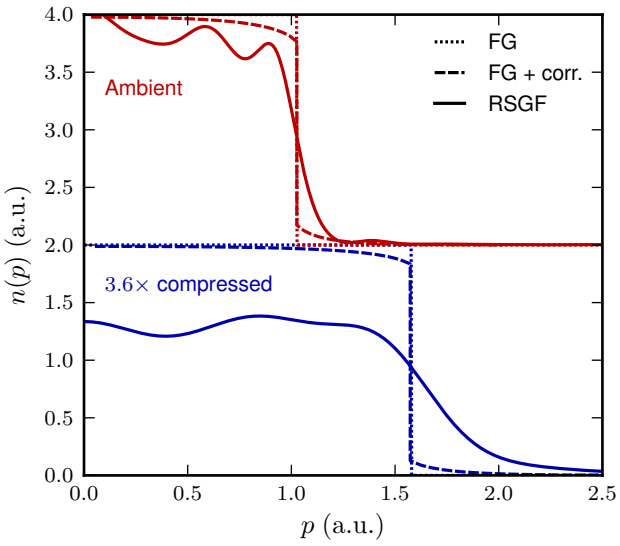

Figure 6.5: Momentum distribution $n(p)$ for an non-interacting gas (FG), interacting electron gas (FG + corr) and for the solid, neglecting correlations (RSGF).

	FG + corr.	RSGF
Ambient	0.10	0.36
Compressed	0.08	0.75

Table 6.1: Number of electrons promoted above p_F (out of 2 total electrons).

For quantitative comparison, Table 6.1 shows the number of electrons promoted above the Fermi level,

$$\frac{V}{(2\pi)^3}\int_{p_F}^{\infty} p^2 n(p) dp. \tag{6.2}$$

The corresponding Compton profiles are shown in Fig. 6.6. At ambient density, the effect of correlations is smaller than that of the electron-ion interaction, but is by no means negligible. However, at higher densities, the electron-ion interaction clearly dominates over electron-electron correlations.

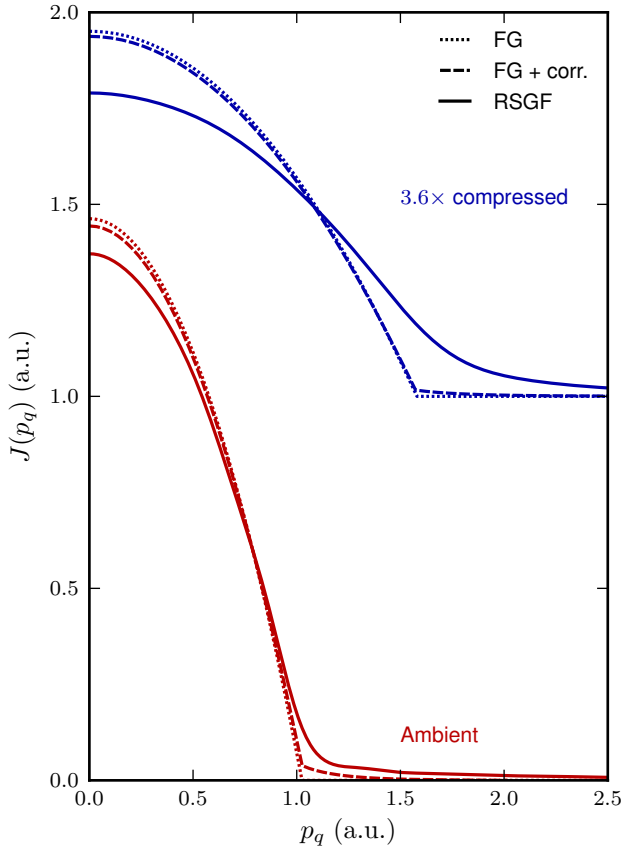

Figure 6.6: Compton profile $J(p_q)$ for an non-interacting gas (FG), interacting electron gas (FG + corr) and for the solid, neglecting correlations (RSGF).

Chapter 7

THEORETICAL TREATMENTS OF THE BOUND-FREE CONTRIBUTION AND EXPERIMENTAL BEST PRACTICE IN X-RAY THOMSON SCATTERING FROM WARM DENSE MATTER

(*Originally published as:* B. A. Mattern and G. T. Seidler, Phys. Plasmas **20**, 022706 (2013))

By comparison with high-resolution synchrotron x-ray experimental results, we assess several theoretical treatments for the bound-free (core-electron) contribution to x-ray Thomson scattering (i.e., also known as nonresonant inelastic x-ray scattering). We identify an often overlooked source of systematic error in the plane-wave form factor approximation (PWFFA) used in the inference of temperature, ionization state, and free electron density in some laser-driven compression studies of warm dense matter. This error is due to a direct violation of energy conservation in the PWFFA. We propose an improved practice for the bound-free term that will be particularly relevant for XRTS experiments performed with somewhat improved energy resolution at the National Ignition Facility or the Linac Coherent Light Source. Our results raise important questions about the accuracy of state variable determination in XRTS studies, given that the limited information content in low-resolution XRTS spectra does not strongly constrain the models of electronic structure being used to fit the spectra.

7.1 Introduction

The field of *warm dense matter* (WDM) rests in the transitional regime between traditional condensed phase systems and strongly-correlated, fully-ionized plasmas. As such, it draws from the complexity of both fields while showing its own special fundamental and, as we show here, pragmatic challenges. A significant and growing literature exists on the electronic structure,[115, 113, 66, 262, 220] thermodynamics[112] and hydrodynamics[191] of WDM, in addition to a range of applications in fusion energy science[188] and laboratory astrophysics.[236, 297] Here, however, we investigate a particular difficulty of the WDM

regime: assessing the accuracy of the experimental determination of the basic state variables of the system, such as temperature, density and ionization state. Reliable inference of these quantities is central to the clearly-needed improvements in the equation of state of materials under, for example, the entire range of conditions leading from ambient matter to inertial confinement fusion.[197]

The high optical opacity of WDM requires the use of penetrating probe radiation, i.e., x-ray photons with energies of a few to a few tens of keV. Unfortunately, with only few counterexamples[61] the inference of state-variables using these methods is limited by the degree of understanding of the electronic structure of WDM and its relationship to the state variables themselves. Faintly circular co-dependencies of this type are not uncommon in emergent fields of experimental science (e.g., consider the many years of effort needed to establish accurate and precise pressure sensing in the Mbar range in opposed-anvil pressure cells[93, 219, 119, 227]), and a firm foundation for such methodologies can follow from any of several developments. Foremost among such developments are: experimental data of sufficient information content to itself strongly constrain the constituent theories for electronic structure; broad programs to assess accuracy by cross-comparison of different metrologies; and, finally, an eventual comparison to international standards. The experimental determination of state variables in the WDM regime is seeing only the earliest such examples, including notably the rare experiments using detailed balance in x-ray Thomson scattering[61] or the recent checks in consistency between conclusions drawn from the elastic and inelastic components of x-ray scattering.[96]

The present paper reports a first step in evaluating the accuracy, rather than precision, of the methods used for state variable determination in the WDM regime. To this end, we investigate the various available treatments for the core-electron, or bound-free, contribution to x-ray Thomson scattering (XRTS, also called nonresonant inelastic x-ray scattering, NIXS[251]) with a special emphasis on the plane-wave form-factor approximation (PWFFA) of Schumacher, et al.[252]. We will show that this approximation, which has seen extensive use in XRTS studies of shock-compressed matter,[240, 249, 243, 107, 174, 173, 96]is fundamentally flawed and presents a source of systematic uncertainty in inferred quantities.

Based on these observations we come to three main conclusions. First, looking to the near

future, when XRTS studies of WDM with improved energy resolution will be performed at the Linac Coherent Light Source[126] and the National Ignition Facility[197], the errors implicit in the use of the PWFFA must be avoided if physically meaningful information on the equation of state in the WDM regime is to be determined. Second, while it is important to note that a faulty theoretical treatment has been used, and that some reevaluation of experimental results may be called for, the more lasting conclusion is that the information content in the measured XRTS spectra for WDM has been insufficient to alert the experimenters to the presence of an unphysical model for the electronic structure. This strongly suggests the need for cross-comparison with alternative methods of WDM state variable determination, e.g., x-ray fluorescence thermometry[299, 256, 266, 204, 185, 285]. Third, we find that stronger connections between the synchrotron x-ray and WDM-XRTS communities provide important experimental and theoretical synergies. The wealth of very high-resolution studies at synchrotron light sources of both the free-free (valence) [51, 144, 287, 149, 146, 121, 209, 248] and bound-free (core) [251, 32, 36, 34, 244, 81, 271, 91, 110, 13, 83, 78, 184, 294] contributions to XRTS provide important benchmarks both for comparison to WDM-specific theory and also for validation of experimental protocol including, e.g., instrument-specific backgrounds. Further, as we have illustrated here, there will be cases where theoretical methods already in use for synchrotron studies may be beneficially transported to WDM-XRTS studies.

In Sect. 7.2 we discuss four theoretical treatments of bound-free XRTS: the impulse approximation (IA), which is valid at large energy transfer; a hydrogenic model (HM); an extension of the IA to incorporate binding energies (PWFFA); and a real-space Green's function method (RSGF). The first three are essentially atomic (with varying degrees of approximation), while the latter treats the condensed solid, and is based on methods broadly used for many years in the interpretation of several x-ray spectroscopic techniques. [233, 234]

Since high-resolution XRTS data from WDM at known thermodynamic conditions is currently unavailable, we instead compare each of the above theories with very high-quality XRTS spectra collected under ambient conditions at a synchrotron x-ray source. This provides a baseline validation for the core contribution: a theoretical treatment which fails under these conditions is certain to form a weak foundation when including the further

complexities of continuum lowering and partial ionization present in WDM.

Experimental details are described in Sect. 7.3 and the comparison of theory and experiment is made in Sect. 7.4.1. The relative success of even atomic treatments at describing the condensed solid suggests that these methods should be extensible to the WDM regime with only minor modifications. However, we find that the PWFFA, which has been used for a few years in the interpretation of WDM measurements,[240, 249, 243, 107, 174, 173, 96]is in stark disagreement with the ambient experimental data. In Sect. 7.4.2, we show that this disagreement is due to internal inconsistency in the PWFFA that leads to unphysical results. Next, in Sect. 7.4.3, we consider the implications of using the PWFFA to model the bound-free contribution to WDM XRTS data; namely, the likelihood of previously-undiagnosed systematic errors in extracted thermodynamic quantities. These observations then motivate a discussion of best future practice in Sect. 7.4.4, after which we conclude in Sect. 7.5.

7.2 Theory

The fundamental observable in XRTS/NIXS is the *dynamic structure factor* $S(\mathbf{q},\omega)$, which separates into independent contributions from electrons in different shells. We will focus on the contribution from tightly bound core electrons, i.e., the *bound-free* contribution. The theoretical description of bound-free XRTS begins with the Kramers-Heisenberg formula for the first-Born approximation to the double-differential scattering cross-section (DDSCS):[251]

$$\frac{d^2\sigma}{d\omega d\Omega} = \frac{\omega_2}{\omega_1} r_o^2 \left|\hat{\epsilon}_1 \cdot \hat{\epsilon}_2^*\right|^2 S(\mathbf{q},\omega) \tag{7.1}$$

$$S(\mathbf{q},\omega) = \sum_I P_I(T) \sum_F \left| \langle F| \sum_j e^{i\mathbf{q}\cdot\mathbf{r}_j} |I\rangle \right|^2 \times \delta(E_F - E_I - \omega) \tag{7.2}$$

Here, $\omega_{1,2}$ and $\hat{\epsilon}_{1,2}$ are initial and final photon energies and polarizations; r_0 is the Thomson scattering length; $|I\rangle$,$|F\rangle$ are initial and final many-body states with energies E_I,E_F; $P_I(T)$ is the temperature-dependent Boltzmann factor; $\mathbf{q}$ is the momentum transfer; $\omega = \omega_1 - \omega_2$ is the energy transfer and j indexes individual electrons. In this and subsequent formulae,

we use Hartree atomic units ($\hbar = m_e = 1$).

In the independent particle approximation, Eq. (7.2) can written as

$$\begin{aligned} S(\mathbf{q},\omega) &= \sum_i n_i S_i(\mathbf{q},\omega) \\ S_i(\mathbf{q},\omega) &= \sum_f (1-n_f) \left|\langle f| e^{i\mathbf{q}\cdot\mathbf{r}} |i\rangle\right|^2 \delta(E_f - E_i - \omega), \end{aligned} \tag{7.3}$$

where $|i\rangle$,$|f\rangle$ are initial and final state *single particle* states with energies E_i,E_f and thermally-averaged occupation numbers n_i, n_f.

7.2.1 The impulse approximation

In the limit of large energy-transfer ω relative to the initial state binding energy E_B, known as the impulse approximation (IA), the XRTS spectrum is completely determined by the initial-state electronic momentum distribution; the binding energy of the scattering electron plays no role.[71]

For $\omega \gg E_B$, only unoccupied final states contribution to Eq. (7.3), so we set $n_f = 0$. Next, following Eisenberger and Platzman,[71] we expand the δ-function using the standard Fourier representation

$$\delta(\omega) = \int \frac{dt}{2\pi} e^{i\omega t}. \tag{7.4}$$

After rearranging slightly and using the fact that $|i\rangle$ and $|f\rangle$ are eigenstates of the single-particle Hamiltonian H, we find

$$\begin{aligned} S_i(\mathbf{q},\omega) &= \int \frac{dt}{2\pi} \sum_f e^{i\omega t} \langle i| e^{iHt} e^{-i\mathbf{q}\cdot\mathbf{r}} e^{-iHt} |f\rangle \langle f| e^{i\mathbf{q}\cdot\mathbf{r}} |i\rangle \\ &= \int \frac{dt}{2\pi} e^{i\omega t} \langle i| e^{iHt} e^{-i\mathbf{q}\cdot\mathbf{r}} e^{-iHt} e^{i\mathbf{q}\cdot\mathbf{r}} |i\rangle . \end{aligned} \tag{7.5}$$

In the second line, we have used completeness to remove the sum over final states. The IA corresponds to replacing H by the free-particle Hamiltonian H_0, which can be justified in the limit of $(\omega/E_B)^2 \gg 1$ (see Section III of Ref. 71). After inserting a complete set of momentum eigenstates and integrating over the direction of momentum, we obtain

$$S_i(\mathbf{q},\omega) = (2\pi/q) \int_{|w/q - q/2|}^{\infty} p\, dp\, \rho_i(p), \tag{7.6}$$

where $\rho_i(p) = (2\pi)^{-3} |\langle i|p\rangle|^2$ is the initial-state momentum density, which is here assumed to be isotropic (e.g. s-shell, or sum over a filled subshell).

This formula can be interpreted as describing XRTS from a gas of free electrons with the same initial-state momentum distribution. The scattering spectrum consists of a line centered at the free-particle Compton shift $\omega_c = q^2/2$ that is Doppler broadened by the projection of the momentum distribution along the direction of $\mathbf{q}$. The integral over the momentum distribution in Eq. (7.6) simply counts electrons with a given momentum-projection p_q determined by the energy transfer.

We now turn to methods that take the binding energy into account.

7.2.2 Hydrogenic Model

It is possibly to analytically evaluate Eq. (7.3) using hydrogenic initial and final states. For a $1s$ initial state, the result is[71]

$$S_i(q,\omega) = \int \frac{d^3p}{(2\pi)^3} |\langle f| e^{i\mathbf{q}\cdot\mathbf{r}} |i\rangle|^2 \delta(\omega - E_B - p^2/2), \tag{7.7}$$

with

$$\begin{aligned} |\langle f| e^{i\mathbf{q}\cdot\mathbf{r}} |i\rangle|^2 &= \frac{\pi^2 8^3 a^2}{p}(1 - e^{-2\pi/pa})^{-1} \\ &\times \exp\left[\frac{-2}{pa}\tan^{-1}\left(\frac{2pa}{1+(q^2a^2)-p^2a^2}\right)\right] \\ &\times \left[k^4a^4 + (1/3)k^2a^2(1+p^2a^2)\right] \\ &\times \left[(k^2a^2+1-p^2a^2)^2 + 4p^2a^2\right]^{-3}. \end{aligned} \tag{7.8}$$

Here, p is the final-state momentum, $a = 1/Z$ where Z is the effective nuclear charge[45], and $E_B = 1/2Z^2$ is the binding energy. In this expression, contributions from bound final states have been neglected. Expressions for shells other than the $1s$ are included in Schumacher, et al.[252] , where this method is referred to as the *hydrogenic form-factor approximation.* We will, however, refer to this simply as the hydrogenic model (HM).

7.2.3 Plane-wave form-factor approximation

The *plane-wave form-factor approximation* (PWFFA) is an attempt to improve the IA by including the binding energy in the kinematics. The final states are assumed to be momen-

tum eigenstates, which is conceptually appealing in the context of dense plasmas where the jellium model has found wide application. However, as we demonstrate in Sect. 7.4.2, a fundamental difficulty arises: this approximation effectively evaluates the initial-state energy using the atomic Hamiltonian, while evaluating the final-state energy using the free-particle Hamiltonian. This inconsistent treatment violates energy conservation, resulting in violations of the Bethe f-sum rule and deviations from experimental results that, although small in the original context of gamma-ray scattering, are quite large under the kinematic conditions typical of XRTS measurements. It is the use of the PWFFA in the interpretation of recent XRTS experiments on WDM[240, 249, 243, 107, 174, 173, 96]that motivates the present paper.

Schumacher's derivation of the PWFFA[252] makes the following assumptions:

$$\begin{aligned} |f\rangle &= |\mathbf{p}+\mathbf{q}\rangle \\ \sum_f &\rightarrow \int \frac{d^3p}{(2\pi)^3} \\ E_f &= E_{\mathbf{p}+\mathbf{q}} = \frac{(\mathbf{p}+\mathbf{q})^2}{2} \\ E_i &= -E_B \end{aligned} \tag{7.9}$$

where E_B is the initial-state binding energy, $\mathbf{p}$ is the initial-state momentum and $\mathbf{p}+\mathbf{q}$ is the final-state momentum. Assuming that $T=0$ and applying (7.9) to (7.3), we find

$$\begin{aligned} S_i(\mathbf{q},\omega) &= \int \frac{d^3p}{(2\pi)^3} \left|\langle \mathbf{p}+\mathbf{q}| \, e^{i\mathbf{q}\cdot\mathbf{r}} \, |i\rangle\right|^2 \delta(E_{\mathbf{p}+\mathbf{q}} + E_B - \omega) \\ &= \int \frac{d^3p}{(2\pi)^3} \left|\langle \mathbf{p}|i\rangle\right|^2 \delta(E_{\mathbf{p}+\mathbf{q}} + E_B - \omega) \\ &= \int d^3p \rho_i(\mathbf{p}) \delta(E_{\mathbf{p}+\mathbf{q}} + E_B - \omega) \end{aligned} \tag{7.10}$$

In the second line we use the fact that $e^{i\mathbf{q}\cdot\mathbf{r}}$ is a momentum translation operator. The last line uses the definition of the momentum density $\rho_i(\mathbf{p}) = (2\pi)^{-3}\left|\langle\mathbf{p}|i\rangle\right|^2$. Furthermore, if we again restrict ourselves to an isotropic momentum density (e.g., s-shell, or sum over a filled subshell), we can perform the angular integrals to obtain

$$S_i(\mathbf{q},\omega) = (2\pi/q) \int_{|\sqrt{2(\omega-B)}-q|}^{\sqrt{2(\omega-B)}+q} p \, dp \, \rho_i(p) \tag{7.11}$$

This expression, along with (7.1) differs from Schumacher's[252] Eqs. (5) and (21) only in that it does not contain the relativistic prefactor $\sqrt{1+(p/mc)^2}$, which for the experimental conditions under consideration differs negligibly from unity.

Eq. (7.11) has the same form as the IA expression Eq. (7.6), differing only by the bounds on the integration over the momentum density. Given this similarity and the well-tested validity of the IA in its regime of applicability, one would expect that for $\omega \gg E_B$ the PWFFA would reproduce the IA. This is, however, not the case — despite claims in the literature to the contrary.[252, 107] We will return to this point in Sect. 7.4, after comparison with experiment.

7.2.4 The real-space Green's function method

The prior methods have all treated XRTS for an isolated atom to various degrees of approximation. The next method we describe treats an arbitrary cluster of atoms using a real-space Green's function (RSGF) formalism implemented in recent versions of the x-ray spectroscopy code `FEFF` .[263] This formalism, which can treat complex, aperiodic systems, has been extensively applied to condensed-matter systems, where XRTS/NIXS provides a bulk-sensitive alternative to, and extension of, soft x-ray absorption spectroscopy, [263, 272, 270, 13, 79, 89, 225] The RSGF approach has recently been extended to treat the valence contribution.[194]

Starting with a description of atomic species and locations, an effective one-particle Green's function for the valence electrons in the cluster of atoms is calculated in the muffin-tin approximation, including the effects of full multiple scattering[234]. This Green's function implicitly contains the excited electronic states that are the final states in the scattering experiment. In terms of a spectral density matrix defined by $\rho(E) = \sum_f |f\rangle \langle f| \, \delta(E - E_f)$, which is related to the Green's function by $\langle \mathbf{r}| \, \rho(E) \, |\mathbf{r}'\rangle = -(1/\pi) \operatorname{Im} G(\mathbf{r}', \mathbf{r}, E)$, Eq. (7.3) can be recast as

$$S_i(\mathbf{q}, \omega) = \langle i| \, e^{-i\mathbf{q}\cdot\mathbf{r}'} P \rho(E) P e^{i\mathbf{q}\cdot\mathbf{r}} \, |i\rangle \, . \tag{7.12}$$

Here $E = \omega + E_i$ is the photoelectron energy and P projects the final states (which are calculated in the presence of a core hole) onto the unoccupied states of the initial-state

Hamiltonian (which has no core hole).[263] The Green's function can be separated into contributions from the central atom and from scattering off other atoms in the cluster. Likewise, the dynamic structure factor can be factored as

$$S_i(\mathbf{q},\omega) = S_0(q,\omega)[1+\chi_{\mathbf{q}}(\omega)], \tag{7.13}$$

where $S_0(q,\omega)$ is a smoothly varying, isotropic atomic background and $\chi_{\mathbf{q}}$ is the fine structure due to all orders of photoelectron scattering from the environment.[263, 83] Implicit in the fine structure is information about nearest-neighbor distances and thus also density[263]. However, at the poor experimental resolution typical of WDM measurements[107], this structure will be washed out. Thus, for our purposes, we will include only the atomic background contribution, $S_0(q,\omega)$.

7.3 Experiment

Although we are ultimately interested in the elevated temperatures and densities of WDM, it is important to first validate theoretical methodology against spectra taken under known thermodynamic conditions and at higher resolution than presently typical of WDM experiments. To this end, experimental XRTS data for polycrystalline Be at ambient temperature and pressure were collected using the lower energy resolution inelastic x-ray (LERIX) spectrometer at beamline 20-ID of the Advanced Photon Source.[84] Scattered photons with $\omega_2 = (9891.7 \pm 0.2)$ eV were analyzed by a single spherically bent Si crystal located at a fixed 171° scattering angle while scanning the incident photon energy. From the elastic peak width the total instrumental resolution was determined to be 1.3 eV. The data, which have previously been reported[194], are shown in Fig. 7.1. The graph is labelled $S(q_\theta,\omega)$ to indicate that the data are collected at fixed scattering angle, and thus q is a weak function of ω.

After normalizing to the incident flux, a small linear background and a single scale factor were fit in order to match the RSGF core calculation in the tail region ($800 < \omega < 1500$ eV) and thus put the data into absolute units. The results of this fit have been used to scale the experimental data in Fig. 7.1. Additionally, theoretical core and valence calculations, the fit linear background, and the sum of these three are shown.

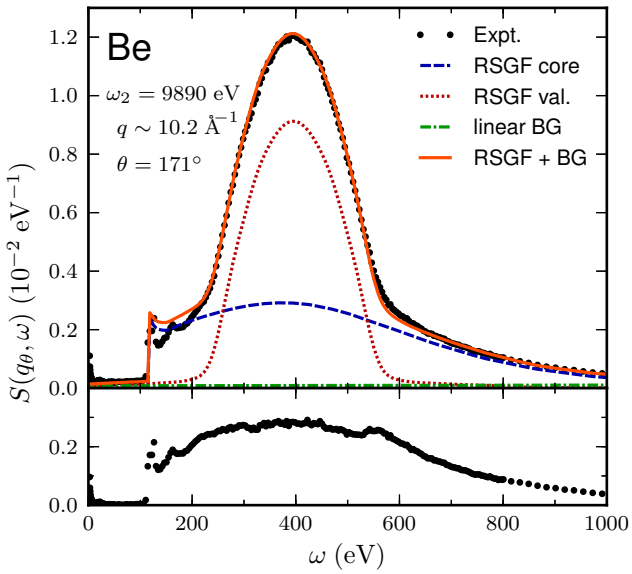

Figure 7.1: (Color online.) XRTS from polycrystalline beryllium under ambient conditions at a fixed 171° scattering angle and 9890-eV scattered photon energy[194]. Here, the energy transfer ω is the difference between the incident and scattered photon energies. In the upper panel, the data are shown along with a combined real-space Green's function (RSGF) valence and core calculation. The data have been scaled as described in the text. In the lower panel, the valence contribution and linear background have been subtracted to give the core contribution alone.

The experimental generalized oscillator strength $\int(2/q^2)\omega S(q,\omega)d\omega$ matches that for the combined theoretical RSGF spectrum to within 1%. Since the measurement was performed at fixed scattering angle, this value is slightly larger than the Bethe f-sum rule[251, 151, 293] value of N=4 (which only holds for experiments performed at fixed q).

The theoretical valence profile, calculated from the RSGF,[194] was then subtracted to obtain the experimental core profile, shown in the lower panel of Fig. 7.1. The small peak visible for $550 < \omega < 650$ eV is a result of the theoretical valence profile underestimating the actual contribution in this region, as was also seen in comparisons with higher momentum-transfer data (see Figs. 4 and 5 of Mattern, et al.[194]).

7.4 Results and Discussion

7.4.1 Comparison of Experiment and Theory

The extracted experimental core profile is compared in Fig. 7.2 to to each of the four theoretical calculations discussed in Section 7.2. All calculations are in absolute units and have taken the weak dependence of q on ω into account. Vertical guides are included at the $1s$ binding energy (112 eV) and the free-particle Compton shift (396 eV).

The IA and PWFFA calculations use the ground-state Dirac-Fock Be $1s$ wavefunction calculated using `FEFF` 's atomic solver as the initial state, and thus only differ in their treatment of the final states and energy conservation. For the RSGF calculation, the Dirac-Fock wavefunction is calculated in the presence of a $1s$ core-hole. We have included only the atomic background contribution $S_0(q,\omega)$. The fine structure visible in the experimental data for $\omega \lesssim 200$ eV is not included, although it has been treated elsewhere.[263] The HM calculation uses hydrogenic wavefunctions with an effective nuclear charge (Z=3.685)[45] for the initial and final states.

We focus on three regions for comparison: the vicinities of the K-edge binding energy ($\omega \sim 112$ eV), the peak ($\omega \sim 396$ eV), and the tail ($\omega \gtrsim 600$ eV). The RSGF calculation matches the data reasonably well in all three regions (with the exception of immediately above the K edge, where interference effects have been omitted). The HM accurately describes the peak and tail regions, but shows a large deficit above the experimental binding

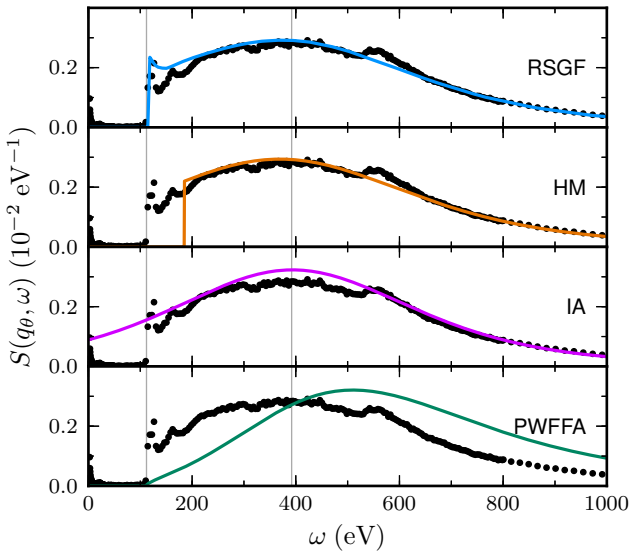

Figure 7.2: (Color online.) Comparison of extracted core-shell XRTS with theoretical calculations using the RSGF, the hydrogenic model (HM), impulse approximation (IA), and plane-wave form-factor approximation (PWFFA). The energy transfer ω is the difference between the incident and scattered photon energies. *All calculations are in absolute units.* Vertical guides are shown at the $1s$ binding energy (112 eV) and the free-particle Compton shift (396 eV).

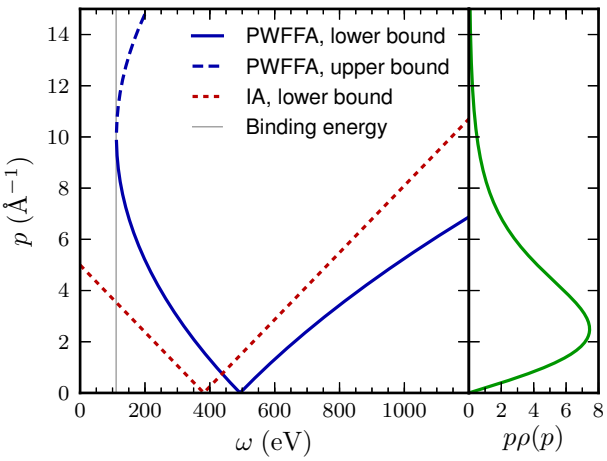

Figure 7.3: (Color online.) On the left are shown the integration bounds for both the PWFFA (upper and lower bounds) and IA (lower only, upper bound is ∞) calculations. On the right, plotted vertically, is the integrand $p\rho(p)$. Both the offset of the peak by the binding energy (112 eV) and the lack of convergence of the PWFFA to the IA at large ω are apparent.

energy due to the larger binding energy of the hydrogenic state. The IA, which ignores the binding energy, has an unphysical tail at low energy transfers. The peak region is reasonably well described by the IA, while the high-ω tail region is quite accurate. This is expected since the conditions of applicability of the IA are well satisfied for large energy transfer.

By contrast, although the PWFFA of Schumacher, et al.[252] vanishes below K edge, it exhibits only a gradual onset and further shows strong quantitative and qualitative disagreement with the experimental data everywhere else. Given its application in the interpretation of several XRTS experiments[240, 249, 243, 107, 174, 173, 96]on WDM, and its evident failure to describe high-resolution synchrotron measurements, we now turn our focus to the PWFFA. We will first look in more detail at the source of the approximation's error, and then briefly discuss the possible implications for interpretation of experiment and future best practice.

7.4.2 A closer look at the PWFFA

Although others have previously observed that the PWFFA gives results with unphysical features that are in disagreement with experimental data,[53, 18] we are unaware of a discussion of the origin of the approximation's inconsistency. We now consider this point in detail.

An alternative route to obtain the PWFFA is to follow the IA derivation up to Eq. (7.5). At this point, if one makes the *ad hoc* approximation of replacing only the second H by H_0,

$$S_i(\mathbf{q},\omega) \approx \int \frac{dt}{2\pi} e^{i\omega t} \left\langle i\right| e^{iHt} e^{-i\mathbf{q}\cdot\mathbf{r}} e^{-iH_0 t} e^{i\mathbf{q}\cdot\mathbf{r}} \left|i\right\rangle . \tag{7.14}$$

then, instead, the PWFFA result (7.11) follows. Thus, the assumptions (7.9) correspond to making the uncontrolled approximation of evaluating the initial-state energy using H and the final-state energy using H_0. This effectively violates energy conservation, opening the possibility of unphysical results.

As we mentioned in Sect. 7.2.3, the IA (7.6) and PWFFA (7.11) results differ only in the bounds of the integration over the momentum density. In left panel of Fig. 7.3, we show the integration bounds as a function of ω for both theories. For the IA, there is no upper bound, and for the PWFFA the upper bound is only relevant for small ω, beyond which it is

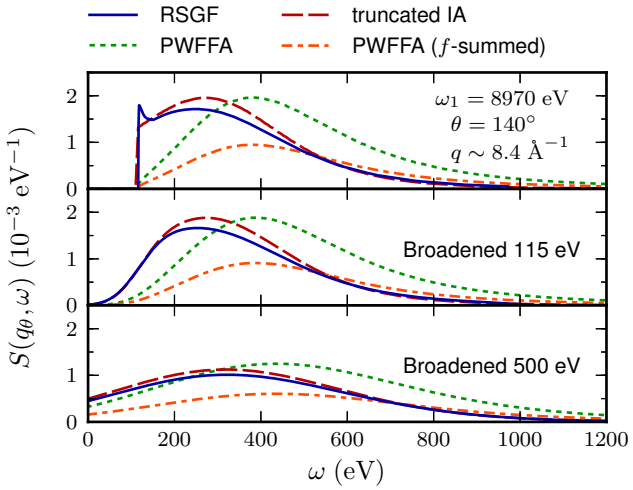

Figure 7.4: (Color online.) Theoretical core profiles for the experimental conditions of Fortmann, et al.[96]. The inaccuracy of the PWFFA remains, even after substantial broadening.

well above the integrand's region of support. The right panel shows the integrand (rotated so that the abscissa runs vertically). The scattering spectra can be seen to peak when the lower integration bound vanishes. For the PWFFA, this is offset to higher energy transfer by the binding energy of the initial state. Furthermore, the failure of the PWFFA to reduce to the IA at large ω can be clearly seen here. The offset of the PWFFA peak relative to the IA appears to be in conflict with the calculations presented in Fig. 3 of Riley, et al.[240].

Given the much lower energy resolution typical of WDM experiments, it is natural to ask whether the discrepancies seen above are relevant in that context. In Fig. 7.4, we compare RSGF, IA and PWFFA calculations at the representative experimental conditions of Fortmann, et al.[96]. The IA calculation has been truncated at the empirical binding energy. In addition to the absolute-unit PWFFA calculation, we have included a curve scaled to match the f-sum of the other theoretical curves. The unbroadened calculations are shown in the upper panel. The curves in the middle panel are broadened by 115-eV (FWHM) to match the experimental resolution of Ref. 96. Finally, for illustrative purposed, the lower panel contains curves broadened by 500 eV. Even in the latter, admittedly extreme case,

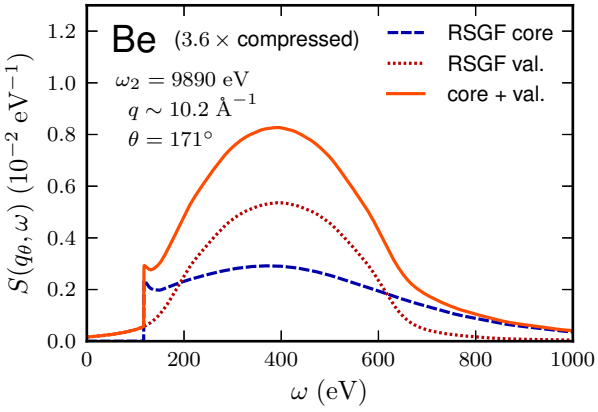

Figure 7.5: (Color online.) Theoretical (RSGF) XRTS from polycrystalline Be compressed to 3.6× ambient density. The valence contribution is broader than under ambient conditions (*cf.* Fig. 7.1, top panel). Subsequently, the core contribution (assumed here to be independent of density) is relatively larger in the region of the peak.

the PWFFA offset and subsequent overestimation of the high-ω tail is still quite prominent. The *ad hoc* f-sum scaling results in a tail that is only slightly overestimated, but at the cost of an extreme deficit beneath the peak.

At the higher densities typical of WDM, the core contribution becomes even more important. As the density is increased, the Fermi level increases relative to the bottom of the valence band resulting in a broader valence contribution. The core wavefunction, on the other hand, is only weakly dependent on density (at least for modest compression, where the cores from neighboring sites have negligible overlap). Subsequently, as shown in Fig. 7.5 (*cf.* Fig. 7.1, top panel), the core contribution is relatively larger in the peak region, increasing the importance of a numerically accurate theoretical treatment.

7.4.3 Implications

We now turn to implications of an incorrect core treatment on the interpretation of XRTS spectra from WDM. It is important to recognize the difficulty of these experiments and their

analysis. The intrinsic width of backlighter x-ray sources fundamentally limits the energy resolution obtainable in this measurement technique. The low flux and need for single-shot measurement requires the use of low-resolution spectrometers with limited spectral range further decreasing the resolution while also complicating background characterization. This uncertainty in the background subtraction makes f-sum normalization especially difficult, and thus the spectra often can not be reliably placed into absolute units. Furthermore, the highest likelihood background is necessarily dependent upon assumptions made about the core contribution to the spectrum.

The complicated interplay between the various degrees of freedom present in such fits makes it difficult to state the exact implications of using the PWFFA in the extraction of thermodynamic state variables in published work.[240, 249, 243, 107, 174, 173, 96]It is likely that, in order for a good fit in the high-ω tail to be obtained, the ionization state must be overestimated. This could explain the discrepancy noted by Fortmann, et al.,[96] between their best-fit ionization state found using the PWFFA and earlier work that appears to use the HM.[181, 106] Beyond that, the net effect on extracted thermodynamic parameters is unclear. However, due to this previously undiagnosed systematic uncertainty, re-evaluation of existing experimental data[240, 249, 243, 107, 174, 173, 96]using a more appropriate core calculation and a maximum likelihood treatment of the background is necessary.

7.4.4 Future Practice

The limitations of the PWFFA bring up the question of best future practice for fitting the core-shell XRTS from WDM. This will become particularly important when higher resolution WDM-XRTS experiments are performed at the Linac Coherent Light Source and the National Ignition Facility. If such experiments are to reach their full scientific potential, errors on the scale of those given by the PWFFA must be avoided. An ideal treatment would include self-consistent determination of occupied and unoccupied electronic states including condensed-phase effects. Also, the decrease of ionization potentials with increased density (i.e., *continuum lowering*) should be either implicitly present in the calculation, or tunable using models from plasma physics.[70, 273, 300]

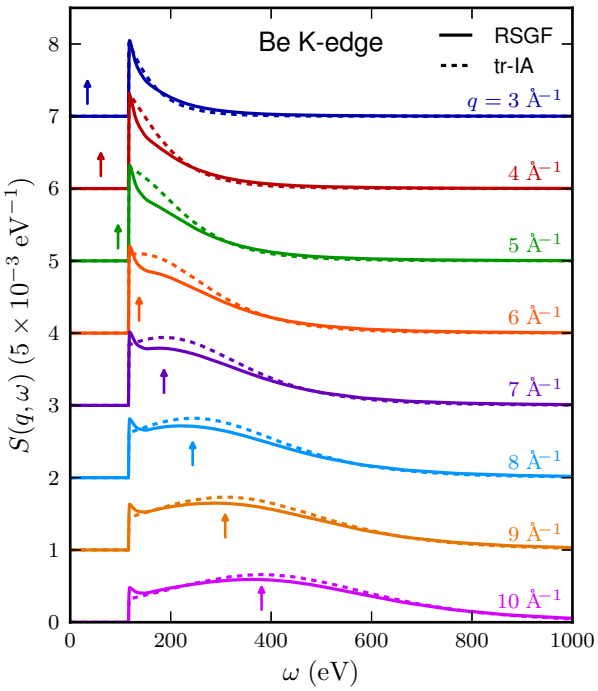

Figure 7.6: (Color online.) Comparison of theoretical core contribution to Be K-edge XRTS calculated using RSGF and truncated IA methods as a function of momentum transfer. Vertical arrows are located at the free-particle Compton shifts.

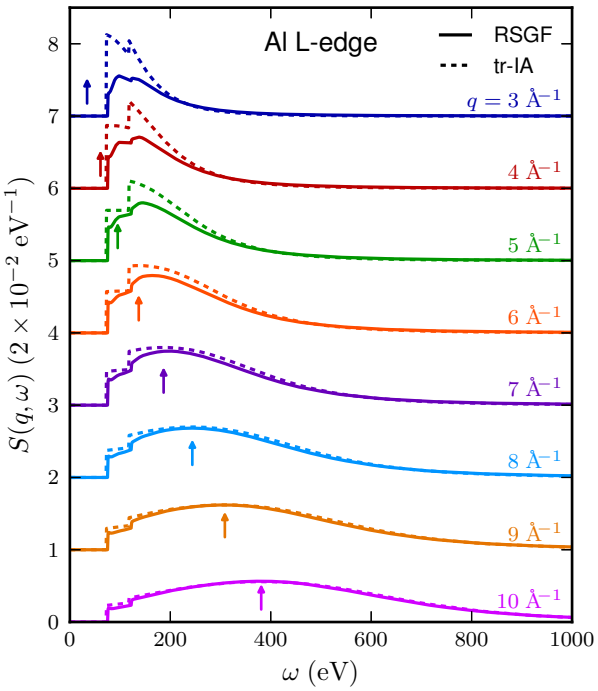

Figure 7.7: (Color online.) Same as Fig. 7.6, except for Al L_1- and $L_{2,3}$-edge XRTS.

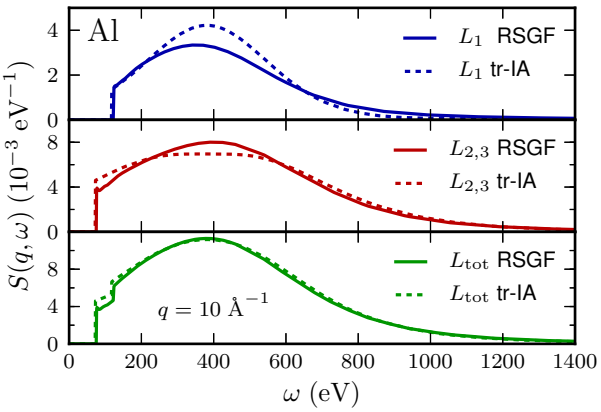

Figure 7.8: (Color online.) Comparison of RSGF and IA calculations for L_1 ($2s$) and $L_{2,3}$ ($2p$) subshells, along with the combined spectra at high q. While the RSGF and IA differ for individual subshells, agreement is recovered for the combined spectra.

Of the methods we have presented, the RSGF calculation most closely describes the ambient experimental data. Condensed-phase effects are included explicitly in final states. Although a frozen atomic core wavefunction is used, this is a common feature of all techniques under consideration, and should be sufficient at modest densities where core overlap is expected to be negligible. The primary limitation of the RSGF approach is that it is currently unclear how to incorporate continuum-lowering effects.

Alternatively, one can use an *ad hoc* modification of the low-energy-transfer tail of the IA

$$S_{\rm tr-IA}(q,\omega) = S(q,\omega)\left(1 - \frac{1}{e^{\beta(\omega - E_B)} + 1}\right). \tag{7.15}$$

We will refer to this approach, which for $T = 0$ simply truncates the spectrum below binding energy, as the *truncated IA* (tr-IA). This allows straightforward application of continuum-lowering models to adjust the binding energy. A similar approach, using screened hydrogenic wavefunctions for the initial state instead of Dirac-Fock is discussed in Gregori, et al.[114], but only in the context of smaller q, where the core contribution is relatively small. In Figs. 7.6, 7.7, and 7.8, we explore the accuracy and applicability of the tr-IA at T=0 by

comparing it with RSGF calculations for a range of momentum transfers for the K shell of Be and L shell of Al. Note that all calculations are in absolute units.

As long as the free-particle Compton shift (shown by vertical arrows) is a few times the edge energy, the tr-IA is in reasonable agreement with the RSGF calculation. Since the IA satisfies the f-sum rule by construction, the truncation of the low ω tail results in slight f-sum violations ($\lesssim 5\%$ for Al, $q \geq 6$ Å^{-1}). We also note that for the Al L shell, the tr-IA and RSGF calculations differ for the individual subshells (Fig. 7.8, upper two panels). However, agreement is recovered after combining to form the total L-shell contribution (Fig. 7.8 lower panel).

Recently, another approach to modeling XRTS from WDM has been discussed by Johnson, et al.[158] They use an *average-atom* model, which gives a significant improvement in the treatment of the free-electrons compared to a simple jellium model. Unfortunately, the average-atom binding energies disagree significantly with experiment, limiting the accuracy of the bound-free contribution to the XRTS spectrum. Johnson, et al.[158] also consider applying the PWFFA to the average-atom $1s$ state for Be and find similar qualitative discrepancies as we have discussed here.

In summary, for XRTS experiments with modest energy resolution at high momentum transfer it should be sufficient to treat the bound-free contribution with a truncated IA, where the truncation energy is adjusted to include the effects of continuum lowering. However, the IA ceases to be accurate at lower momentum transfers. If continuum-lowering shifts and temperatures are negligible compared to the desired energy resolution, then the RSGF approach can be immediately applied at any momentum transfer. Further investigation is needed to determine if continuum lowering can be calculated or included empirically within the RSGF framework.

7.5 Conclusion

We have discussed several techniques for calculating the core-shell contribution to XRTS and compared with experimental data collected from polycrystalline Be under ambient conditions. Of the techniques considered, the real-space Green's function method best describes the data. However, a simple *ad hoc* truncation of the impulse approximation is reasonably

accurate at higher momentum transfers and allows more straightforward inclusion of continuum lower effects. The accuracy of this truncated IA as a function of q has been explored by comparing with RSGF calculations for both the Be K-shell and Al L-shell. On the other hand, the plane-wave form-factor approximation, which has been used in the interpretation of several WDM experiments[240, 249, 243, 107, 174, 173, 96]is quantitatively and qualitatively inaccurate due to an inconsistent treatment of the single-particle Hamiltonian. Re-evaluation of the experimental data using a more accurate core calculation and maximum likelihood background subtraction is recommended. More importantly, an accurate treatment of the bound-free XRTS from WDM will be necessary when higher resolution experiments are performed at the Linac Coherent Light Source and the National Ignition Facility. We believe we have also motivated the need for cross-method comparisons and the usefulness of exchange of both theoretical and experimental techniques between the condensed-matter and dense-plasma communities.

Chapter 8

SYSTEMATIC ERRORS IN THE INTERPRETATION OF X-RAY THOMSON SCATTERING STUDIES OF WARM DENSE MATTER

Uncertainties in the equation of state (EOS) of ablator materials are one of the underlying challenges for complete modeling of inertial confinement fusion (ICF) experiments. X-ray Thomson Scattering (XRTS) studies of warm dense matter hold the potential to provide a critical test of EOS under conditions relevant to the early stages of compression, as demonstrated by recent experimental determinations of the adiabats in Be and CH. We discuss here a faulty theoretical treatment of inelastic x-ray scattering that has, for many years, been used when interpreting x-ray Thomson scattering studies of low-Z ablator materials. This practice has resulted in systematic errors of inferred temperatures, ionization states and free-electron densities that are likely at the level or larger than quoted systematic errors.

8.1 Introduction

A complete understanding of any laser-shock compression study requires careful treatment of the laser-plasma interaction, all mass and heat transport, and the equation of state (EOS) of the target material.[62] Any, or all, of these issues may play a role in the difficulty in obtaining ignition in the campaign for inertial confinement fusion (ICF) at the National Ignition Facility.[197, 120, 211] The thermodynamic path of the ablator material during the early stages of compression is notably problematic[96, 173, 107], as it encompasses high mass densities, structural disorder, incomplete ionization, and varying degrees of both free electron degeneracy and electron-ion scattering. The EOS[164, 46, 237], electronic structure[261, 161], and real-space structure[253, 217, 126, 220] in the often-called *warm dense matter* (WDM) regime is consequently a matter of considerable importance and current scientific interest.

However, from an experimental perspective, studies of WDM suffer from a substantial complication: the high opacity of the WDM up to at least the soft x-ray regime makes

it impossible to use passive observation of black-body radiation or laser scattering methods (as used at lower plasma densities) for the determination of state variables such as temperature.[107, 210] This has led to a long-standing research program to develop hard x-ray based diagnostics that actively probe the thermodynamic state variables in dense, partially ionized systems. [177, 107, 173, 96, 200, 185, 126, 299, 266, 256] Nonresonant inelastic x-ray scattering (IXS), typically called x-ray Thomson scattering (XRTS) in WDM studies, has emerged as the only broadly applicable method for studies of low-Z WDM at large-scale laser facilities.[107] As such, XRTS has the potential to strongly constrain the EOS of ablator materials, an accomplishment with deep importance in the campaign for ignition. For example, recent XRTS studies of shocked Be and CH show strong progress toward determining their adiabats in conditions relevant for the early stages of compression in ICF.[173, 96]

However, we have recently shown[193] that a theoretically unjustifiable model, the plane-wave form-factor approximation (PWFFA)[252], has been used for the bound-free contribution to the XRTS in many studies of WDM.[240, 249, 243, 181, 107, 174, 106, 173, 175, 96, 117, 190] The purpose of the present paper is to more completely revisit the implementation of theoretical models used for extraction of state variables from XRTS in laser-compression experiments and to assess the magnitude of errors that presently exist in the literature.

We have two main results. First, we find that the rejection of the impulse approximation (IA), a model well-known to be useful in the synchrotron x-ray studies,[251, 71] has been due to an inconsistent implementation of sum-rules between the free-electron and bound-electron contributions to the IXS. Second, we find that the near-universal acceptance of the PWFFA in laser-compression studies of WDM has resulted in previously unquantified systematic errors that can be significantly larger than reported statistical errors, with exact consequences that depend on experiment-specific kinematic conditions and on any assumptions or prior knowledge about instrumental backgrounds. As a subsidiary issue, we also propose that these results illustrate the importance of stronger communication and shared methodologies between the plasma-XRTS and synchrotron-IXS communities: high-resolution IXS data taken at ambient conditions should broadly serve as a testing ground for models to be used in WDM studies at large-scale laser facilities, where energy resolutions,

signal to noise, and knowledge of experimental backgrounds are typically much degraded.

8.2 Theory

Throughout this article, we will use Hartree atomic units ($\hbar = m_e = 1$) for theoretical expressions. The experimental observable in XRTS experiments is the double-differential scattering cross section, which in the first-Born approximation is given by[251, 71]

$$\frac{d^2\sigma}{d\omega_2 d\Omega} = \frac{\omega_1}{\omega_2}\left(\frac{d\sigma}{d\Omega}\right)_{\mathrm{Th}} S(\mathbf{k},\omega), \tag{8.1}$$

$$\left(\frac{d\sigma}{d\Omega}\right)_{\mathrm{Th}} = \left(\frac{\omega_2}{\omega_1}\right)^2 r_0^2 \left|\epsilon_1 \cdot \epsilon_2\right|^2, \tag{8.2}$$

$$S(\mathbf{k},\omega) = \sum_F \left|\langle F| \sum_j e^{i\mathbf{k}\cdot\mathbf{r}_j} |I\rangle\right|^2 \delta(E_F - E_I - \omega). \tag{8.3}$$

A clear separation exists between the probe-specific properties given by the Thomson scattering cross-section $(d\sigma/d\Omega)_{\mathrm{Th}}$ and material properties described the dynamic structure factor $S(\mathbf{k},\omega)$. In Eqs.(8.1)-(8.3), $\omega_{1,2}$ are the incident and scattered photon energies and $\epsilon_{1,2}$ are the respective polarizations. The energy and momentum transferred to the sample by the inelastic scattering event are given by ω and $\mathbf{k}$, $d\Omega$ is the differential solid angle into which the photon is scattered, and r_0 is the classical electron radius. $|I\rangle, |F\rangle$ are initial and final many-particle states with energies E_I, E_F, respectively, and the index j runs over all electrons. For finite temperatures, Eq. (8.3) should be thermally averaged over initial states.

Eq. 8.3 includes both coherent scattering, in which the final and initial states are identical, and incoherent scattering, in which they differ, i.e.,

$$S(\mathbf{k},\omega) = S^{\mathrm{COH}}(\mathbf{k})\delta(\omega) + S^{\mathrm{INC}}(\mathbf{k},\omega) \tag{8.4}$$

The small energy transfer associated with quasi-elastic scattering from the ion (e.g. phonons) does not influence the present discussion and their weight is included in $S^{COH}(\mathbf{k})$.

We now make use of the independent particle approximation and define a partial dynamic

structure factor

$$\begin{aligned} S_a(\mathbf{k},\omega) &= \sum_b \left| \langle b| e^{i\mathbf{k}\cdot\mathbf{r}} |a\rangle \right|^2 \delta(E_b - E_a - \omega) \\ &= |f_a(\mathbf{k})|^2 + S_a^{\mathrm{INC}}(\mathbf{k},\omega) \qquad (8.5) \\ f_a(\mathbf{k}) &= \langle a| e^{i\mathbf{k}\cdot\mathbf{r}} |a\rangle \qquad (8.6) \end{aligned}$$

where $|a\rangle$,$|b\rangle$ are initial and final *single-particle* states and E_a, E_b are the corresponding energies.

It is important to note that $S(\mathbf{k},\omega) \neq \sum_a S_a(\mathbf{k},\omega)$, but rather that,

$$\begin{aligned} S^{\mathrm{COH}}(\mathbf{k}) &= \left| \sum_a f_a(\mathbf{k}) \right|^2, \qquad (8.7) \\ S^{\mathrm{INC}}(\mathbf{k},\omega) &= \sum_a S_a^{\mathrm{INC}}(\mathbf{k},\omega). \qquad (8.8) \end{aligned}$$

As their names indicate, the coherent contributions add coherently, and the incoherent contributions add incoherently.

Now, $S_a(\mathbf{k},\omega)$ for a single electron satisfies the following sum rules [71, 151, 293]

$$\begin{aligned} \int_{-\infty}^{\infty} S_a(\mathbf{k},\omega)\, d\omega &= 1 \qquad (8.9) \\ \int_{-\infty}^{\infty} \omega\, S_a(\mathbf{k},\omega)\, d\omega &= \frac{k^2}{2}. \qquad (8.10) \end{aligned}$$

These generalize in the many-particle case to

$$\begin{aligned} \int_{-\infty}^{\infty} S^{\mathrm{INC}}(\mathbf{k},\omega)\, d\omega &= N - \sum_a |f_a(\mathbf{k})|^2 \qquad (8.11) \\ \int_{-\infty}^{\infty} \omega\, S(\mathbf{k},\omega)\, d\omega &= N\frac{k^2}{2}, \qquad (8.12) \end{aligned}$$

where N is the total number of electrons. We note that the sum in Eq. (8.11) is an incoherent sum, unlike that in Eq. (8.7). Eq. (8.12) is commonly referred to as the Bethe f-sum rule.[151]

These sum rules are useful for two primary purposes. The first is to normalize experimental data to absolute units for comparison with theory, where Eq. (8.12) is to be preferred over Eq. (8.11) because the former is independent of theoretical calculations of $f_a(\mathbf{k})$. We

note that the sum rules are valid for fixed **k**; errors of a few percent are made when normalizing energy-loss spectra taken at fixed scattering angle due to the slight ω dependence of k. However, this is typically well below the statistical noise of WDM data. The second purpose is as a check on any approximations made in theoretical calculations of the various contributions to $S(\mathbf{k},\omega)$.

8.3 Results and Discussion

In Fig. 8.1, we show high resolution synchrotron data from polycrystalline Be at ambient conditions from Ref. 194, to which we refer for experimental details. Since $S(\mathbf{k},\omega)$ from isotropic (e.g. polycrystalline) systems has no dependence on the direction of **k**, we will henceforth drop the vector symbol and refer simply to $S(k,\omega)$. We note that such high-resolution ($\sim$ 1 eV) IXS/XRTS measurements are regularly available at synchrotron light sources, where they are supported by dedicated endstation apparatus[85, 282, 265]. These facilities have been used to conduct numerous IXS/XRTS studies of condensed phase systems.[251, 88, 147, 32, 36, 34, 244, 81, 271, 91, 110, 13, 83, 78, 184, 294] The data in Fig. 8.1 have been placed into absolute units by applying a single overall scale factor in order to numerically satisfy the Bethe f-sum rule (Eq. (8.12)). A clear distinction can be seen between the contributions from the delocalized valence electrons and the bound core electrons. The valence electrons contribute a peak similar to an upside-down parabola that is centered at the free-particle Compton shift $\omega_C = k^2/2$. The core contribution displays a sharp onset at the $1s$ binding energy $E_B = 112$ eV, and is subsequently much broader. The small oscillatory structure in the core contribution near $\omega = E_B$ is due to solid-state interference effects in the final photo-electron state[263], and will not be considered further here.

The extraction of thermodynamic parameters from XRTS spectra at elevated temperatures in the WDM regime is strongly dependent on the relative magnitudes of the valence (called free-free) and core (called bound-free) contributions to the IXS. For given experimental conditions, it is the ratio of f-sums of the theoretical forms fitted to these two contributions that, for example, substantially determines the ionization state of the core levels. The degree of ionization in turn then constrains the inference of temperature or

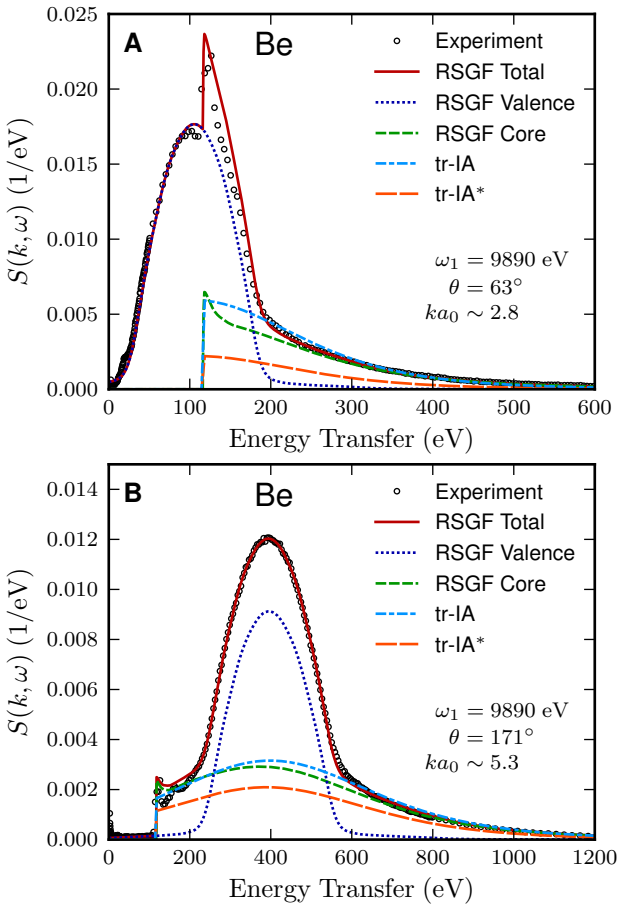

Figure 8.1: High-resolution NIXS data from polycrystalline Be at ambient conditions, normalized to absolute units using the Bethe f-sum rule. A real-space Green's function (RSGF) calculation agrees well with the experimental data at both momentum transfers shown. A truncated impulse approximation (tr-IA) makes modest errors at both momentum transfers. The additional scaling present in the tr-IA*, however, significantly underestimates the core contribution relative to the valence.

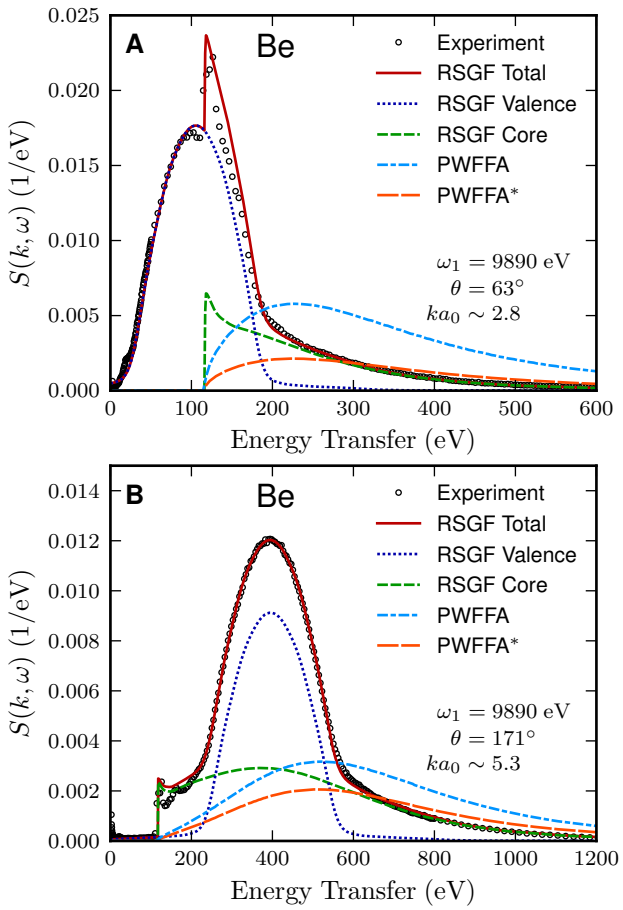

Figure 8.2: Comparison between experiment and plane-wave form-factor approximation. Although the PWFFA dramatically differs from the experimental data, near-agreement on the high-ω tail is fortuitously regained after including the scaling present in the PWFFA*. However, the low-ω region is significantly underestimated by the PWFFA*.

free-electron density. We now use the data in Fig. 8.1 as a contextual testing ground for illustrating and evaluating the differing theoretical practice for IXS that presently exist between the synchrotron IXS and laser-plasma XRTS communities.

We first compare the experimental data to a real-space Green's function calculation, shown in Fig. 8.1. We refer elsewhere for details of these calculations[193]. We note that the RSGF calculations are preformed in absolute units, contain no free parameters, and numerically satisfy the sum rules, Eqs. (8.11),(8.12), to within a few percent. Good agreement with the data is seen throughout.

The `XRTS` software package[115, 114, 107] has been used for the analysis of nearly all XRTS studies from WDM.[240, 249, 243, 181, 107, 174, 106, 173, 175, 96, 117, 190] The starting point[114] is again the independent particle approximation, now in a form following Chihara[42]

$$S(k,\omega) = |f_I(k) + q(k)|^2 S_{\rm ii}(k,\omega) + S_{\rm ff}(k,\omega) + S_{\rm bf}(k,\omega). \tag{8.13}$$

The first term accounts for quasi-elastic scattering off of electrons that follow the ion motion, including bound electrons with form-factor $f_I(k)$ and the screening cloud of free (and valence) electrons with form-factor $q(k)$. $S_{\rm ii}(k,\omega)$ is the ion-ion correlation function. The second term in Eq. (8.13) gives the contribution from free electrons and the final term gives the contribution from bound electrons scattered into the continuum. These are the free-free and bound-free contributions, respectively.

For the incoherent contribution to the scattered x-ray intensity, in the methodology used in WDM studies,[107, 115, 114] one then defines

$$I_{\rm INC} = A \left(\frac{\omega_2}{\omega_1}\right)^2 \left[B^{-3}\, r_k\, \tilde{S}_{\rm bf}(k,\omega) + S_{\rm ff}(k,\omega)\right], \tag{8.14}$$

where A is an overall scale factor fit to experimental data. $\tilde{S}_{\rm bf}(k,\omega)$ is a high-k model for the bound-free scattering, e.g., in the impulse approximation. The factor r_k is intended to correct for errors made due to this pragmatic choice. Whether this correction is valid is a subtle point, which we will discuss in detail later after giving more context.

First, however, we discuss the Breit-Dirac recoil factor[37, 58, 154]

$$B^{-3} \equiv \left(1 + \frac{k^2/2}{\omega_1}\right)^{-3}, \tag{8.15}$$

It is surprising that this factor is associated with the material properties of the bound electrons alone in Eq. (8.14) instead of the overall Thomson-scattering cross-section which encapsulates the probe-specific physics in the first-Born approximation. In x-ray diffraction studies, the total incoherent intensity is often The standard form of this correction contains $B = (\omega_2/\omega_1)$, which agrees with Eq. (8.15) only at the free-particle Compton shift. In standard discussions of this correction[75, 166, 154], one factor of B is typically meant to account for energy-sensitive detectors. This is already present in Eq. (8.14) as the additional power of (ω_2/ω_1) compared to Eq. (8.1). The other two factors of B constitute the well-known difference between the quantum and classical Thomson scattering cross-sections.[153] These are included in Eq. (8.2) and thus have already been accounted for in Eqs. (8.1) and (8.14). Fortunately, although the factor of B^{-3} should not be present in Eq. (8.14), the error it introduces is typically small; for the conditions shown in Fig. 8.1, the RHS of Eq. (8.15) is ~ 0.97 for the upper panel and 0.90 for the lower panel and is constant to $\sim 1\%$.

Now, two primary models are used for calculating $\tilde{S}_{\rm bf}(k,\omega)$ in WDM studies: a truncated impulse approximation (tr-IA) and the plane-wave form-factor approximation (PWFFA) of Schumacher[252]. In the tr-IA, the spectrum is first calculated in the impulse approximation (IA)[71], and then truncated to zero for $\omega < E_B$. We have recently shown that the PWFFA is an uncontrolled approximation which is internally inconsistent and violates energy conservation.[193] For a thorough discussion of these two models, we refer to Ref. 193.

In both the (untruncated) IA and the PWFFA, the left-hand side of Eq. (8.11) is always equal to the number of bound electrons N_b, with no allowance for non-zero $|f_a(k)|^2$. The factor of $r_k \equiv 1 - \sum_a |f_a(k)|^2/N_b$ in Eq. (8.14) is then motivated by the desire to bring these models into agreement with Eq. (8.11). However, in the case of the tr-IA, this is flawed for several reasons. First, the truncation present in the tr-IA itself decreases the left-hand side of Eq. (8.11). We have found numerically that the truncation alone results in near-satisfaction of Eq. (8.11), with the residual discrepancy being $\lesssim 20\%$ for all k, as we show later. Second, since the truncation only affects low (or negative) ω, the Bethe f-sum rule, which is satisfied exactly for the IA, is only modestly violated ($\lesssim 10\%$) by the tr-IA.[193] Thus, scaling the tr-IA by r_k results in substantial violation of both of the sum rules. Third, we have found that the tr-IA is reasonably accurate along the high-ω tail for

$k^2/2 \gtrsim E_B$[193]. Consequently, any rescaling factor applied to the tr-IA over the entire energy loss spectrum will necessarily result in departures from the physical solution for the high-ω tail of the bound-free contribution, i.e., exactly the data that strongly influence the inferred ionization state of the core level. In the remainder of the paper, we illustrate these facts and analyze the consequences of this conceptual error, and the closely related adoption of the PWFFA, in the analysis of XRTS WDM studies.

Throughout the following discussion, we will use the notation tr-IA* and PWFFA* to refer to the scaled combination $B^{-3}\, r_k\, \tilde{S}_{\rm bf}(k,\omega)$ (see Eq. (8.14)). In Fig. 8.1, we show tr-IA and tr-IA* calculations using a hydrogenic $1s$ wavefunction with a screened nuclear charge $\tilde{Z} = 3.81$[216]. The value of r_k in the tr-IA* was calculated for the same hydrogenic wavefunction. From Fig. 8.1, it is clear that the *unscaled* tr-IA shows, as expected, good agreement with the experimental data and RSGF calculations at both momentum transfers shown. However, the scaled tr-IA* significantly underestimates the core contribution relative to the valence. Again, when the rescaling of Eq. (8.14) is used, the sum rules (Eqs. (8.11) and (8.12)) are not being consistently applied between the free-free and bound-free contributions.

In Fig. 8.2, we reproduce Fig. 8.1, but replace the tr-IA core by calculations using the PWFFA and PWFFA*. The unscaled PWFFA shows dramatic disagreement with experiment, as we have previously noted.[193] The factor of r_k in the PWFFA* then has its intended effect of rescaling such that Eq. (8.11) is satisfied. This results, somewhat fortuitously, in much improved agreement along the high-ω tail (although, at the expense of significantly underestimating the region near the binding energy). For this reason, the PWFFA* has been preferred over the tr-IA* in the vast majority of XRTS studies of WDM[240, 249, 243, 181, 107, 174, 106, 173, 175, 96, 117, 190]. However, the fact that the PWFFA* gives reasonable fits to experimental data provides no support for this methodology. Instead, it emphasizes that low-resolution XRTS data typically has relatively low information content and cannot generally be expected, by itself, to select between different theoretical treatments of the electronic structure of WDM.

In order to determine the magnitude of systematic errors made by the use of the PWFFA* in XRTS studies, we consider two representative cases. In Fig. 8.3, we simulate incoherent scattering spectra using a core contribution calculated from the RSGF[263] combined with

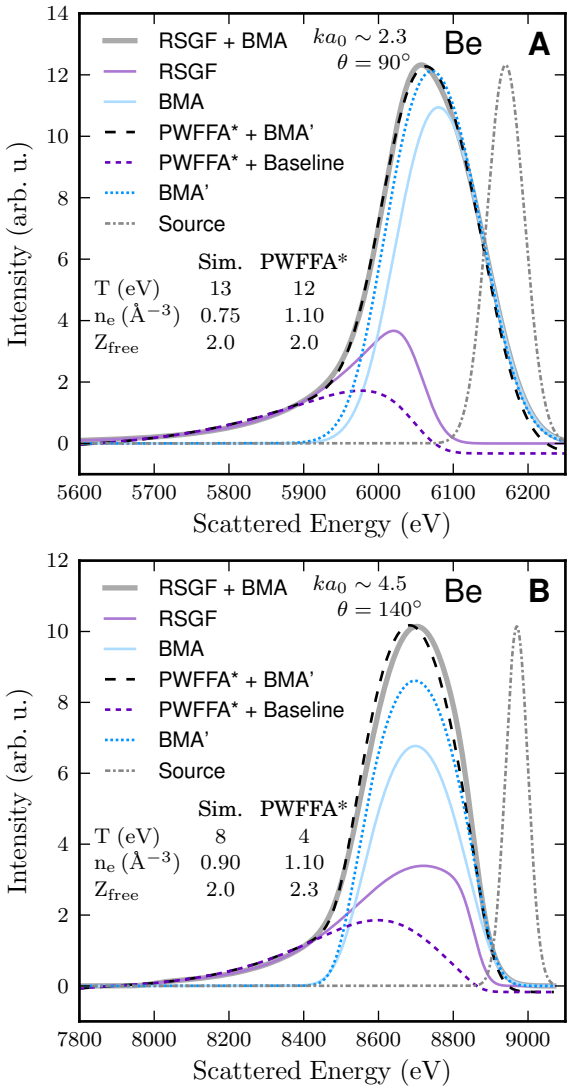

Figure 8.3: Estimation of characteristic systematic errors when using the PWFFA* in the thermodynamic and kinematical conditions of (A) Lee, et al[181] (90° data) and (B) Fortmann, et al.[96] (pre-shock-collision). Simulated IXS is generated by combining a real-space Green's function core (RSGF) with a valence calculation in the Born-Mermin approximation and broadening to match the combined experimental resolution (Source). The simulated curves are then fit using a PWFFA* core and a BMA valence with adjustable density n_e, temperature T and ionization state Z_{free}. Additionally, a constant baseline and overall amplitude are fit to emulate the presence of an unknown background and uncertain experimental normalization.

a valence contribution in the Born-Mermin approximation (BMA)[255] under the conditions of Lee, et al.[181] (Fig 8.3A) and Fortmann, et al.[96] (Fig. 8.3B). The incident energies and scattering angles were chosen to match the experimental studies, and all curves have been Gaussian broadened (60-eV FWHM for panel A and 70-eV for panel B, labeled "Source") to agree with the net experimental resolution of these studies. The simulated curves were then fit using a PWFFA* core and a BMA valence contribution (labeled BMA' in Fig. 8.3) parameterized by electron density, temperature and ionization state. Additionally, a constant baseline and overall amplitude were included in the fit, as is standard practice due to uncertainties in background levels and normalization of experimental data. The curves in Fig. 8.3 are plotted with respect to scattered energy instead of energy transfer, as is typical in the XRTS literature.

For the lower incident energy and k of Fig. 8.3A, the valence electron response is partially collective, as can be seen by the density-dependence of the valence peak location. The PWFFA* core peaks at lower energies than the RSGF core, which is compensated for in the fit by increasing the density by $\sim 45\%$. We also note that a negative baseline was required to obtain agreement along the low-energy tail. To summarize: using a correct theoretical treatment for the core, we have made simulated spectra at the reported thermodynamic conditions of reference 181. We find that fits based on the PWFFA* (Eq. (8.14)) then lead to deviations (9% for T and 47% for n_e) at the scale of the reported statistical errors (23% for T and 6% for n_e).

At the higher incident energy and k of Fig. 8.3B, the valence electron peak location is no longer density dependent, but instead is located near the free-electron Compton shift. The scattering in this regime is entirely non-collective. Here the lack of weight in the PWFFA* near the binding energy is compensated for by increasing the ionization state by 15%. Increasing ionization state alone results in a overly-broad peak, which is further corrected for by an underestimation of temperature by $\sim 50\%$. However, this result is highly influenced by the strong covariance present between temperature and density, which must be broken by accurate modeling of the coherent scattering contribution. We note that the peak shift in the core cannot be completely compensated for by adjusting any of the free parameters we have allowed. To summarize: using a correct theoretical treatment for the

	$k = 2.3$			$k = 4.5$		
	Sim.	PWFFA*	tr-IA	Sim.	PWFFA*	tr-IA
T (eV)	13	12	12	8	4	7
n_e (Å^{-3})	0.75	1.10	0.7	0.90	1.10	0.90
Z_{free}	2.0	2.0	2.0	2.0	2.3	2.0

Table 8.1: Effect of different models for the core contribution on fits to simulated data.

core, we have simulated spectra at the reported thermodynamic conditions of reference 96. We find that fits based on the PWFFA* lead to deviations (50% for T and 22% for n_e) that are at the scale of reported statistical errors (22% for T and 8% for n_e).

We have also performed fits to the simulated spectra using the unscaled tr-IA for the core. These results, and those of the fits shown in Fig. 8.3, are shown in Table 8.1. Compared to the PWFFA*, the tr-IA fits come much closer to reproducing the simulated parameters although small discrepancies remain. We note that in these and similar experimental conditions, the best-fit parameters will also be dependent on the accuracy of the estimated binding energy, including any continuum lowering effects.[44]

In Table 8.2 we show the result of numerically evaluating the sum rules for the contribution to $S(k, \omega)$ (for fixed k) from a single $1s$ electron in Be using the various theoretical treatments we have discussed. The RSGF values agree with the exact values to within a few percent. The unscaled tr-IA satisfies the f-sum rule to a similar accuracy, but slightly overestimates the total integral. The scaled tr-IA* and unscaled PWFFA both significantly violate both sum rules. Finally, the scaled PWFFA* is close to having the correct total integral, but violates the f-sum rule by $30 - 50\%$.

8.4 Conclusion

We have shown that an inconsistent normalization between the bound-free and free-free contributions to x-ray Thomson scattering has been used in the analysis of many diagnostic studies of WDM[240, 249, 243, 181, 107, 174, 106, 173, 175, 96, 117, 190]. This has resulted in the adoption of a theoretically unjustifiable model for the bound-free contribution which

	ka_0	Exact	RSGF	tr-IA	tr-IA*	PWFFA	PWFFA*
$\langle\omega^0\rangle$	2.3	0.32	0.31	0.36	0.10	0.99	0.28
	4.5	0.73	0.72	0.76	0.49	0.99	0.63
$\frac{2}{k^2}\langle\omega^1\rangle$	2.3	1.00	1.02	1.02	0.29	5.11	1.45
	4.5	1.00	1.03	1.05	0.67	2.06	1.31

Table 8.2: Numerical evaluation of sum rules, Eqs. (8.11) and (8.12), for the contribution to $S(k,\omega)$ from a single $1s$ electron in Be at fixed k. For the exact value of $\langle\omega^0\rangle$, the RHS of Eq. (8.11) was evaluated for a Hartree-Fock $1s$ orbital.

has led to previously unidentified systematic errors. We find that these systematic errors are likely at, or above, the reported level of statistical uncertainty in many of these studies. Both a reanalysis of prior work and a modification of ongoing data analysis methods are needed.

Chapter 9

CONCLUSIONS AND FUTURE DIRECTIONS

In this dissertation, I have developed a method for theoretical calculation of the valence-electron contribution to non-resonant inelastic x-ray scattering spectra from materials in the warm dense matter regime. In doing so, I have shown the importance of including the non-perturbative effects of the ion-electron interaction on the valence-electronic state. I have also discussed the relative strengths of a variety of models for the core-shell contribution.

I have shown that the prevailing models used in the analysis of non-resonant inelastic x-ray scattering studies of warm dense matter introduce systematic errors into extracted thermodynamic state parameters that are likely at the level of current statistical accuracy or larger. These errors are due to a common misconception, namely that the valence electron wavefunctions in dense systems can be accurately treated as being simply plane waves. Such an approximation neglects the non-perturbative effects of the potential landscape in which the valence electrons live. In particular, the lack of orthogonalization between valence electrons and occupied core states results in a significant underestimation of the breadth of the valence-electron momentum distribution and thus the width of the Compton scattering contribution to the NIXS spectrum. This leads to underestimation of electron density, temperature or both parameters in fits to experimental NIXS data from WDM. For the core-shell contribution to NIXS, the use of plane-wave final states results in a shift of the peak to higher energy transfer, with the offset being equal to the binding energy of the core state. The effect that this has on extracted thermodynamic parameters depends on both the kinematics of the experiment (which sets the Compton shift, and thus the location of the core-shell contribution with respect to that from the valence). However, in any case, this results in a reshaping of the portion of the spectrum to be fit by the valence-electron model, and thus a modification of extracted thermodynamic parameters.

The logical next step for this work is to include ionic disorder by averaging over con-

figurations obtained from molecular dynamics simulations of hot-dense Be. Currently, for a single configuration at fixed thermodynamic state, the `FEFF` calculation requires ~ 200 hours of CPU time. This time scales linearly with the number of configuration and points in thermodynamic phase space required. Thus, a study including disorder could be performed on a modest computational cluster. However, the computational time required to perform perform a full unconstrained fit to experimental data is still somewhat prohibitive. Before such an effort is to be deemed worthwhile, critical tests of each component of the spectrum are needed.

At present, the low resolution of experimental data, which is insufficient to even distinguish between the core- and valence contributions to the spectrum, makes such tests difficult, since data can be fit well using a variety of models. Fortunately, higher energy resolution will be attainable in studies at x-ray free electron facilities such as the Linac Coherent Light Source (LCLS) at Stanford and the upcoming European X-ray Free Electron Laser (XFEL) in Hamburg, both of which have plans for beamlines focused on studying matter at elevated temperatures and densities. As data from these facilities becomes available, the separation between the valence and core-shell contributions to the spectrum should be much more clear, providing an additional strong constraint on fitting parameters and thus give a much better test of theoretical models used for each of the contributions to the spectrum.

Appendix A

A PLASTIC MINIATURE X-RAY EMISSION SPECTROMETER (MINIXES) BASED ON THE CYLINDRICAL VON HAMOS GEOMETRY

(*Originally published as:* B. A. Mattern, G. T. Seidler, M. Haave, J. I. Pacold, R. A. Gordon, J. Planillo, J. Quintana, and B. Rusthoven, Rev. Sci. Inst. **83**, 023901 (2012))

We present a short working distance miniature x-ray emission spectrometer (miniXES) based on the cylindrical von Hamos geometry. We describe the general design principles for the spectrometer and detail a specific implementation that covers $K\beta$ and valence level emission from Fe. Large spatial and angular access to the sample region provides compatibility with environmental chambers, microprobe and pump/probe measurements. The primary spectrometer structure and optic is plastic, printed using a 3-dimensional rapid-prototype machine. The spectrometer is inexpensive to construct and is portable; it can be quickly set up at any focused beamline with a tunable narrow bandwidth monochromator. The sample clearance is over 27 mm, providing compatibility with a variety of environment chambers. An overview is also given of the calibration and data processing procedures, which are implemented by a multiplatform user-friendly software package. Finally, representative measurements are presented. Background levels are below the level of the $K\beta_{2,5}$ valence emission, the weakest diagram line in the system, and photometric analysis of count rates finds that the instrument is performing at the theoretical limit.

A.1 Introduction

Several different types of dispersive optics are used in x-ray spectrometers for laboratory and light-source based experiments. The Johann[156], Johannson[69, 157], and von Hamos[289] geometries are the most commonly used, and considerable effort has been made to steadily improve the quality of such optics and the diversity of their application [260, 145, 140, 4, 125, 128, 129, 130, 131, 206, 239, 258, 259, 222, 295, 296, 86]. In practice, instruments

based on spherically-bent crystal analyzers (SBCA) using the Johann geometry are the most commonly employed, with several instruments based on one or more SBCA present at most hard x-ray light sources[22, 226, 165, 132]. While some of the dominance of SBCA-based instruments is historical in nature and some is due to synergistic benefits of using SBCA for $\sim$ 1-eV resolution at facilities where SBCA have also been developed for much higher energy resolution applications, it is important to recognize that the SBCA-based instruments hold a unique advantage in flexibility of operation. First, when used in traditional, focusing mode, they efficiently select a single emission energy and consequently are ideal for high-energy resolution fluorescence detection (HERFD), a technique with rapidly growing appeal in the synchrotron community. [54, 100, 55, 101, 189, 28] Second, when operated in positions off the Rowland circle, as has been common for some years in plasma physics[94, 279, 196] but is a more recent development in synchrotron radiation studies,[140, 283, 2, 148] the SBCA then support dispersive-mode operation, distributing their collection solid angle across a range of emission energies.

That being said, when one excludes the case of HERFD applications from dilute species, spectrometers based on purely dispersive analyzer optics are often at least technically competitive with multi-SBCA systems and sometimes have operational characteristics that are highly favorable to net scientific output.[137, 275, 139, 138] One of the most recent examples of such an alternative route to $\sim$1-eV resolution hard x-ray spectroscopy comes in the demonstration of a very efficient, short working-distance (SWD) x-ray spectrometer by Dickinson, et al.[57] As demonstrated in the present paper, these instruments are inexpensive, easily fabricated and operated, and (perhaps most importantly from the standpoint of fostering novel science) are trivially portable and can be readily implemented at any high-flux, hard x-ray beamline. As such, they provide an important new route to implement $\sim$ 1-eV resolution resonant and non-resonant x-ray emission spectroscopy.

SWD optics are based on the observation that microfocused incident beams permit one to obtain good energy resolution from an analyzer crystal which is $\sim$1 cm from the sample, as opposed to the $\sim$1-m distance which is more typical when using spherically bent crystal analyzers (SBCA). In Dickinson, *et al.*[57], a collection of small, flat analyzer crystals were arranged near the sample on a fixed support in a Johann-like configuration. The reflections

from the analyzer crystals were spatially filtered so that each crystal uniquely illuminates a different region on a 2-dimensional position-sensitive detector (2D-PSD) having very low dark-counts and readout noise. After *in situ* calibration of each pixel of the 2D-PSD, the resulting instrument demonstrated performance comparable to traditional inelastic x-ray scattering or x-ray emission spectrometers for some applications. The low cost and straightforward operation of even the prototype instrument suggest a useful range of future applications of SWD optics in x-ray emission spectroscopy and inelastic x-ray scattering experiments. In particular, for concentrated samples SWD spectrometers should provide single-shot collection of hard x-ray emission spectra at the Linac Coherent Light Source.

Our research group has since pushed forward to develop several variants of SWD spectrometers[213, 109]. This approach has come to be known in the synchrotron community as "miniXES" (miniature X-ray Emission Spectrometer). In this paper, we present a spectrometer covering the Fe $K\beta$ and valence emission regions using an SWD design based on the von Hamos geometry. Fe compounds are ubiquitous across many areas of active research, including high pressure studies of magnetism[10, 9, 11, 186, 187], non-precious metal fuel-cell catalysts[159], metalloenzymes[221] and other metallo-organics[280], thus motivating this choice of energy range.

As noted previously[57], the Johann geometry for SWD optics often presents a significant challenge to the experimenter to find a analyzer crystal with a Bragg reflection quite close to backscatter for the desired energy range. The Johann geometry does not satisfy the Rowland circle, and the associated Johann aberrations, which are small for longer working-distance instruments (such as SBCA), become extreme for the large collection angles used in the SWD approach when the reflection from the analyzer crystal is not close to backscatter. In the von Hamos geometry, however, each analyzer crystal approximately satisfies its own Rowland circle. This allows the use of a Bragg reflection further from backscatter, increasing the space available for the sample, removing the sample from the path between analyzer and detector and allowing compatibility with a range of sample environments such as cryostats, furnaces, diamond anvil cells (DACs) and electrochemical cells. This geometry also spatially separates the sample-to-analyzer and analyzer-detector pathways allowing for improved shielding.

The remainder of this paper is arranged as follows. In section A.2 we describe the design

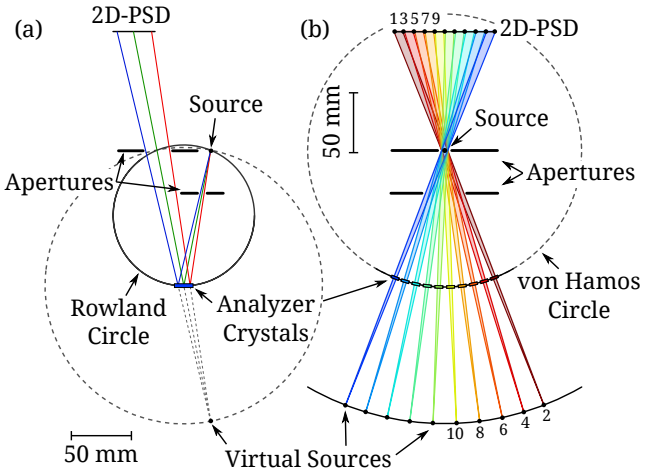

Figure A.1: (Color online). (a) Side view of ray tracing for a single analyzer crystal. (b) Front view. Ray tracing from real source to analyzer crystals has been left off for clarity. Note that only ∼30% of each analyzer crystal is active.

and construction of the spectrometer and the experimental configuration. A key point in the design process is the use of in-context computer-aided design (CAD) in the SolidWorks environment and the embedding of the geometric constraints associated with optimal design of the SWD optic into the CAD assembly documents. Although the spectrometer could have been machined using traditional means, it was convenient and less expensive to have major components fabricated as all-plastic parts using a 3-dimensional rapid prototyping machine (i.e., "3D printer"). This combination of CAD-embedded geometrical constraints and rapid prototyping greatly eases modification of the design to cover a wide range of a different emission lines. As discussed in this section, table A.1 contains a list of suitable analyzer crystals and Bragg angles for $3d$ transition metal Kβ emission lines. The current spectrometer design can be easily modified to produce spectrometers for any of these emission lines. In section A.3 we describe the spectrometer operation, calibration and data processing procedures. We have written a cross-platform Python software package to streamline data processing for this and other similar spectrometers. This package includes a user-friendly calibration interface and several command-line processing utilities

allowing most data processing to occur at the beamline, including batch processing of large data sets. In section A.3 we also present sample data taken with the instrument and give a photometric analysis demonstrating that our instrument is performing at the theoretical limit. Finally, in section A.4 we conclude.

A.2 Experimental

A.2.1 Spectrometer Design

The spectrometer design is a variation of the classical von Hamos optic[289], replacing the single cylindrically bent crystal with flat crystals that tile the cylindrical surface (see Fig. A.1). Although this modification results in a loss of focus along the cylindrical axis, a quasi-focus is retained at which an exit aperture is placed. Following Dickinson, *et. al.*[57], this exit aperture allows the dispersed image from each analyzer crystal to illuminate a unique region of the detector.

The geometry of the spectrometer is primarily constrained by the desired energy range, resolution and the size of the active region of the 2D-PSD. The Fe $K\beta$ emission region, including the valence emission band ($K\beta_{2,5}$), extends from ∼7000 to 7140 eV, including some extra range on both sides for background characterization. After selecting the desired energy range, an appropriate analyzer crystal material and orientation are chosen so that this energy range has Bragg angles close enough to backscatter to obtain the desired energy resolution at a short working distance, but not so close as to negatively impact sample clearance. For the energy range above, Ge (620) crystals give Bragg angles between 76° and 82°. This spectrometer is based around a commercial 2D-PSD, the Dectris Pilatus 100K. The detector face is 83.8×33.5 mm^2 with 487×195 pixels of dimension 172×172 μm^2. For spectrometers coupled to this detector, the von Hamos geometry is optimal when the range of Bragg angles of interest is greater than $\sim 3°$, as in the current case. For smaller angular ranges, an alternative design based on the Johannson geometry[213] will typically provide a larger collection solid angle.

For a microfocused beam, the energy resolution of the spectrometer is primarily determined by the angular size of a detector pixel as seen from a virtual source, and thus, for

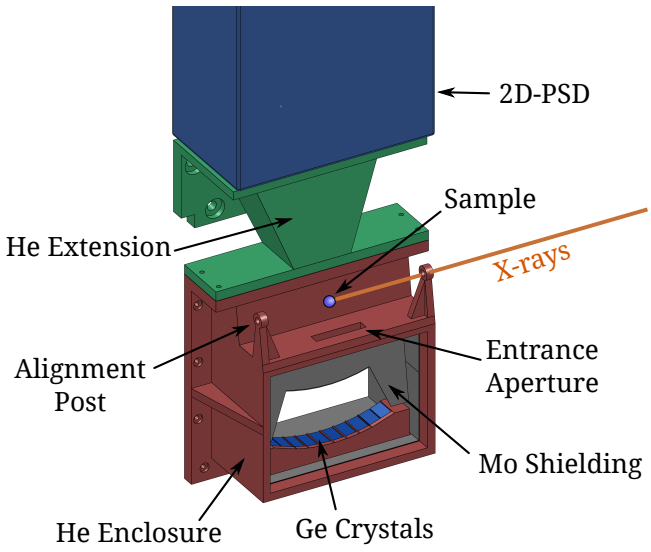

Figure A.2: (Color online). A 3D cutaway rendering of the spectrometer.

fixed linear pixel size, by the total path length from source to detector. Moving the detector further back gives a linear increase in resolution. However, since the total area of the detector is also fixed, this results in quadratic loss of total collection solid angle. Thus, it is optimal to place the detector as close as possible while still resolving the spectral features of interest. For nonresonant core-shell spectroscopies, the lifetime broadening of spectral features is dominated by the core-hole lifetime[100], e.g., 1.25 eV for the Fe 1s shell[98]. In the case of resonant x-ray emission spectroscopy, on the other hand, resonant-Raman features are broadened primarily by the final-state lifetime[100]. For the Fe 3p shell, the lifetime broadening is multiplet-term dependent due to the spin dependence of super-Coster-Kronig decay rates[288, 276], but is not lower than ∼0.6 eV[98, 276]. For the present instrument, in order to balance collection solid angle and spectrometer resolution, we chose an average pixel energy width of 0.7 eV. Placing the detector appropriately to obtain this resolution, i.e., a typical distance from source to detector of 33.8 cm, results in a total active collection solid angle of 20 msr. This solid angle is calculated as the sum of solid angles subtended by each illuminated detector pixel as seen from the virtual source of the corresponding analyzer crystal, and thus includes the effects of all entrance and exit apertures.

For comparison with other spectrometers, we note that a standard 10-cm diameter spherically bent crystal analyzer (SBCA) at 1-m working distance from a sample covers a solid angle of 7.9 msr; the active collection solid angle of this spectrometer is thus equivalent to that of 2.5 traditional SBCA.

Next, the radius of the Rowland circle (Fig. A.1a) is chosen to give a roughly even three-way split between source-to-crystal, crystal-to-aperture and aperture-to-PSD distances. This provides a good balance between collection solid angle, obliqueness of incidence on the detector face and sample clearance. At this point the geometry for a single analyzer crystal (Fig. A.1a) is fully constrained.

This geometry then must be duplicated and rotated about the line connecting the source to the exit aperture. For a given rotation angle, the exit aperture size and detector location would need to be chosen appropriately in order to optimally fill the detector with non-overlapping images. Since we have already constrained the detector location, we instead fix the non-dispersive exit aperture size and use the following iterative solution to the inverse problem of determining the crystal locations required to optimally fill the detector.

Beginning at one edge of the 2D-PSD, (point 1 in Fig. A.1b), raytrace through the closest edge of the aperture to the circle of virtual sources (point 2), and back to the 2D-PSD (point 3). The intersection of this triangle with the von Hamos circle defines the active region for one crystal. After moving over a few pixels on the detector face to prevent overlap of dispersed images, repeat the process until the entire 2D-PSD is filled. For the present spectrometer, this procedure results in 10 analyzer crystals with central scattering angles from 69.3° to 110.7°, separated by $\sim 4.6°$. This corresponds to momentum transfers between 4 and 6 Å^{-1} for 7100 eV elastically scattered radiation.

Decreasing the non-dispersive dimension of the exit aperture results in a larger number of narrower crystals needed to fill the detector. This has the benefit of limiting the pathways by which non-specular scatter off of the analyzer crystals can reach the camera, thus reducing background. In the limit of an infinitely thin aperture, one recovers the original focusing von Hamos bent crystal. However, for flat crystals, decreased size requires higher machining precision to gain the same angular tolerance. This places a practical lower limit on the crystal size and thus also on the aperture size. Since the condition of non-overlapping

images results in gaps between the active analyzer regions, the crystals can be oversized to fill in these gaps, improving angular precision. It is beneficial to include individual entrance apertures, one for each analyzer crystal, to ensure that only the active region is exposed. This removes background from non-specular scattering (e.g., Compton scattering) from the non-active crystal regions, and also helps remove scatter or fluorescence from exposed plastic between the crystals.

This design can be easily modified to produce spectrometers covering many interesting emission bands of other elements, e.g., the Kβ emission from other $3d$ transition metals. Table A.1 lists selected Bragg angles for a few analyzer crystal materials and shows that suitable refelections exist for all of the $3d$ transition metals. The relatively large acceptance angle of the miniXES design opens up the undesired possibility of the Bragg condition being satisfied for other planes in the analyzer that are close in angle to the desired one. This possibility is greatly reduced by using high-symmetry analyzer materials due to the selection rules for Bragg scattering. For this reason, we have only considered Ge, Si and GaP in table A.1.

A.2.2 Construction

The spectrometer body is constructed out of two pieces of plastic that were fabricated using an Alaris 30 rapid-prototyping machine. One piece (labeled "He Enclosure" in Fig. A.2) forms the optic on which the Ge crystals are mounted, the helium enclosure and posts for alignment with the x-ray beam. Access to the spectrometer interior is provided through a lucite door that seals over an O-ring. A second plastic piece ("He Extension" in Fig. A.2) extends the helium space from the exit aperture up to the detector. Polyimide film is used to form entrance and exit windows that seal the helium space.

The interior of the He enclosure is lined with 0.25-mm thick Mo shielding in order to prevent stray x-ray transmission through the plastic and fluorescence from the small metal content in the plastic from reaching the detector. The Mo plates are shaped by wire-electric discharge machining. The entrance and exit apertures are also cut into the Mo shielding. A vertical Mo shield is placed between the source-to-crystal and crystal-to-detector paths

Element	$E_{1,3}$	$E_{2,5}$	Crystal	Reflection	$\theta(E_{1,3})$	$\theta(E_{2,5})$	$\theta(E_{1,3}+20)$	$\theta(E_{1,3}-45)$	$\theta(E_{2,5}+20)$
Sc	4460	4495	Ge	(400)	79.32	77.18	78.04	83.06	76.11
Ti	4931	4971	Ge	(331)	75.58	73.91	74.70	77.80	73.13
V	5427	5471	Ge	(422)	81.54	78.87	80.22	85.85	77.85
Cr	5946	5989	Ge	(333),(511)	73.23	71.94	72.60	74.74	71.36
Mn	6490	6544	Ge	(440)	72.75	71.29	72.19	74.09	70.78
			GaP	(440)	82.37	79.41	81.15	86.43	78.52
Fe	7058	7117	Ge	(620)	79.08	76.82	78.27	81.18	76.15
			GaP	(600)	75.18	73.46	74.58	76.64	72.93
Co	7649	7716	Ge	(444)	82.96	79.70	81.84	86.69	78.92
			Si	(533)	78.10	75.95	77.41	79.84	75.37
Ni	8264	8338	Ge	(642)	82.83	79.53	81.80	86.03	78.81
			Si	(444)	73.11	71.51	72.66	74.18	71.10
				(551),(711)	80.51	77.84	79.72	82.62	77.22
Cu	8905	8980	Ge	(800)	79.86	77.47	79.16	81.64	76.91
			Si	(642)	73.57	72.03	73.14	74.59	71.64
				(553),(731)	79.91	77.51	79.22	81.71	76.95
Zn	9572	9659	Ge	(660),(822)	76.26	74.27	75.78	77.41	73.86
				(555),(751)	82.48	79.24	81.62	84.93	78.63
			Si	(800)	72.55	70.97	72.18	73.44	70.63
				(733)	77.45	75.30	76.92	78.73	74.85

Table A.1: Selected Bragg angles for $3d$ transition metal Kβ lines. $E_{1,3}$ and $E_{2,5}$ give energies of K$\beta_{1,3}$ and K$\beta_{2,5}$ lines in eV[56]. The corresponding Bragg angles are given by $\theta(E)$. If only the main Kβ peak is of interest, then the required angular range is from $\theta(E_{1,3}+20)$ to $\theta(E_{1,3}-45)$. To include the valence emission, the lower Bragg angle should be extended to $\theta(E_{2,5}+20)$.

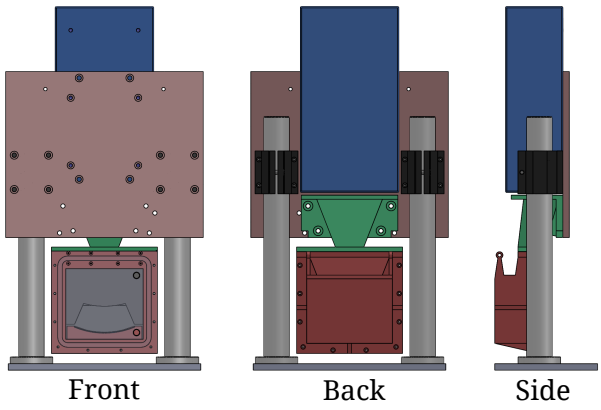

Figure A.3: (Color online). A rendering of the full spectrometer assembly. The side view is looking downstream along the beam.

to limit background from He scatter.

The spectrometer and detector are mounted together on an aluminum-alloy plate that is supported by two large optical posts attached to a lower aluminum-alloy mounting plate. A 3D rendering of the complete assembly is shown in Fig. A.3 and a photograph of the spectrometer is shown in Fig. A.4.

A.2.3 Sample preparation and beamline details

As reference samples, we used two pressed-powder pellets. One was 13-mm diameter, ∼1-mm thick pellet of pure Fe_3O_4. The other was a 7-mm diameter pellet of FeS diluted in BN/PVP to $\sim$ 0.12 absorption lengths of Fe. These were mounted inside a separate He enclosure that was on an independent translation stage.

All measurements were performed at the 20-ID-B beamline[133] of the Advanced Photon Source (APS) at Argonne National Labs. X-ray radiation from an undulator passes through a liquid-nitrogen cooled Si (111) double crystal monochromator resulting in a beam with ∼0.8-eV energy resolution near 7 keV which is focused down to a 30-μm diameter spot using Kirkpatrick-Baez mirrors. The flux incident on the sample was $\sim 10^{12}$ photons/s. The monochromator energy was calibrated by setting the first-derivative zero crossing of

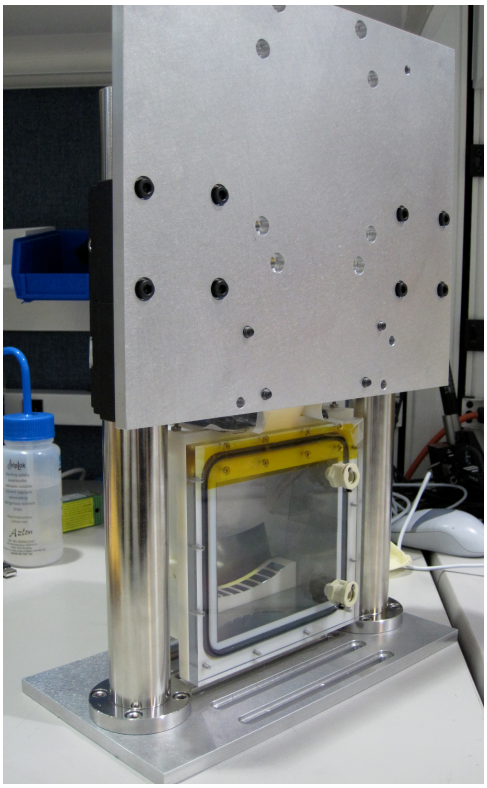

Figure A.4: (Color online). A photograph of the Fe $K\beta$ spectrometer, viewed from the opposite perspective as Fig. A.2.

an Fe foil K-edge transmission scan to 7110.75 eV[170]. As mentioned above, we used a commercial 2D position-sensitive area detector (Dectris Pilatus 100K) with 497×195 pixels of dimension 172×172 μm^2 covering a region 83.8×33.5 mm^2.

A.2.4 Installation

Installing the spectrometer at the beamline is straightforward and typically takes less than an hour. The assembled spectrometer is mounted on a three-axis translation stage and roughly aligned with the focus of the x-ray beam. Precise alignment normal to the beam direction is performed using circular alignment posts (see Fig. A.2) by translating the spectrometer while measuring the transmitted x-ray intensity using a downstream gas ionization chamber. Large samples can typically be aligned transverse to the beam by eye by sighting through the alignment posts. For smaller samples a combination of transmission measurements and fluorescence detection using a nearby solid state detector can be used. Longitudinal alignment is then performed using the symmetry of elastic scattering arcs on the 2D-PSD. Once aligned, test exposures are used to reveal any radiation leaks to the detector. Lead tape is then applied as remedy.

A.3 Spectrometer Operation and Results

We now discuss the spectrometer operation, calibration and data processing procedures and present typical results. All processing routines are implemented in a multi-platform Python software package that is available from the authors. This package allows data to be quickly and easily processed while at the beamline. It is modular, extensible and can be scripted for processing large data sets.

A.3.1 Calibration

Although it is straightforward to calculate the theoretical response function for each pixel on the detector from the designed geometry, the rapid prototyping procedure and crystal fabrication both have limited precision. For crystal mounting surfaces of dimension 15 mm $\times$ 8 mm, the maximum angular deviation from the specification was 0.1°. This corresponds

to a maximum shift of 0.5 eV at a given pixel on the detector. The detected energy at a pixel is also sensitive to the sample location along the beam. To alleviate the need for precision manufacturing and sample alignment, we use an *in situ* calibration procedure[57] to assign an energy value to each pixel on the detector face.

We take a series of exposures while scanning the incident beam energy over the spectrometer's detected energy range. The dominant signal during this scan is elastic scatter off of the sample. Placing the sample in a He enclosure prevents elastic scatter from air close to the sample which would otherwise also be present in the calibration data.

Fig. A.5a shows a composite image formed from such a scan consisting of 15 exposures taken at 10-eV steps from 7000 to 7140 eV. The ten columns in the figure contain radiation that has been Bragg reflected from each of the ten Ge crystals. The effects of crystal misalignment are clearly seen in the occasional small overlap between the images from neighboring crystals, as seen in Fig. A.6. Additionally, two crystals (with images 3rd and 8th from left in Fig. A.6) were misaligned enough to cause the apertures to cut off the region near the top of the PSD image. This cutoff is also evident in the raw calibration exposures (not shown).

The integration time required for the calibration exposures depends on the elastic scattering cross section. For this sample, we integrated for 10 s (60 s) per exposure for incident energies below (above) 7125 eV. The longer integration time was necessary above the Fe K-absorption edge to clearly separate elastic scatter from Fe $K\beta$ valence emission.

Next, we define the regions that correspond to Bragg reflection from each crystal (filled areas of Fig. A.5b). At this step we exclude regions that contain overlap from two crystals and those cut off due to misalignment. For each column of pixels within the defined regions, we find the center of the elastic line using a windowed average about the maximum. Then, we fit the energy as function of pixel coordinate to a quartic polynomial over the region exposed by each analyzer crystal and evaluate the fit at the centers of each pixel producing the calibration matrix shown in Fig. A.5b. The RMS deviation of the input points from the fit is typically under 0.1 eV.

From the calibration exposures it is possible to determine the energy resolution of the spectrometer. We point out that this is not constant, and varies over the energy range of the

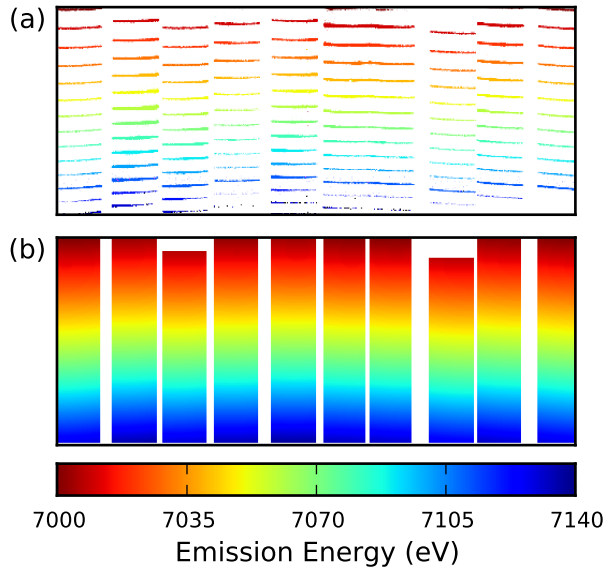

Figure A.5: (Color online). (a) A composite image formed from 15 exposures taken at evenly spaced incident beam energies across the range of the spectrometer. (b) The calibrated 2D-PSD face.

spectrometer due to the nonlinearity of Bragg's law. The measured full width at half max (FWHM) of elastic scatter ranged between 1.0 and 1.3 eV from low to high energy. This includes the bandwidth of the incident beam, which varies from $\sim 0.8 - 0.9$ over this energy range. After deconvolution, this is in agreement with the designed spectrometer resolution of $\sim 0.5 - 0.9$ eV/pixel when moving from low energy (7000 eV) to high energy (7140 eV). This is also consistent with the change in the calibration matrix between neighboring pixels in the dispersive direction.

Since the detected energy range for this spectrometer contains the Fe K-absorption edge, fluorescence emission is also present in calibration exposures taken with the incident beam above the edge. The main $K\beta$ peak can be easily filtered out since it only has intensity when the elastic line is well above and thus geometrically well separated from the fluorescence. However, for samples with a weak elastic-scattering cross section, the valence emission is comparable in intensity to elastic scatter at the valence emission energy. In this case, locating the elastic peak in software is difficult. Since the detected range extends above the Fermi energy, the spectrometer can still be calibrated by simply skipping over the small valence emission range in the calibration scan.

Comparison of multiple calibration scans taken at the same sample spot places the average uncertainty in the energy assignment of a pixel at 0.02 eV relative to the monochromator calibration. The maximum deviation for any single pixel between two different calibration matrices was less than 0.1 eV.

Since the calibration depends on the exact location at which the beam intersects the sample, the spectrometer must be recalibrated whenever the beam spot on the sample moves by a significant amount (on the scale of the pixel size) relative to the spectrometer. Note that if the sample moves while the beam remains fixed, the intersection point can only move longitudinally. This is in the non-dispersive direction (horizontal in Fig. A.5), along which the calibration changes slowly. Failure to recalibrate will then primarily result in a loss of resolution rather than a systematic energy shift. Best practice is to recalibrate after switching samples. However, in cases where this is not feasible, it is possible to re-align a sample well enough that prior calibration can be used[213]. Additionally, one application of miniXES is for microprobe XES studies of geological sections[212]. In this case, if the

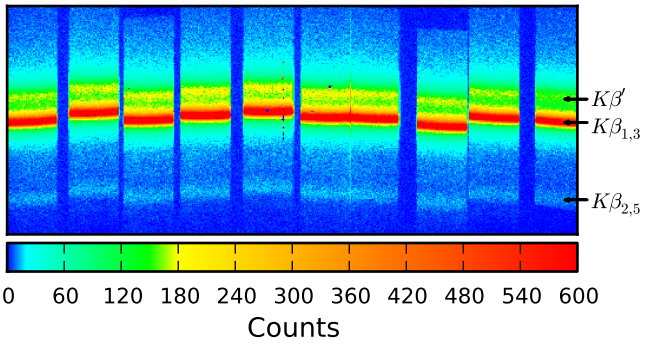

Figure A.6: (Color online). A 300-s exposure of Fe_3O_4 $K\beta$ fluorescence at 7800-eV incident energy. Emission energy runs vertically downward. A nonlinear color scale was chosen to highlight the labeled spectral features. The incident flux was $\sim 10^{12}$ photons/s.

surface is sufficiently flat and can be mounted parallel to the translation axes of a translation stage, it is possible to quickly perform 2D scans using only a single calibration.

A.3.2 Emission Spectra

Fig. A.6 shows a five-minute exposure of non-resonant $K\beta$ emission from a pressed Fe_3O_4 pellet. The incident beam energy was 7800 eV; far enough above the Fe K-absorption edge that the Compton-scattering peak fell well outside the spectrometer range. The incident flux was $\sim 10^{12}$ s^{-1}. The raw counts at each pixel of this exposure are combined with the energy values from the calibration matrix (Fig. A.5b) to produce the emission spectrum shown in Fig. A.7a.

First, however, some filtering is necessary to remove erroneous counts from bad pixels in the detector, as visible in Fig. A.6, especially along a vertical line near the center. Typically, bad pixels in this type of detector produce counts several orders of magnitude above the signal level, and can be simply filtered out using a low pass filter with a cutoff placed safely above the fluorescence peak. However, some pixels from this particular detector unit registered erroneous counts at the level of the signal. These were located using dark exposures and then masked out in later processing.

Across the region exposed by a single analyzer crystal, the solid angle subtended by a pixel varies by $\sim$ 7%, and this variation is largely correlated with energy. Hence, we normalize to counts / sr using solid angles calculated from the design specification. Since this does not take sample or analyzer crystal misalignment into account, a slight systematic uncertainty remains. However, for estimated misalignment, this is at the level of one part in 10^{-4} and thus can be neglected relative to typical statistical uncertainties.

Each 1-pixel wide column in a calibrated region of the spectrometer forms a complete, albeit low count, spectrum. Although it is possible to simply bin the data, the distribution of pixel energies is not uniform and binned spectra can contain systematic uncertainty due to bins having uneven weights for pixels from different analyzer crystals (which may have differing net efficiencies). So, instead, we interpolate the spectra from each column onto a common energy grid and then average over the columns. This procedure ensures that all points in the final spectrum include an average over all analyzer crystals.

A spectrum generated in this fashion is independent of the spacing chosen for the energy grid. That is, for two different grids that contain a common energy value, the corresponding intensity value will be identical. The spectra shown in Fig. A.7 are oversampled onto an energy grid with 0.1 eV spacing. Neighboring points in this oversampled spectrum are not statistically independent. However, the fluctuations in $K\beta_{2,5}$ region of the spectrum (shown at a larger scale in Fig. A.7) have a spacing consistent with the spectrometer resolution, and have amplitudes consistent with Poisson statistics. Also visible in Fig. A.7b is the $K\beta''$ peak which results from a ligand 2s electron filling the metal 1s corehole[100]. Both spectra in Fig. A.7 are in good agreement with published results[298, 242] after broadening our spectra to match the instrumental resolutions in the cited works. The background level (visible beneath the $K\beta_{2,5}$ in Fig. A.7) is noticably larger than that in spectra obtained with SBCA-based spectrometers[183]. We believe that the dominant source of this background is from photons outside the desired energy range scattering from the interior of the spectrometer, e.g., Compton scattering of Fe $K\alpha$ fluorescence off of the Ge analyzer crystals.

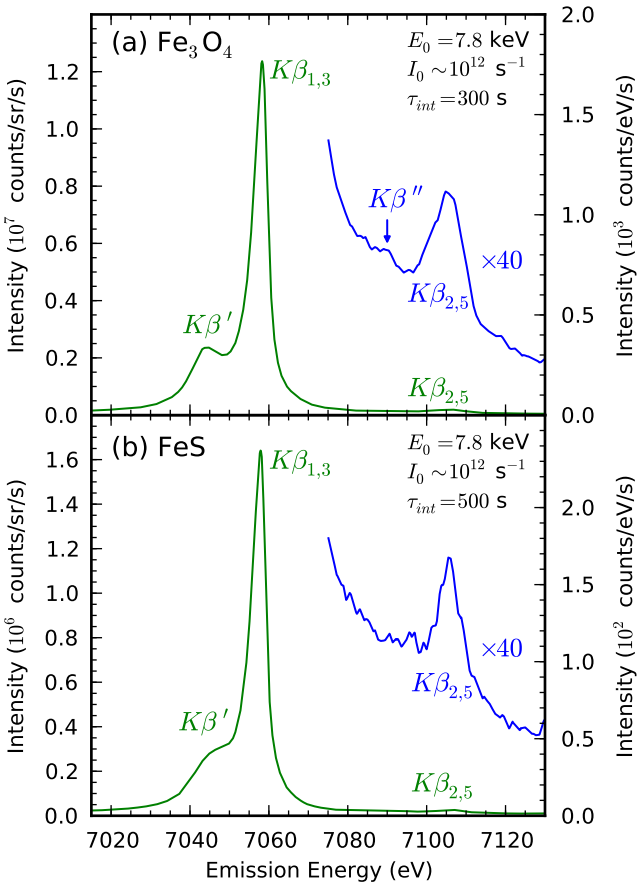

Figure A.7: (Color online). $K\beta$ emission spectra for (a) Fe_3O_4 (corresponding to raw data in Fig. A.6) and (b) FeS. The incident beam was at 7.8 keV, with an incident flux $\sim 10^{12}$ photons/s. The integration time was 300 s and 500 s respectively. Note that the scale for FeS is an order of magnitude smaller than for Fe_3O_4 due to the sample being substantially thinner than an absorption length. The scale on the left side shows counts/sr/s. The scale on the right is normalized to counts/eV/s. The total integrated counts rates are 18,800 and 2,500 cps respectively.

A.3.3 Photometrics

Given the successful performance of this instrument, the question of its efficiency with respect to traditional, SBCA-based spectrometers naturally arises. Direct, quantitative comparisons are difficult because of differences in sample preparation, in addition to other, typically not published, experimental details. That being said, any instrument can be usefully characterized in terms of its performance relative to theoretical expectation for its efficiency, based on the relevant scattering geometries and the theoretical integral reflectivity of its diffractive optic. Below, we present such an analysis for Fe Kβ miniXES. We quantify the miniXES performance while removing sensitivity to all sample preparation and incident flux issues by comparing the detected signal to the simultaneously measured signal from a solid-state detector. We find that the present instrument is indeed operating at theoretical efficiency, within modest errors. We are unfamiliar with any similarly careful analysis of the performance of an SBCA-based spectrometer for XES studies. Common experience at synchrotron light sources finds that SBCA's often do not perform at the theoretical limit for collection solid angle, as evidenced by substantial variations in performance between different optics having nominally identical fabrication. In this sense, the simplicity of the miniXES optic, *i.e.*, unstrained, flat analyzer crystals, may provide a practical advantage.

To make this analysis as straightforward as possible, we calculate an effective spectrometer efficiency, η_{miniXES}, that gives the probability of Fe $K\beta$ photons that are emitted by, and escape from, the sample to be detected by the instrument. We do the same for a commercial Si drift detector (SDD) and compare experimental results. The experimental countrates presented here are for a 4-μm thick Fe foil with the incident beam at 10 keV.

We treat the sample as an isotropic point-source of fluorescence radiation. For a given energy, a conical lamella with a narrow angular width is reflected by the analyzer crystal. The effective width is determined by the *integral reflectivity*, $\delta\theta$, which is the integral of the rocking curve over Bragg angle and gives a measure of the efficiency of the analyzer crystal. Only a small piece of this conical lamella intersects the active detector region (which accounts for the finite size of the analyzers and the effects of all entrance and exit apertures). Let the non-dispersive angular size of this piece, as seen from the image of

$\Gamma_{\mathrm{miniXES}}$	5815 ± 12 cps
Γ_{SDD}	247212 ± 107 cps
η_{miniXES}	$1.27 \pm 0.05 \times 10^{-6}$
η_{SDD}	$5.26 \pm 0.10 \times 10^{-5}$
$\Gamma_{\mathrm{SDD}}/\Gamma_{\mathrm{miniXES}}$	42.51 ± 0.09
$\eta_{\mathrm{SDD}}/\eta_{\mathrm{miniXES}}$	41.4 ± 1.9

Table A.2: Results of a photometric analysis for the present spectrometer (miniXES) and a commerical Si drift detector (SDD). The ratio of the measured count rates (Γ) is compared to the ratio of the theoretical detector efficiencies (η).

the point source, be $\delta\phi$. Assuming both of these angles are small, the effective collection solid angle for a specific energy is $\Omega = \delta\theta\delta\phi$. Including the effects of absorption along the pathway between sample and detector, η_{abs}, we find

$$\eta_{\mathrm{miniXES}} = \frac{\delta\theta\delta\phi}{4\pi}\eta_{\mathrm{abs}}, \tag{A.1}$$

For the present spectrometer, $\delta\phi = 0.213 \pm 0.003$ rad, with negligible variation over the detected energy range. The weighted average $\delta\theta$ for Ge (620) over the Fe $K\beta$ fluorescence energy range has been calculated using the `GID_sl` software package[267] to be $(8.5 \pm 0.3) \times 10^{-5}$ rad. The dominant absorption effects are due to 3.5 cm of air and 50.8 μm of polyimide windows, giving $\eta_{\mathrm{abs}} = 0.88$. Using these values in Eq. A.1, we find $\eta_{\mathrm{miniXES}} = (1.27 \pm 0.05) \times 10^{-6}$.

The SDD was located 37.0 ± 0.5 cm from the sample in the horizontal plane, $\sim 30^{\circ}$ from backscatter. The active detection region is 1.7 cm^2, giving a total detector solid angle of 1.24 ± 0.07 msr. Including the effect of air absorption on the path from sample to detector, we find the effective efficiency for the SDD to be $\eta_{\mathrm{SDD}} = (5.3 \pm 0.2) \times 10^{-5}$.

The total $K\beta$ countrate was measured for both detectors. The background level in the miniXES data (discussed in section A.3.2) was determined from the count rate in areas between active detector regions. This was then subtracted from the total count rate. The SDD countrate was corrected for detector deadtime using standard techniques. In table A.2, we

present the results and compare the ratio of measured countrates to the ratio of theoretical efficiencies. The results agree to within the errors, which are $\sim 5\%$. Hence, we find that the miniXES performs at the limit of theoretical expectations.

A similar photometric experiment can be performed for SBCA-based instruments. The analogy is most direct when the analyzer is moved off of the Rowland circle and operated in dispersive mode[140]. If an SBCA performs at theoretical efficiency, then a direct comparison can be made with miniXES on the basis of the integral reflectivities and total collection solid angles of the respective instruments.

A.4 Conclusions

We have demonstrated a SWD (miniXES) x-ray emission spectrometer design based on the cylindrical von Hamos geometry, and have shown that the instrument performs at the limit of theoretical efficiency. The use of in-context CAD with embedded geometrical constraints combined with rapid prototype fabrication of plastic parts has proven to be an effective, low-cost approach, and allows the design to be modified to cover different emission lines. Portability and ease of installation, alignment and operation allow this spectrometer to be used at any existing microfocus beamline. Multi-platform processing software contributes to ease of use, allowing data processing to occur at the beamline. Finally, compatibility with environmental chambers and optical access to the sample for pump-probe measurements make this instrument well suited to a wide range of applications.

BIBLIOGRAPHY

[1] Feff manual.

[2] R. Alonso Mori, E. Paris, G. Giuli, S. G. Eeckhout, M. Kavcic, M. Zitnik, K. Bucar, L. G. M. Pettersson, and P. Glatzel. Electronic structure of sulfur studied by x-ray absorption and emission spectroscopy. *Analytical Chemistry*, 81(15):6516–6525, 2009.

[3] N. Amadou, E. Brambrink, A. Benuzzi-Mounaix, G. Huser, F. Guyot, S. Mazevet, G. Morard, T. de Resseguier, T. Vinci, K. Myanishi, N. Ozaki, R. Kodama, T. Boehly, O. Henry, D. Raffestin, and M. Koenig. Direct laser-driven ramp compression studies of iron: A first step toward the reproduction of planetary core conditions. *High Energy Density Physics*, 9(2):243 – 246, 2013.

[4] U. Andiel, K. Eidmann, F. Pisani, K. Witte, I. Uschmann, O. Wehrhan, and E. Forster. Conical x-ray crystal spectrometer for time integrated and time resolved measurements. *Review of Scientific Instruments*, 74(4):2369, 2003.

[5] A. L. Ankudinov, B. Ravel, J. J. Rehr, and S. D. Conradson. Real-space multiple-scattering calculation and interpretation of x-ray-absorption near-edge structure. *Physical Review B*, 58(12):7565–7576, September 1998.

[6] A.L. Ankudinov, S.I. Zabinsky, and J.J. Rehr. Single configuration dirac-fock atom code. *Computer Physics Communications*, 98(3):359 – 364, 1996.

[7] N. W. Ashcroft and J. Lekner. Structure and resistivity of liquid metals. *Phys. Rev.*, 145:83–90, May 1966.

[8] Neil W. Ashcroft and David N. Mermin. *Solid state physics*. Thomson Learning, Toronto, 1 edition, January 1976.

[9] James Badro, Guillaume Fiquet, Francois Guyot, Jean-Pascal Rueff, Viktor V. Struzhkin, Gyorgy Vanko, and Giulio Monaco. Iron partitioning in earth's mantle: Toward a deep lower mantle discontinuity. *Science*, 300:789–791, 2003.

[10] James Badro, Guillaume Fiquet, Viktor V. Struzhkin, Maddury Somayazulu, Ho-kwang Mao, Guoyin Shen, and Tristan Le Bihan. Nature of the high-pressure transition in Fe_2o_3 hematite. *Physical Review Letters*, 89:205504, 2002.

[11] James Badro, Jean-Pascal Rueff, Gyorgy Vanko, Giulio Monaco, Guillaume Fiquet, and Francois Guyot. Electronic transitions in perovskite: Possible nonconvecting layers in the lower mantle. *Science*, 305(5682):383–386, 2004.

[12] M. Balasubramanian, C. S. Johnson, J. O. Cross, G. T. Seidler, T. T. Fister, E. A. Stern, C. Hamner, and S. O. Mariager. Fine structure and chemical shifts in nonresonant inelastic x-ray scattering from li-intercalated graphite. *Applied Physics Letters*, 91(3):031904, 2007.

[13] M. Balasubramanian, C. S. Johnson, J. O. Cross, G. T. Seidler, T. T. Fister, E. A. Stern, C. Hamner, and S. O. Mariager. Fine structure and chemical shifts in nonresonant inelastic x-ray scattering from li-intercalated graphite. *Applied Physics Letters*, 91(3):031904, 2007.

[14] A. Bansil, R. S. Rao, P. E. Mijnarends, and L. Schwartz. Electron momentum densities in disordered muffin-tin alloys. *Physical Review B*, 23:3608–3616, April 1981.

[15] B. Barbiellini, Ch, G. Loupias, T. Buslaps, and A. Shukla. How the hydrogen bond in nh_4f is revealed with compton scattering. *Physical Review B*, 79:155115, April 2009.

[16] B. Barbiellini, A. Koizumi, P. E. Mijnarends, W. Al Sawai, Hsin Lin, T. Nagao, K. Hirota, M. Itou, Y. Sakurai, and A. Bansil. Role of oxygen electrons in the metal-insulator transition in the magnetoresistive oxide $la_{2-2x}sr_{1+2x}mn_2o_7$ probed by compton scattering. *Physical Review Letters*, 102:206402, May 2009.

[17] U. von Barth and L. Hedin. A local exchange-correlation potential for the spin polarized case. i. *Journal of Physics C: Solid State Physics*, 5(13):1629–1642, July 1972.

[18] F Bell. Compton profiles by the 1. born approximation. *Zeitschrift für Physik D*, 3:97–98, 1986.

[19] L. Bellaiche and K. Kunc. Core effects in lithium hydride. *Phys. Rev. B*, 55(8), 1997.

[20] Lorin X. Benedict, Tadashi Ogitsu, Andrea Trave, Christine J. Wu, Philip A. Sterne, and Eric Schwegler. Calculations of high-pressure properties of beryllium: Construction of a multiphase equation of state. *Phys. Rev. B*, 79:064106, Feb 2009.

[21] U. Bergmann, Ph, P. Glatzel, M. Cavalleri, L. G. M. Pettersson, A. Nilsson, and S. P. Cramer. X-ray raman spectroscopy at the oxygen K edge of water and ice: implications on local structure models. *Physical Review B*, 66:092107, September 2002.

[22] Uwe Bergmann and Steve P. Cramer. A high-resolution large-acceptance analyzer for x-ray fluorescence and raman spectroscopy. *Proc. SPIE*, 3448:198, 1998.

[23] Uwe Bergmann, Andrea Di Cicco, Philippe Wernet, Emiliano Principi, Pieter Glatzel, and Anders Nilsson. Nearest-neighbor oxygen distances in liquid water and ice observed by x-ray raman based extended x-ray absorption fine structure. *The Journal of Chemical Physics*, 127(17):174504, 2007.

[24] Uwe Bergmann, Pieter Glatzel, and Stephen P. Cramer. Bulk-sensitive XAS characterization of light elements: from x-ray raman scattering to x-ray raman spectroscopy. *Microchemical Journal*, 71(2-3):221–230, April 2002.

[25] Felix Bloch. Über die quantenmechanik der elektronen in kristallgittern. *Zeitschrift für Physik*, 52:555–600, 1929.

[26] P. E. Blöchl. Projector augmented-wave method. *Phys. Rev. B*, 50:17953–17979, Dec 1994.

[27] David Bohm and David Pines. A collective description of electron interactions: Iii. coulomb interactions in a degenerate electron gas. *Phys. Rev.*, 92:609–625, Nov 1953.

[28] Amelie Bordage, Etienne Balan, Johan P. R. de Villiers, Robert Cromarty, Amelie Juhin, Claire Carvallo, Georges Calas, P. V. Sunder Raju, and Pieter Glatzel. V oxidation state in Fe-Ti oxides by high-energy resolution fluorescence-detected X-ray absorption spectroscopy. *Physics and Chemistry of Minerals*, 38(6):449, 2011.

[29] C. R. Bradley, M. L. Wroge, A. K. Dozier, and P. C. Gibbons. White lines at K edges of light atoms. *Phys. Rev. B*, 31:5066–5070, Apr 1985.

[30] J. A. Bradley, Sen S. Gupta, G. T. Seidler, K. T. Moore, M. W. Haverkort, G. A. Sawatzky, S. D. Conradson, D. L. Clark, S. A. Kozimor, and K. S. Boland. Probing electronic correlations in actinide materials using multipolar transitions. *Physical Review B*, 81:193104, May 2010.

[31] J. A. Bradley, A. Sakko, G. T. Seidler, A. Rubio, M. Hakala, K. Hämäläinen, G. Cooper, A. P. Hitchcock, K. Schlimmer, and K. P. Nagle. Reexamining the lyman-birge-hopfield band of n_2. *Physical Review A*, 84:022510, August 2011.

[32] J. A. Bradley, A. Sakko, G. T. Seidler, A. Rubio, M. Hakala, K. Hämäläinen, G. Cooper, A. P. Hitchcock, K. Schlimmer, and K. P. Nagle. Reexamining the lyman-birge-hopfield band of n_2. *Phys. Rev. A*, 84:022510, Aug 2011.

[33] J. A. Bradley, G. T. Seidler, G. Cooper, M. Vos, A. P. Hitchcock, A. P. Sorini, C. Schlimmer, and K. P. Nagle. Comparative study of the valence electronic excitations of $\mathbf{n}_2$ by inelastic x-ray and electron scattering. *Physical Review Letters*, 105:053202, July 2010.

[34] J. A. Bradley, G. T. Seidler, G. Cooper, M. Vos, A. P. Hitchcock, A. P. Sorini, C. Schlimmer, and K. P. Nagle. Comparative study of the valence electronic excitations of $\mathbf{n}_2$ by inelastic x-ray and electron scattering. *Phys. Rev. Lett.*, 105:053202, Jul 2010.

[35] Joseph A. Bradley, Ping Yang, Enrique R. Batista, Kevin S. Boland, Carol J. Burns, David L. Clark, Steven D. Conradson, Stosh A. Kozimor, Richard L. Martin, Gerald T. Seidler, Brian L. Scott, David K. Shuh, Tolek Tyliszczak, Marianne P. Wilkerson,

and Laura E. Wolfsberg. Experimental and theoretical comparison of the o K-Edge nonresonant inelastic x-ray scattering and x-ray absorption spectra of NaReO4. *J. Am. Chem. Soc.*, 132(39):13914–13921, September 2010.

[36] Joseph A. Bradley, Ping Yang, Enrique R. Batista, Kevin S. Boland, Carol J. Burns, David L. Clark, Steven D. Conradson, Stosh A. Kozimor, Richard L. Martin, Gerald T. Seidler, Brian L. Scott, David K. Shuh, Tolek Tyliszczak, Marianne P. Wilkerson, and Laura E. Wolfsberg. Experimental and theoretical comparison of the o k-edge nonresonant inelastic x-ray scattering and x-ray absorption spectra of nareo4. *Journal of the American Chemical Society*, 132(39):13914–13921, Oct 2010.

[37] G. Breit. A correspondence principle in the compton effect. *Phys. Rev.*, 27:362–372, Apr 1926.

[38] M. Brown, R. E. Peierls, and E. A. Stern. White lines in x-ray absorption. *Phys. Rev. B*, 15:738–744, Jan 1977.

[39] W. A. Caliebe, J. A. Soininen, Eric L. Shirley, C. C. Kao, and K. Hämäläinen. Dynamic structure factor of diamond and LiF measured using inelastic X-Ray scattering. *Physical Review Letters*, 84:3907–3910, April 2000.

[40] D. A. Chapman and D. O. Gericke. Analysis of thomson scattering from nonequilibrium plasmas. *Physical Review Letters*, 107:165004, October 2011.

[41] J. Chihara. Difference in x-ray scattering between metallic and non-metallic liquids due to conduction electrons. *Journal of Physics F: Metal Physics*, 17(2):295, February 1987.

[42] Junzo Chihara. Interaction of photons with plasmas and liquid metals - photoabsorption and scattering. *Journal of Physics: Condensed Matter*, 12(3):231, 2000.

[43] Junzo Chihara. Interaction of photons with plasmas and liquid metals - photoabsorption and scattering. *Journal of Physics: Condensed Matter*, 12(3):231, January 2000.

[44] O. Ciricosta, S. M. Vinko, H.-K. Chung, B.-I. Cho, C. R. D. Brown, T. Burian, J. Chalupský, K. Engelhorn, R. W. Falcone, C. Graves, V. Hájková, A. Higginbotham, L. Juha, J. Krzywinski, H. J. Lee, M. Messerschmidt, C. D. Murphy, Y. Ping, D. S. Rackstraw, A. Scherz, W. Schlotter, S. Toleikis, J. J. Turner, L. Vysin, T. Wang, B. Wu, U. Zastrau, D. Zhu, R. W. Lee, P. Heimann, B. Nagler, and J. S. Wark. Direct measurements of the ionization potential depression in a dense plasma. *Phys. Rev. Lett.*, 109:065002, Aug 2012.

[45] E. Clementi and D. L. Raimondi. Atomic screening constants from scf functions. *The Journal of Chemical Physics*, 38(11):2686–2689, 1963.

[46] J. Clerouin, P. Noiret, P. Blottiau, V. Recoules, B. Siberchicot, P. Renaudin, C. Blancard, G. Faussurier, B. Holst, and C. E. Starrett. A database for equations of state and resistivities measurements in the warm dense matter regime. *Physics of Plasmas*, 19(8):082702, 2012.

[47] Arthur H. Compton. A quantum theory of the scattering of x-rays by light elements. *Physical Review*, 21:483–502, May 1923.

[48] Arthur H. Compton and Y. H. Woo. The wave-length of molybdenum k rays when scattered by light elements. *Proceedings of the National Academy of Sciences*, 10(6):271–273, 1924.

[49] Heiko Conrad, Felix Lehmkühler, Christian Sternemann, Arto Sakko, Dietmar Paschek, Laura Simonelli, Simo Huotari, Omid Feroughi, Metin Tolan, and Keijo Hämäläinen. Tetrahydrofuran clathrate hydrate formation. *Physical Review Letters*, 103(21):218301, November 2009.

[50] M. Cooper, P. Pattison, B. Williams, and K. C. Pandey. The compton profile of aluminum. *Philosophical Magazine*, 29:1237, 1974.

[51] M. J. Cooper, P. E. Mijnarends, N. Shiotani, N. Sakai, and A. Bansil. *X-Ray Compton Scattering*. Oxford Series on Synchrotron Radiation. Oxford University Press, 2004.

[52] M. J. Cooper, P. E. Mijnarends, N. Shiotani, N. Sakai, and A. Bansil. *X-Ray Compton Scattering*. Oxford Series on Synchrotron Radiation. Oxford University Press, 2004.

[53] R. Currat, P. D. DeCicco, and Roy Kaplow. Compton scattering and electron momentum density in beryllium. *Phys. Rev. B*, 3:243–251, Jan 1971.

[54] F. de Groot. High-resolution x-ray emission and x-ray absorption spectroscopy. *Chemical Reviews*, 101(6):1779, 2001.

[55] F. M. F. de Groot, M. H. Krisch, and J. Vogel. Spectral sharpening of the pt L edges by high-resolution x-ray emission. *Physical Review B*, 66:195112, 2002.

[56] Richard D. Deslattes, Ernest G. Kessler, P. Indelicato, L. de Billy, E. Lindroth, J. Anton, J.S. Coursey, D.J. Schwab, C. Chang, R. Sukumar, K. Olsen, and R.A. Dragoset. X-ray transition energies (version 1.2), Sep 2011.

[57] B. Dickinson, G. T. Seidler, Z. W. Webb, J. A. Bradley, K. P. Nagle, S. M. Heald, R. A. Gordon, and I. M. Chou. A short working distance multiple crystal x-ray spectrometer. *Review of Scientific Instruments*, 79:123112, 2008.

[58] P. A. M. Dirac. *Proc. Roy. Soc. Lond. A*, 111:405–423, June 1926.

[59] S. Doniach, P. M. Platzman, and J. T. Yue. X-Ray raman scattering in metals. *Physical Review B*, 4:3345–3350, November 1971.

[60] T. Döppner, O. L. Landen, H. J. Lee, P. Neumayer, S. P. Regan, and S. H. Glenzer. Temperature measurement through detailed balance in x-ray thomson scattering. *High Energy Density Physics*, 5(3):182–186, September 2009.

[61] T. Döppner, O.L. Landen, H.J. Lee, P. Neumayer, S.P. Regan, and S.H. Glenzer. Temperature measurement through detailed balance in x-ray thomson scattering. *High Energy Density Physics*, 5(3):182 – 186, 2009.

[62] R.P. Drake. *High-Energy-Density Physics*. Shock Wave and High Pressure Phenomena. Springer, Berlin, 2006.

[63] Jesse W. M. Du Mond. Experimental confirmation for sommerfeld-fermi-dirac degenerate gas theory of conduction electrons. *Science*, 9(1767):452, 1928.

[64] Jesse W. M. Du Mond. Compton modified line structure and its relation to the electron theory of solid bodies. *Phys. Rev.*, 33:643–658, May 1929.

[65] Jesse W. M. Du Mond. The linear momenta of electrons in atoms and in solid bodies as revealed by x-ray scattering. *Rev. Mod. Phys.*, 5:1–33, Jan 1933.

[66] James W. Dufty and S. B. Trickey. Scaling, bounds, and inequalities for the noninteracting density functionals at finite temperature. *Phys. Rev. B*, 84:125118, Sep 2011.

[67] S. B. Dugdale and T. Jarlborg. Thermal disorder versus correlation in compton profiles from alkali metals. *Solid State Communications*, 105(5):283–287, February 1998.

[68] Jesse W. M. Dumond. Experimental confirmation for sommerfeld-fermi-dirac degenerate gas theory of conduction electrons. *Science*, 9(1767):452, 1928.

[69] J.W.M. DuMond and H.A. Kirkpatrick. *Review of Scientific Instruments*, 1:88, 1930.

[70] G. Ecker and W. Kroll. Lowering of the ionization energy for a plasma in thermodynamic equilibrium. *Physics of Fluids*, 6(1):62–69, 1963.

[71] P. Eisenberger and P. M. Platzman. Compton scattering of x rays from bound electrons. *Physical Review A*, 2:415–423, 1970.

[72] P. Eisenberger and P. M. Platzman. Compton scattering of x rays from bound electrons. *Physical Review A*, 2:415–423, August 1970.

[73] Irving R. Epstein. Calculation of atomic and molecular momentum expectation values and total energies from compton-scattering data. *Phys. Rev. A*, 8:160–168, Jul 1973.

[74] A. Erba, M. Itou, Y. >Sakurai, R. Yamaki, M. Ito, S. Casassa, L. Maschio, A. Terentjevs, and C. Pisani. Beyond a single-determinantal description of the density matrix of periodic systems: Experimental versus theoretical compton profiles of crystalline silicon. *Physical Review B*, 83:125208, March 2011.

[75] S. Ergun. Optical studies of carbon. *Chem. Phys. Carbon*, 3, 1968.

[76] R. R. Fäustlin, Th, T. Döppner, S. Düsterer, E. Förster, C. Fortmann, S. H. Glenzer, S. Göde, G. Gregori, R. Irsig, T. Laarmann, H. J. Lee, B. Li, K. H. Meiwes Broer, J. Mithen, B. Nagler, A. Przystawik, H. Redlin, R. Redmer, H. Reinholz, G. Röpke, F. Tavella, R. Thiele, J. Tiggesbäumker, S. Toleikis, I. Uschmann, S. M. Vinko, T. Whitcher, U. Zastrau, B. Ziaja, and Th. Observation of ultrafast nonequilibrium collective dynamics in warm dense hydrogen. *Physical Review Letters*, 104:125002, March 2010.

[77] Yejun Feng, G. T. Seidler, J. O. Cross, A. T. Macrander, and J. J. Rehr. Role of inversion symmetry and multipole effects in nonresonant x-ray raman scattering from icosahedral b_4C. *Physical Review B*, 69:125402, March 2004.

[78] Yejun Feng, G. T. Seidler, J. O. Cross, A. T. Macrander, and J. J. Rehr. Role of inversion symmetry and multipole effects in nonresonant x-ray raman scattering from icosahedral b_4C. *Phys. Rev. B*, 69:125402, Mar 2004.

[79] Yejun Feng, J. A. Soininen, A. L. Ankudinov, J. O. Cross, G. T. Seidler, A. T. Macrander, J. J. Rehr, and E. L. Shirley. Exciton spectroscopy of hexagonal boron nitride using nonresonant x-ray raman scattering. *Physical Review B*, 77:165202, April 2008.

[80] O. M. Feroughi, C. Sternemann, Ch, M. A. Schroer, H. Sternemann, H. Conrad, A. Hohl, G. T. Seidler, J. Bradley, T. T. Fister, M. Balasubramanian, A. Sakko, K. Pirkkalainen, K. Hämäläinen, and M. Tolan. Phase separation and si nanocrystal formation in bulk SiO studied by x-ray scattering. *Applied Physics Letters*, 96(8):081912, 2010.

[81] O. M. Feroughi, C. Sternemann, Ch. J. Sahle, M. A. Schroer, H. Sternemann, H. Conrad, A. Hohl, G. T. Seidler, J. Bradley, T. T. Fister, M. Balasubramanian, A. Sakko, K. Pirkkalainen, K. Hämäläinen, and M. Tolan. Phase separation and si

nanocrystal formation in bulk sio studied by x-ray scattering. *Applied Physics Letters*, 96(8):081912, 2010.

[82] T. T. Fister, D. D. Fong, J. A. Eastman, H. Iddir, P. Zapol, P. H. Fuoss, M. Balasubramanian, R. A. Gordon, K. R. Balasubramaniam, and P. A. Salvador. Total-reflection inelastic x-ray scattering from a 10-nm thick $la_{0.6}sr_{0.4}coo_3$ thin film. *Physical Review Letters*, 106:037401, January 2011.

[83] T. T. Fister, G. T. Seidler, C. Hamner, J. O. Cross, J. A. Soininen, and J. J. Rehr. Background proportional enhancement of the extended fine structure in nonresonant inelastic x-ray scattering. *Phys. Rev. B*, 74:214117, Dec 2006.

[84] T. T. Fister, G. T. Seidler, L. Wharton, A. R. Battle, T. B. Ellis, J. O. Cross, A. T. Macrander, W. T. Elam, T. A. Tyson, and Q. Qian. Multielement spectrometer for efficient measurement of the momentum transfer dependence of inelastic x-ray scattering. *Review of Scientific Instruments*, 77(6):063901, 2006.

[85] T. T. Fister, G. T. Seidler, L. Wharton, A. R. Battle, T. B. Ellis, J. O. Cross, A. T. Macrander, W. T. Elam, T. A. Tyson, and Q. Qian. Multielement spectrometer for efficient measurement of the momentum transfer dependence of inelastic x-ray scattering. *Review of Scientific Instruments*, 77(6):063901, 2006.

[86] T. T. Fister, G. T. Seidler, L. Wharton, A. R. Battle, T. B. Ellis, J. O. Cross, A. T. Macrander, W. T. Elam, T. A. Tyson, and Q. Qian. Multielement spectrometer for efficient measurement of the momentum transfer dependence of inelastic x-ray scattering. *Review of Scientific Instruments*, 77(6):063901, 2006.

[87] Tim T. Fister, Moritz Schmidt, Paul Fenter, Chris S. Johnson, Michael D. Slater, Maria K. Y. Chan, and Eric L. Shirley. Electronic structure of lithium battery interphase compounds: Comparison between inelastic x-ray scattering measurements and theory. *The Journal of Chemical Physics*, 135(22):224513, 2011.

[88] Tim T. Fister, Moritz Schmidt, Paul Fenter, Chris S. Johnson, Michael D. Slater, Maria K. Y. Chan, and Eric L. Shirley. Electronic structure of lithium battery inter-

phase compounds: Comparison between inelastic x-ray scattering measurements and theory. *The Journal of Chemical Physics*, 135(22):224513, 2011.

[89] Timothy T. Fister, Kenneth P. Nagle, Fernando D. Vila, Gerald T. Seidler, Christopher Hamner, Julie O. Cross, and John J. Rehr. Intermediate-range order in water ices: Nonresonant inelastic x-ray scattering measurements and real-space full multiple scattering calculations. *Phys. Rev. B*, 79:174117, May 2009.

[90] Timothy T. Fister, Fernando D. Vila, Gerald T. Seidler, Lukas Svec, John C. Linehan, and Julie O. Cross. Local electronic structure of dicarba-closo-dodecarboranes C2B10H12. *J. Am. Chem. Soc.*, 130(3):925–932, December 2007.

[91] Timothy T. Fister, Fernando D. Vila, Gerald T. Seidler, Lukas Svec, John C. Linehan, and Julie O. Cross. Local electronic structure of dicarba- closo -dodecarboranes c 2 b 10 h 12. *Journal of the American Chemical Society*, 130(3):925–932, Jan 2008.

[92] L. B. Fletcher, A. Kritcher, A. Pak, T. Ma, T. Doppner, C. Fortmann, L. Divol, O. L. Landen, J. Vorberger, D. A. Chapman, D. O. Gericke, R. W. Falcone, and S. H. Glenzer. X-ray thomson scattering measurements of temperature and density from multi-shocked ch capsules. *Physics of Plasmas*, 20(5):056316, 2013.

[93] Richard A. Forman, Gasper J. Piermarini, J. Dean Barnett, and Stanley Block. Pressure measurement made by the utilization of ruby sharp-line luminescence. *Science*, 176(4032):284–285, 1972.

[94] E. Forster, K. Gabel, and I. Uschmann. New crystal spectrograph designs and their application to plasma diagnostics (invited). *Review of Scientific Instruments*, 63(10):5012–5016, 1992.

[95] C. Fortmann, T. Bornath, R. Redmer, H. Reinholz, G. Röpke, V. Schwarz, and R. Thiele. X-ray thomson scattering cross-section in strongly correlated plasmas. *Laser and Particle Beams*, 27(02):311–319, 2009.

[96] C. Fortmann, H. J. Lee, T. Döppner, R. W. Falcone, A. L. Kritcher, O. L. Landen, and S. H. Glenzer. Measurement of the adiabatic index in be compressed by counterpropagating shocks. *Phys. Rev. Lett.*, 108:175006, Apr 2012.

[97] Carsten Fortmann, August Wierling, and Gerd Röpke. Influence of local-field corrections on thomson scattering in collision-dominated two-component plasmas. *Physical Review E*, 81:026405, February 2010.

[98] J.C. Fuggle and J.E. Inglesfield, editors. *Unoccupied Electronic States*. Springer, 1992.

[99] E. Garcia Saiz, G. Gregori, D. O. Gericke, J. Vorberger, B. Barbrel, R. J. Clarke, R. R. Freeman, S. H. Glenzer, F. Y. Khattak, M. Koenig, O. L. Landen, D. Neely, P. Neumayer, M. M. Notley, A. Pelka, D. Price, M. Roth, M. Schollmeier, C. Spindloe, R. L. Weber, L. van Woerkom, K. Wunsch, and D. Riley. Probing warm dense lithium by inelastic x-ray scattering. *Nat Phys*, 4(12):940–944, December 2008.

[100] P. Glatzel and U. Bergmann. High resolution 1s core hole x-ray spectroscopy in 3d transition metal complexeselectronic and structural information. *Coordination Chemistry Reviews*, 249(1-2):65, 2005.

[101] P Glatzel, FMF de Groot, O Manoilova, D Grandjean, BM Weckhuysen, U Bergmann, and R Barrea. Range-extended EXAFS at the L edge of rare earths using high-energy-resolution fluorescence detection: A study of La in LaOCl. *Physical Review B*, 72:014117, 2005.

[102] S. H. Glenzer, G. Gregori, R. W. Lee, F. J. Rogers, S. W. Pollaine, and O. L. Landen. Demonstration of spectrally resolved X-Ray scattering in dense plasmas. *Physical Review Letters*, 90:175002, May 2003.

[103] S. H. Glenzer, G. Gregori, F. J. Rogers, D. H. Froula, S. W. Pollaine, R. S. Wallace, and O. L. Landen. X-ray scattering from solid density plasmas. *Physics of Plasmas*, 10(6):2433–2441, 2003.

[104] S. H. Glenzer, O. L. Landen, P. Neumayer, R. W. Lee, K. Widmann, S. W. Pollaine, R. J. Wallace, G. Gregori, A. Höll, T. Bornath, R. Thiele, V. Schwarz, W. D. Kraeft,

and R. Redmer. Observations of plasmons in warm dense matter. *Phys. Rev. Lett.*, 98(6):065002, February 2007.

[105] S. H. Glenzer, H. J. Lee, P. Davis, T. Döppner, R. W. Falcone, C. Fortmann, B. A. Hammel, A. L. Kritcher, O. L. Landen, and R. W. Lee. Dense plasma x-ray scattering: Methods and applications. *High Energy Density Physics*, 6(1):1–8, January 2010.

[106] S.H. Glenzer, H.J. Lee, P. Davis, T. Dppner, R.W. Falcone, C. Fortmann, B.A. Hammel, A.L. Kritcher, O.L. Landen, R.W. Lee, D.H. Munro, R. Redmer, and S. Weber. Dense plasma x-ray scattering: Methods and applications. *High Energy Density Physics*, 6(1):1 – 8, 2010.

[107] Siegfried H. Glenzer and Ronald Redmer. X-ray thomson scattering in high energy density plasmas. *Reviews of Modern Physics*, 81(4):1625–1663, 2009.

[108] Siegfried H. Glenzer and Ronald Redmer. X-ray thomson scattering in high energy density plasmas. *Reviews of Modern Physics*, 81(4):1625–1663, December 2009.

[109] R. Gordon, T. K. Sham, B. A. Mattern, G. T. Seidler, M. C. Stennett, D. P. Reid, and N. C. Hyatt. Hard x-ray RIXS and NIXS of ionic cerium compounds. Submitted to Physical Review B, 2011.

[110] R. A. Gordon, G. T. Seidler, T. T. Fister, M. W. Haverkort, G. A. Sawatzky, A. Tanaka, and T. K. Sham. High multipole transitions in nixs: Valence and hybridization in 4f systems. *EPL (Europhysics Letters)*, 81(2):26004, Jan 2008.

[111] R. A. Gordon, G. T. Seidler, T. T. Fister, and K. P. Nagle. Studying low-energy corevalence transitions with bulk sensitivity using q-dependent NIXS. *Journal of Electron Spectroscopy and Related Phenomena*, 184(3-6):220–223, April 2011.

[112] G. Gregori, S. H. Glenzer, K. B. Fournier, K. M. Campbell, E. L. Dewald, O. S. Jones, J. H. Hammer, S. B. Hansen, R. J. Wallace, and O. L. Landen. X-ray scattering measurements of radiative heating and cooling dynamics. *Phys. Rev. Lett.*, 101:045003, Jul 2008.

[113] G. Gregori, S. H. Glenzer, and O. L. Landen. Generalized x-ray scattering cross section from nonequilibrium plasmas. *Phys. Rev. E*, 74:026402, Aug 2006.

[114] G. Gregori, S. H. Glenzer, F. J. Rogers, S. M. Pollaine, O. L. Landen, C. Blancard, G. Faussurier, P. Renaudin, S. Kuhlbrodt, and R. Redmer. Electronic structure measurements of dense plasmas. *Physics of Plasmas*, 11(5):2754–2762, 2004.

[115] G. Gregori, S. H. Glenzer, W. Rozmus, R. W. Lee, and O. L. Landen. Theoretical model of x-ray scattering as a dense matter probe. *Phys. Rev. E*, 67:026412, Feb 2003.

[116] G. Gregori, A. Ravasio, A. Höll, S.H. Glenzer, and S.J. Rose. Derivation of the static structure factor in strongly coupled non-equilibrium plasmas for x-ray scattering studies. *High Energy Density Physics*, 3(1-2):99 – 108, 2007.

[117] Hu Guangyue, Zhang Xiaoding, Zheng Jian, Lei Anle, Shen Baifei, Xu Zhizhan, Zhang Jiyan, Yang Jiamin, Yang Guohong, Wei Minxi, Li Jun, and Ding Yongkun. Demonstration of x-ray thomson scattering on shenguang-ii laser facility. *Plasma Science and Technology*, 14(10):864, 2012.

[118] Subhra S. Gupta, J. A. Bradley, M. W. Haverkort, G. T. Seidler, A. Tanaka, and G. A. Sawatzky. Coexistence of bound and virtual-bound states in shallow-core to valence x-ray spectroscopies. *Physical Review B*, 84:075134, August 2011.

[119] Y. M. Gupta and X. A. Shen. Potential use of the ruby r[sub 2] line shift for static high-pressure calibration. *Applied Physics Letters*, 58(6):583–585, 1991.

[120] S. W. Haan, J. Atherton, D. S. Clark, B. A. Hammel, D. A. Callahan, C. J. Cerjan, E. L. Dewald, S. Dixit, M. J. Edwards, S. Glenzer, S. P. Hatchett, D. Hicks, O. S. Jones, O. L. Landen, J. D. Lindl, M. M. Marinak, B. J. MacGowan, A. J. MacKinnon, N. B. Meezan, J. L. Milovich, D. H. Munro, H. F. Robey, J. D. Salmonson, B. K. Spears, L. J. Suter, R. P. Town, S. V. Weber, J. L. Kline, and D. C. Wilson. Nif ignition campaign target performance and requirements: Status may 2012. *Fusion Science and Technology*, 63(2):67–75, MAR-APR 2013.

[121] M. Hakala, S. Huotari, K. Hämäläinen, S. Manninen, Ph. Wernet, A. Nilsson, and L. G. M. Pettersson. Compton profiles for water and mixed water-neon clusters: A measure of coordination. *Phys. Rev. B*, 70:125413, Sep 2004.

[122] M. Hakala, K. Nygaard, S. Manninen, S. Huotari, T. Buslaps, A. Nilsson, L. G. M. Pettersson, and K. Hämäläinen. Correlation of hydrogen bond lengths and angles in liquid water based on compton scattering. *The Journal of Chemical Physics*, 125(8):084504, 2006.

[123] M. Hakala, K. Nygaard, J. Vaara, M. Itou, Y. Sakurai, and K. Hämäläinen. Charge localization in alcohol isomers studied by compton scattering. *The Journal of Chemical Physics*, 130(3):034506, 2009.

[124] K. Hämäläinen, S. Galambosi, J. A. Soininen, Eric L. Shirley, J. P. Rueff, and A. Shukla. Momentum dependence of fluorine K -edge core exciton in lif. *Physical Review B*, 65:155111, March 2002.

[125] K. Hamalainen, M. Krisch, C. C. Kao, W. Caliebe, and J. B. Hastings. *Review of Scientific Instruments*, 66(2):1525, 1995.

[126] S. P. Hau-Riege, A. Graf, T. Döppner, R. A. London, J. Krzywinski, C. Fortmann, S. H. Glenzer, M. Frank, K. Sokolowski-Tinten, M. Messerschmidt, C. Bostedt, S. Schorb, J. A. Bradley, A. Lutman, D. Rolles, A. Rudenko, and B. Rudek. Ultrafast transitions from solid to liquid and plasma states of graphite induced by x-ray free-electron laser pulses. *Phys. Rev. Lett.*, 108:217402, May 2012.

[127] M. W. Haverkort, A. Tanaka, L. H. Tjeng, and G. A. Sawatzky. Nonresonant inelastic X-Ray scattering involving excitonic excitations: The examples of NiO and CoO. *Physical Review Letters*, 99(25):257401, December 2007.

[128] S. Hayakawa, Y. Kagoshima, Y. Tsusaka, J. Matsui, and T. Hirokawa. *Journal of Trace and Microprobe Techniques*, 19(4):615, 2001.

[129] S. Hayakawa, A. Yamaguchi, W. Hong, Y. Gohshi, T. Yamamoto, K. Hayashi,

J. Kawai, and S. Goto. *Spectrochimica Acta Part B-Atomic Spectroscopy*, 54(1):171, 1999.

[130] H. Hayashi, M. Kawata, R. Takeda, Y. Udagawa, Y. Watanabe, T. Takano, S. Nanao, and N. Kawamura. *Journal of Electron Spectroscopy and Related Phenomena*, 136:191, 2004.

[131] K. Hayashi, K. Nakajima, K. Fujiwara, and S. Nishikata. Wave-dispersive x-ray spectrometer for simultaneous acquisition of several characteristic lines based on strongly and accurately shaped ge crystal. *Review of Scientific Instruments*, 79(3):033110, 2008.

[132] Jean-Louis Hazemann, Olivier Proux, Vivian Nassif, Herve Palancher, Eric Lahera, Cecile Da Silva, Aurelien Braillard, Denis Testemale, Marie-Ange Diot, Isabelle Alliot, William Del Net, Alain Manceau, Frederic Gelebart, Marc Morand, Quentin Dermigny, and Abhay Shukla. High-resolution spectroscopy on an x-ray absorption beamline. *Journal of Synchrotron Radiation*, 16:283–292, 2009.

[133] S.M. Heald, J.O. Cross, D.L. Brewe, and R.A. Gordon. *Nucl. Instrum. Methods A*, 582(1):215, 2007.

[134] Conyers Herring. A new method for calculating wave functions in crystals. *Phys. Rev.*, 57:1169–1177, Jun 1940.

[135] D. J. Hoarty, P. Allan, S. F. James, C. R. D. Brown, L. M. R. Hobbs, M. P. Hill, J. W. O. Harris, J. Morton, M. G. Brookes, R. Shepherd, J. Dunn, H. Chen, E. Von Marley, P. Beiersdorfer, H. K. Chung, R. W. Lee, G. Brown, and J. Emig. Observations of the effect of ionization-potential depression in hot dense plasma. *Phys. Rev. Lett.*, 110:265003, Jun 2013.

[136] A. Höll, R. Redmer, G. Röpke, and H. Reinholz. X-ray thomson scattering in warm dense matter. *The European Physical Journal D - Atomic, Molecular, Optical and Plasma Physics*, 29(2):159–162, May 2004.

[137] J. Hoszowska, J.-Cl. Dousse, J. Kern, and Ch. Rheme. High resolution von hamos crystal x-ray spectrometer. *Nuclear Instruments & Methods in Physics Research Section a-Accelerators Spectrometers Detectors and Associated Equipment*, 376(1):129, 1996.

[138] J. Hoszowska, J.-Cl. Dousse, J. Szlachetko, Y. Kayser, W. Cao, P. Jagodziński, M. Kavčič, and S. H. Nowak. First observation of two-electron one-photon transitions in single-photon k-shell double ionization. *Phys. Rev. Lett.*, 107:053001, 2011.

[139] J. Hoszowska, A. K. Kheifets, J.-Cl. Dousse, M. Berset, I. Bray, W. Cao, K. Fennane, Y. Kayser, M. Kavčič, J. Szlachetko, and M. Szlachetko. Physical mechanisms and scaling laws of k-shell double photoionization. *Phys. Rev. Lett.*, 102:073006, 2009.

[140] S. Huotari, F. Albergamo, G. Vanko, R. Verbeni, and G. Monaco. Resonant inelastic hard x-ray scattering with diced analyzer crystals and position-sensitive detectors. *Review of Scientific Instruments*, 77(5):053102, 2006.

[141] S. Huotari, K. Hämäläinen, S. Manninen, S. Kaprzyk, A. Bansil, W. Caliebe, T. Buslaps, V. Honkimäki, and P. Suortti. Energy dependence of experimental be compton profiles. *Physical Review B*, 62:7956–7963, September 2000.

[142] S. Huotari, K. Hämäläinen, S. Manninen, S. Kaprzyk, A. Bansil, W. Caliebe, T. Buslaps, V. Honkimäki, and P. Suortti. Energy dependence of experimental be compton profiles. *Physical Review B*, 62:7956–7963, 2000.

[143] S. Huotari, K. Hämäläinen, S. Manninen, C. Sternemann, A. Kaprolat, W. Schülke, and T. Buslaps. High-momentum components and temperature dependence of the compton profile of beryllium. *Physical Review B*, 66:085104, August 2002.

[144] S. Huotari, C. Sternemann, M. Volmer, J. A. Soininen, G. Monaco, and W. Schülke. High-resolution compton line shapes: Fermi break of beryllium. *Phys. Rev. B*, 76:235106, Dec 2007.

[145] S. Huotari, G. Vanko, F. Albergamo, C. Ponchut, H. Graafsma, C. Henriquet, R. Verbeni, and G. Monaco. Improving the performance of high-resolution x-ray spectrome-

ters with position-sensitive pixel detectors. *Journal of Synchrotron Radiation*, 12:467, 2005.

[146] Simo Huotari, Barbara Boldrini, Veijo Honkimäki, Pekka Suortti, and Wolf Weyrich. Directional lithium hydride compton profiles of 0.1% statistical accuracy. *Journal of Synchrotron Radiation*, 16(5):672–682, Sep 2009.

[147] Simo Huotari, Tuomas Pylkk"anen, Roberto Verbeni, Giulio Monaco, and Keijo H"am"al"ainen. Direct tomography with chemical-bond contrast. *Nature Materials*, 10:489–493, 2011.

[148] Simo Huotari, Tuomas Pylkkanen, Roberto Verbeni, Giulio Monaco, and Keijo Hamalainen. Direct tomography with chemical-bond contrast. *Nature Materials*, 10(7):489, 2011.

[149] Simo Huotari, J. Aleksi Soininen, Tuomas Pylkkänen, Keijo Hämäläinen, Arezki Issolah, Andrey Titov, Jeremy McMinis, Jeongnim Kim, Ken Esler, David M. Ceperley, Markus Holzmann, and Valerio Olevano. Momentum distribution and renormalization factor in sodium and the electron gas. *Physical Review Letters*, 105(8):086403, Aug 2010.

[150] G. Huser, M. Koenig, A. Benuzzi-Mounaix, E. Henry, T. Vinci, B. Faral, M. Tomasini, B. Telaro, and D. Batani. Temperature and melting of laser-shocked iron releasing into an lif window. *Physics of Plasmas*, 12(6):060701, 2005.

[151] Mitio Inokuti, Yukikazu Itikawa, and James E. Turner. Addenda: Inelastic collisions of fast charged particles with atoms and molecules¯the bethe theory revisited. *Rev. Mod. Phys.*, 50:23–35, Jan 1978.

[152] M. Itou, Y. Sakurai, T. Ohata, A. Bansil, S. Kaprzyk, Y. Tanaka, H. Kawata, and N. Shiotani. Fermi surface signatures in the compton profile of be. *Journal of Physics and Chemistry of Solids*, 59(1):99 – 103, 1998.

[153] J. D. Jackson. *Classical Electrodynamics*. Wiley, 1998.

[154] R. W. James. *Optical Principles of the Diffraction of X-rays*. G. Bell and Sons, Ltd., London, 1962.

[155] G. E. M. Jauncey. Quantum theory of the unmodified spectrum line in the compton effect. *Phys. Rev.*, 25:314–321, Mar 1925.

[156] H.H. Johann. *Zeitschrift fur Physik*, 69:185, 1931.

[157] T. Johannson. *Zeitschrift fur Physik*, 82:507, 1933.

[158] W. R. Johnson, J. Nilsen, and K. T. Cheng. Thomson scattering in the average-atom approximation. *Phys. Rev. E*, 86:036410, Sep 2012.

[159] C. M. Johnston, P. Piela, and P. Zelenay. *Handbook of Fuel Cells Fundamentals, Technology and Applications*, volume 5, chapter 4. John Wiley & Sons, Ltd., 2009.

[160] I. Juurinen, K. Nakahara, N. Ando, T. Nishiumi, H. Seta, N. Yoshida, T. Morinaga, M. Itou, T. Ninomiya, Y. Sakurai, E. Salonen, K. Nordlund, K. Hämäläinen, and M. Hakala. Measurement of two solvation regimes in Water-Ethanol mixtures using X-Ray compton scattering. *Physical Review Letters*, 107:197401, October 2011.

[161] Valentin V. Karasiev, Travis Sjostrom, and S. B. Trickey. Comparison of density functional approximations and the finite-temperature hartree-fock approximation in warm dense lithium. *Phys. Rev. E*, 86:056704, Nov 2012.

[162] Valentin V. Karasiev, Travis Sjostrom, and S. B. Trickey. Generalized-gradient-approximation noninteracting free-energy functionals for orbital-free density functional calculations. *Phys. Rev. B*, 86:115101, Sep 2012.

[163] J. J. Kas, J. J. Rehr, and L. Reining. *To be submitted Phys. Rev. Lett.*, 2013.

[164] Hyungjun Kim, Julius T. Su, and William A. Goddard. High-temperature high-pressure phases of lithium from electron force field (eff) quantum electron dynamics simulations. *Proceedings of the National Academy of Sciences*, 108(37):15101–15105, 2011.

[165] Evgeny Kleymenov, Jeroen A. van Bokhoven, Christian David, Pieter Glatzel, Markus Janousch, Roberto Alonso-Mori, Marco Studer, Markus Willimann, Anna Bergamaschi, Beat Henrich, and Maarten Nachtegaal. Five-element johann-type x-ray emission spectrometer with a single-photon-counting pixel detector. *Review of Scientific Instruments*, 82:065107, 2011.

[166] Harold P. Klug and Leroy E. Alexander. *X-ray diffraction procedures for polycrystalline and amorphous materials*. Wiley, New York, 2d ed. edition, 1974.

[167] W. Kohn and N. Rostoker. Solution of the schrödinger equation in periodic lattices with an application to metallic lithium. *Physical Review*, 94(5):1111–1120, June 1954.

[168] W. Kohn and L. J. Sham. Self-consistent equations including exchange and correlation effects. *Phys. Rev.*, 140:A1133–A1138, Nov 1965.

[169] J. Korringa. On the calculation of the energy of a bloch wave in a metal. *Physica*, 13(6-7):392–400, August 1947.

[170] S. Kraft, J. Stümpel, P. Becker, and U. Kuetgens. High resolution x-ray absorption spectroscopy with absolute energy calibration for the determination of absorption edge energies. *Rev. Sci. Instrum.*, 67:681, 1996.

[171] M. H. Krisch, F. Sette, C. Masciovecchio, and R. Verbeni. Momentum transfer dependence of inelastic x-ray scattering from the li K edge. *Physical Review Letters*, 78:2843–2846, April 1997.

[172] A. Kritcher. Private Communication.

[173] A. L. Kritcher, T. Döppner, C. Fortmann, T. Ma, O. L. Landen, R. Wallace, and S. H. Glenzer. In-flight measurements of capsule shell adiabats in laser-driven implosions. *Phys. Rev. Lett.*, 107:015002, Jul 2011.

[174] A. L. Kritcher, P. Neumayer, C. R. D. Brown, P. Davis, T. Döppner, R. W. Falcone, D. O. Gericke, G. Gregori, B. Holst, O. L. Landen, H. J. Lee, E. C. Morse, A. Pelka, R. Redmer, M. Roth, J. Vorberger, K. Wünsch, and S. H. Glenzer. Measurements

of ionic structure in shock compressed lithium hydride from ultrafast x-ray thomson scattering. *Phys. Rev. Lett.*, 103:245004, Dec 2009.

[175] A.L. Kritcher, T. Döppner, C. Fortmann, O.L. Landen, R. Wallace, and S.H. Glenzer. Development of x-ray thomson scattering for implosion target characterization. *High Energy Density Physics*, 7(4):271 – 276, 2011.

[176] Andrea L. Kritcher, Paul Neumayer, John Castor, Tilo Döppner, Roger W. Falcone, Otto L. Landen, Hae J. Lee, Richard W. Lee, Edward C. Morse, Andrew Ng, Steve Pollaine, Dwight Price, and Siegfried H. Glenzer. Ultrafast x-ray thomson scattering of Shock-Compressed matter. *Science*, 322(5898):69–71, October 2008.

[177] Andrea L. Kritcher, Paul Neumayer, John Castor, Tilo Dppner, Roger W. Falcone, Otto L. Landen, Hae Ja Lee, Richard W. Lee, Edward C. Morse, Andrew Ng, Steve Pollaine, Dwight Price, and Siegfried H. Glenzer. Ultrafast x-ray thomson scattering of shock-compressed matter. *Science*, 322(5898):69–71, 2008.

[178] R Kubo. The fluctuation-dissipation theorem. *Reports on Progress in Physics*, 29(1):255, 1966.

[179] L. Lam and P. M. Platzman. Momentum density and compton profile of the inhomogeneous interacting electronic system. i. formalism. *Physical Review B*, 9:5122–5127, June 1974.

[180] L. D. Landau and E.M. Lifshitz. *Statistical Physics I.* Course of theoretical physics. Elsevier, Amsterdam, 1980. p. 168.

[181] H. J. Lee, P. Neumayer, J. Castor, T. Döppner, R. W. Falcone, C. Fortmann, B. A. Hammel, A. L. Kritcher, O. L. Landen, R. W. Lee, D. D. Meyerhofer, D. H. Munro, R. Redmer, S. P. Regan, S. Weber, and S. H. Glenzer. X-Ray Thomson-Scattering measurements of density and temperature in Shock-Compressed beryllium. *Phys. Rev. Lett.*, 102(11):115001, 2009.

[182] H. J. Lee, P. Neumayer, J. Castor, T. Döppner, R. W. Falcone, C. Fortmann, B. A. Hammel, A. L. Kritcher, O. L. Landen, R. W. Lee, D. D. Meyerhofer, D. H. Munro,

R. Redmer, S. P. Regan, S. Weber, and S. H. Glenzer. X-Ray Thomson-Scattering measurements of density and temperature in Shock-Compressed beryllium. *Phys. Rev. Lett.*, 102(11):115001, March 2009.

[183] Nicole Lee, Taras Petrenko, Uwe Bergmann, Frank Neese, and Serena DeBeer. Probing valence orbital composition with iron k x-ray emission spectroscopy. *Journal of the American Chemical Society*, 132(28):9715–9727, 2010.

[184] S. K. Lee, J.-F. Lin, Y. Q. Cai, N. Hiraoka, P. J. Eng, T. Okuchi, H.-k. Mao, Y. Meng, M. Y. Hu, P. Chow, Jinfu Shu, Baosheng Li, Hiroshi Fukui, Bum Han Lee, Hyun Na Kim, and Choong-Shik Yoo. X-ray raman scattering study of mgsio3 glass at high pressure: Implication for triclustered mgsio3 melt in earth's mantle. *Proceedings of the National Academy of Sciences*, 105(23):7925–7929, Jun 2008.

[185] A. Lévy, F. Dorchies, A. Benuzzi-Mounaix, A. Ravasio, F. Festa, V. Recoules, O. Peyrusse, N. Amadou, E. Brambrink, T. Hall, M. Koenig, and S. Mazevet. X-ray diagnosis of the pressure induced mott nonmetal-metal transition. *Phys. Rev. Lett.*, 108:055002, Jan 2012.

[186] JF Lin, VV Struzhkin, SD Jacobsen, MY Hu, P Chow, J Kung, HZ Liu, HK Mao, and RJ Hemley. Spin transition of iron in magnesiowustite in the earth's lower mantle. *Nature*, 436(7049):377–380, 2005.

[187] Jung-Fu Lin, Heather Watson, Gyoergy Vanko, Esen E. Alp, Vitali B. Prakapenka, Przemek Dera, Viktor V. Struzhkin, Atsushi Kubo, Jiyong Zhao, Catherine McCammon, and William J. Evans. Intermediate-spin ferrous iron in lowermost mantle post-perovskite and perovskite. *Nature Geoscience*, 1(10):688–691, 2008.

[188] John D. Lindl, Peter Amendt, Richard L. Berger, S. Gail Glendinning, Siegfried H. Glenzer, Steven W. Haan, Robert L. Kauffman, Otto L. Landen, and Laurence J. Suter. The physics basis for ignition using indirect-drive targets on the national ignition facility. *Physics of Plasmas*, 11(2):339–491, 2004.

[189] Pascal Link, Pieter Glatzel, Kristina Kvashnina, Ronald I. Smith, and Uwe Ruschewitzt. Yb Valence States in YbC(2): A HERFD-XANES Spectroscopic Investigation. *Inorganic Chemistry*, 50:5587, 2011.

[190] T. Ma, T. Döppner, R. W. Falcone, L. Fletcher, C. Fortmann, D. O. Gericke, O. L. Landen, H. J. Lee, A. Pak, J. Vorberger, K. Wünsch, and S. H. Glenzer. X-ray scattering measurements of strong ion-ion correlations in shock-compressed aluminum. *Phys. Rev. Lett.*, 110:065001, Feb 2013.

[191] J.J. MacFarlane, I.E. Golovkin, and P.R. Woodruff. Helios-cr a 1-d radiation-magnetohydrodynamics code with inline atomic kinetics modeling. *Journal of Quantitative Spectroscopy and Radiative Transfer*, 99(13):381 – 397, 2006.

[192] B. A. Mattern. *Compton Scattering and Warm Dense Matter Thermometry*. PhD thesis, University of Washington, Seattle, 2013.

[193] Brian A. Mattern and Gerald T. Seidler. Theoretical treatments of the bound-free contribution and experimental best practice in x-ray thomson scattering from warm dense matter. *Physics of Plasmas*, 20(2):022706, 2013.

[194] Brian A. Mattern, Gerald T. Seidler, Joshua J. Kas, Joseph I. Pacold, and John J. Rehr. Real-space green's function calculations of compton profiles. *Physical Review B*, 85:115135, 2012.

[195] N. D. Mermin. Lindhard dielectric function in the relaxation-time approximation. *Phys. Rev. B*, 1:2362–2363, Mar 1970.

[196] T. Missalla, I. Uschmann, E. Forster, G. Jenke, and D. von der Linde. Monochromatic focusing of subpicosecond x-ray pulses in the kev range. *Review of Scientific Instruments*, 70(2):1288–1299, 1999.

[197] E. I. Moses, R. N. Boyd, B. A. Remington, C. J. Keane, and R. Al-Ayat. The national ignition facility: Ushering in a new age for high energy density science. *Physics of Plasmas*, 16(4):041006, 2009.

[198] E. I. Moses, R. N. Boyd, B. A. Remington, C. J. Keane, and R. Al Ayat. The national ignition facility: Ushering in a new age for high energy density science. *Physics of Plasmas*, 16(4):041006, 2009.

[199] N. F. MOTT. Metal-insulator transition. *Rev. Mod. Phys.*, 40:677–683, Oct 1968.

[200] Bob Nagler, Ulf Zastrau, Roland R. Faeustlin, Sam M. Vinko, Thomas Whitcher, A. J. Nelson, Ryszard Sobierajski, Jacek Krzywinski, Jaromir Chalupsky, Elsa Abreu, Sasa Bajt, Thomas Bornath, Tomas Burian, Henry Chapman, Jaroslav Cihelka, Tilo Doeppner, Stefan Duesterer, Thomas Dzelzainis, Marta Fajardo, Eckhart Foerster, Carsten Fortmann, Eric Galtier, Siegfried H. Glenzer, Sebastian Goede, Gianluca Gregori, Vera Hajkova, Phil Heimann, Libor Juha, Marek Jurek, Fida Y. Khattak, Ali Reza Khorsand, Dorota Klinger, Michaela Kozlova, Tim Laarmann, Hae Ja Lee, Richard W. Lee, Karl-Heinz Meiwes-Broer, Pascal Mercere, William J. Murphy, Andreas Przystawik, Ronald Redmer, Heidi Reinholz, David Riley, Gerd Roepke, Frank Rosmej, Karel Saksl, Romain Schott, Robert Thiele, Josef Tiggesbaeumker, Sven Toleikis, Thomas Tschentscher, Ingo Uschmann, Hubert J. Vollmer, and Justin S. Wark. Turning solid aluminium transparent by intense soft x-ray photoionization. *Nature Physics*, 5(9):693–696, Jul 2009.

[201] Bob Nagler, Ulf Zastrau, Roland R. Fäustlin, Sam M. Vinko, Thomas Whitcher, A. J. Nelson, Ryszard Sobierajski, Jacek Krzywinski, Jaromir Chalupsky, Elsa Abreu, Saa Bajt, Thomas Bornath, Tomas Burian, Henry Chapman, Jaroslav Cihelka, Tilo Döppner, Stefan Düsterer, Thomas Dzelzainis, Marta Fajardo, Eckhart Förster, Carsten Fortmann, Eric Galtier, Siegfried H. Glenzer, Sebastian Göde, Gianluca Gregori, Vera Hajkova, Phil Heimann, Libor Juha, Marek Jurek, Fida Y. Khattak, Ali R. Khorsand, Dorota Klinger, Michaela Kozlova, Tim Laarmann, Hae J. Lee, Richard W. Lee, Karl-Heinz Meiwes-Broer, Pascal Mercere, William J. Murphy, Andreas Przystawik, Ronald Redmer, Heidi Reinholz, David Riley, Gerd Röpke, Frank Rosmej, Karel Saksl, Romain Schott, Robert Thiele, Josef Tiggesbäumker, Sven Toleikis, Thomas Tschentscher, Ingo Uschmann, Hubert J. Vollmer, and Justin S. Wark. Turning solid

aluminium transparent by intense soft x-ray photoionization. *Nat Phys*, 5(9):693–696, September 2009.

[202] J. B. Neaton and N. W. Ashcroft. Pairing in dense lithium. *Nature*, 400:141–144, 1999.

[203] J. B. Neaton and N. W. Ashcroft. On the constitution of sodium at higher densities. *Phys. Rev. Lett.*, 86:2830–2833, Mar 2001.

[204] P. M. Nilson, A. A. Solodov, J. F. Myatt, W. Theobald, P. A. Jaanimagi, L. Gao, C. Stoeckl, R. S. Craxton, J. A. Delettrez, B. Yaakobi, J. D. Zuegel, B. E. Kruschwitz, C. Dorrer, J. H. Kelly, K. U. Akli, P. K. Patel, A. J. Mackinnon, R. Betti, T. C. Sangster, and D. D. Meyerhofer. Scaling hot-electron generation to high-power, kilojoule-class laser-solid interactions. *Phys. Rev. Lett.*, 105:235001, Dec 2010.

[205] J. G. Norman. Untitled. *Molecular Physics*, 31:1191, 1976.

[206] M. M. Notley, R. L. Weber, B. Fell, J. Jeffries, R. R. Freeman, A. J. Mackinnon, R. Dickson, D. Hey, F. Khattak, E. G. Saiz, and G. Gregori. Development of time resolved x-ray spectroscopy in high intensity laser-plasma interactions. *Review of Scientific Instruments*, 77(10):10F322, 2006.

[207] K. Nygaard, M. Hakala, S. Manninen, M. Itou, Y. Sakurai, and K. Hämäläinen. Configurational energetics in ice I*h* probed by compton scattering. *Physical Review Letters*, 99:197401, November 2007.

[208] K. Nygaard, M. Hakala, T. Pylkkänen, S. Manninen, T. Buslaps, M. Itou, A. Andrejczuk, Y. Sakurai, M. Odelius, and K. Hämäläinen. Isotope quantum effects in the electron momentum density of water. *The Journal of Chemical Physics*, 126(15):154508, 2007.

[209] J. T. Okada, P. H.-L. Sit, Y. Watanabe, Y. J. Wang, B. Barbiellini, T. Ishikawa, M. Itou, Y. Sakurai, A. Bansil, R. Ishikawa, M. Hamaishi, T. Masaki, P.-F. Paradis, K. Kimura, T. Ishikawa, and S. Nanao. Persistence of covalent bonding in liquid

silicon probed by inelastic x-ray scattering. *Physical Review Letters*, 108(6):067402, Feb 2012.

[210] Committee on High Energy Density Plasma Physics. *Frontiers in High Energy Density Physics: The X-Games of Contemporary Science*. National Acadamies Press, Washington, DC, 2003.

[211] Committee on the Prospects for Inertial Confinement Fusion Energy Systems; National Research Council of the National Academies. *Interim Report-Status of the Study "An Assessment of the Prospects for Inertial Fusion Energy"*. The National Academies Press, 2012.

[212] J. I. Pacold. In preparation, 2011.

[213] J. I. Pacold, J. A. Bradley, B. A. Mattern, M. J. Lipp, G. T. Seidler, P. Chow, Y. Xiao, E. Rod, B. Rusthoven, and J. Quintana. A miniature x-ray emission spectrometer (miniXES) for high- pressure studies in a diamond anvil cell. In preparation, 2011.

[214] K.C. Pandey and L. Lam. Core-orthogonalization effect and the compton profile of sodium metal. *Physics Letters A*, 43(4):319 – 320, 1973.

[215] P. Pattison, N. K. Hansen, and J. R. Schneider. Anisotropy in the compton profile of copper. *Z. Phys. B - Condensed Matter*, 46:285–294, 1982.

[216] L. Pauling and J. Sherman. *Zeitschrift für Kirstallographie*, 1:81, 1932.

[217] A. Pelka, G. Gregori, D. O. Gericke, J. Vorberger, S. H. Glenzer, M. M. Günther, K. Harres, R. Heathcote, A. L. Kritcher, N. L. Kugland, B. Li, M. Makita, J. Mithen, D. Neely, C. Niemann, A. Otten, D. Riley, G. Schaumann, M. Schollmeier, An. Tauschwitz, and M. Roth. Ultrafast melting of carbon induced by intense proton beams. *Phys. Rev. Lett.*, 105:265701, Dec 2010.

[218] Fran çois Perrot and M. W. C. Dharma-wardana. Exchange and correlation potentials for electron-ion systems at finite temperatures. *Phys. Rev. A*, 30:2619–2626, Nov 1984.

[219] G. J. Piermarini, S. Block, J. D. Barnett, and R. A. Forman. Calibration of the pressure dependence of the r[sub 1] ruby fluorescence line to 195 kbar. *Journal of Applied Physics*, 46(6):2774–2780, 1975.

[220] K-U Plagemann, P Sperling, R Thiele, M P Desjarlais, C Fortmann, T Döppner, H J Lee, S H Glenzer, and R Redmer. Dynamic structure factor in warm dense beryllium. *New Journal of Physics*, 14(5):055020, 2012.

[221] Christopher J. Pollock and Serena DeBeer. Valence-to-core x-ray emission spectroscopy: A sensitive probe of the nature of a bound ligand. *Journal of the American Chemical Society*, 133(14):5594–5601, 2011.

[222] P. J. Potts, A. T. Ellis, P. Kregsamer, C. Streli, C. Vanhoof, M. West, and P. Wobrauschek. Atomic spectrometry update?x-ray fluorescence spectrometry. *Journal of Analytical Atomic Spectrometry*, 21(10):1076, 2006.

[223] M. Prange. *Density Matrix Calculation of Optical Constants*. PhD thesis, University of Washington, Seattle, 2009.

[224] M. P. Prange, J. J. Rehr, G. Rivas, J. J. Kas, and John W. Lawson. Real space calculation of optical constants from optical to x-ray frequencies. *Physical Review B*, 80:155110, October 2009.

[225] Tuomas Pylkkanen, Valentina M. Giordano, Jean-Claude Chervin, Arto Sakko, Mikko Hakala, J. Aleksi Soininen, Keijo Hamalainen, Giulio Monaco, and Simo Huotari. Role of non-hydrogen-bonded molecules in the oxygen k-edge spectrum of ice. *The Journal of Physical Chemistry B*, 114(11):3804–3808, 2010.

[226] Q. Qian, T.A. Tyson, W.A. Caliebe, and C.-C. Kao. High-efficiency high-energy-resolution spectrometer for inelastic x-ray scattering. *Journal of Physics and Chemistry of Solids*, 66(12):2295–2298, 2005.

[227] Deirdre D. Ragan, R. Gustavsen, and David Schiferl. Calibration of the ruby r[sub 1] and r[sub 2] fluorescence shifts as a function of temperature from 0 to 600 k. *Journal of Applied Physics*, 72(12):5539–5544, 1992.

[228] Bruce Ravel. Atoms software package, 2001.

[229] Bruce Ravel. Atoms on the web, 2005.

[230] R. Redmer and G. Röpke. Progress in the theory of dense strongly coupled plasmas. *Contrib. Plasma Phys.*, 50(10):970–985, 2010.

[231] R. Redmer and G. Röpke. Progress in the theory of dense strongly coupled plasmas. *Contributions to Plasma Physics*, 50(10):970–985, 2010.

[232] J. J. Rehr and R. C. Albers. Theoretical approaches to x-ray absorption fine structure. *Reviews of Modern Physics*, 72:621–654, July 2000.

[233] J. J. Rehr and R. C. Albers. Theoretical approaches to x-ray absorption fine structure. *Reviews of Modern Physics*, 72:621–654, July 2000.

[234] John J. Rehr, Joshua J. Kas, Micah P. Prange, Adam P. Sorini, Yoshinari Takimoto, and Fernando Vila. Ab initio theory and calculations of x-ray spectra. *Comptes Rendus Physique*, 10(6):548 – 559, 2009.

[235] Bruce A. Remington, R. Paul Drake, and Dmitri D. Ryutov. Experimental astrophysics with high power lasers and z pinches. *Reviews of Modern Physics*, 78:755–807, August 2006.

[236] Bruce A. Remington, R. Paul Drake, and Dmitri D. Ryutov. Experimental astrophysics with high power lasers and z pinches. *Rev. Mod. Phys.*, 78:755–807, Aug 2006.

[237] P. Renaudin, C. Blancard, J. Clérouin, G. Faussurier, P. Noiret, and V. Recoules. Aluminum equation-of-state data in the warm dense matter regime. *Phys. Rev. Lett.*, 91:075002, Aug 2003.

[238] P. Rennert. Calculation of the compton profile of beryllium. *Phys. Stat. Sol. B*, 105:567, 1981.

[239] D. Riley, F. Y. Khattak, E. G. Saiz, G. Gregori, S. Bandyopadhyay, M. Notley, D. Neely, D. Chambers, A. Moore, and A. Comley. Spectrally resolved x-ray scatter from laser-shock-driven plasmas. *Laser and Particle Beams*, 25(3):465, 2007.

[240] D. Riley, F.Y. Khattak, E. Garcia Saiz, G. Gregori, S. Bandyopadhyay, M. Notley, D. Neely, D. Chambers, A. Moore, and A. Comley. Spectrally resolved x-ray scatter from laser-shock-driven plasmas. *Laser and Particle Beams*, 25(03):465–469, 2007.

[241] Bruno Rousseau and N. W. Ashcroft. Interstitial electronic localization. *Phys. Rev. Lett.*, 101:046407, Jul 2008.

[242] J.-P. Rueff, C.-C. Kao, V. V. Struzhkin, J. Badro, J. Shu, R. J. Hemley, and H. K. Mao. Pressure-induced high-spin to low-spin transition in fes evidenced by x-ray emission spectroscopy. *Physical Review Letters*, 82:3284, 1999.

[243] S. Sahoo, G. F. Gribakin, G. Shabbir Naz, J. Kohanoff, and D. Riley. Compton scatter profiles for warm dense matter. *Phys. Rev. E*, 77:046402, Apr 2008.

[244] A. Sakko, C. Sternemann, Ch. J. Sahle, H. Sternemann, O. M. Feroughi, H. Conrad, F. Djurabekova, A. Hohl, G. T. Seidler, M. Tolan, and K. Hämäläinen. Suboxide interface in disproportionating a -sio studied by x-ray raman scattering. *Physical Review B*, 81(20):205317, May 2010.

[245] Y. Sakurai. A high-resolution compton scattering study of cu: experiment and theory. *Journal of Physics and Chemistry of Solids*, 60(7):905–910, July 1999.

[246] Y. Sakurai, M. Ito, T. Urai, Y. Tanaka, N. Sakai, T. Iwazumi, H. Kawata, M. Ando, and N. Shiotani. An x-ray spectrometer for compton scattering. *Review of Scientific Instruments*, 63(1):1190–1193, 1992.

[247] Y. Sakurai, M. Itou, B. Barbiellini, P. E. Mijnarends, R. S. Markiewicz, S. Kaprzyk, J. M. Gillet, S. Wakimoto, M. Fujita, S. Basak, Yung J. Wang, W. Al-Sawai, H. Lin, A. Bansil, and K. Yamada. Imaging doped holes in a cuprate superconductor with High-Resolution compton scattering. *Science*, 332(6030):698–702, May 2011.

[248] Y. Sakurai, M. Itou, B. Barbiellini, P. E. Mijnarends, R. S. Markiewicz, S. Kaprzyk, J.-M. Gillet, S. Wakimoto, M. Fujita, S. Basak, Yung Jui Wang, W. Al-Sawai, H. Lin, A. Bansil, and K. Yamada. Imaging doped holes in a cuprate superconductor with high-resolution compton scattering. *Science*, 332(6030):698–702, May 2011.

[249] H. Sawada, S. P. Regan, D. D. Meyerhofer, I. V. Igumenshchev, V. N. Goncharov, T. R. Boehly, R. Epstein, T. C. Sangster, V. A. Smalyuk, B. Yaakobi, G. Gregori, S. H. Glenzer, and O. L. Landen. Diagnosing direct-drive, shock-heated, and compressed plastic planar foils with noncollective spectrally resolved x-ray scattering. *Physics of Plasmas*, 14(12):122703, 2007.

[250] Winfried Schűlke. *Electron Dynamics by Inelastic X-Ray Scattering*. Oxford Series on Synchrotron Radiation. Oxford University Press, New York, 2007.

[251] Winfried Schülke. *Electron Dynamics by Inelastic X-Ray Scattering*. Oxford Series on Synchrotron Radiation. Oxford University Press, New York, 2007.

[252] M Schumacher, F Smend, and I Borchert. Incoherent scattering of gamma rays by inner-shell electrons. *Journal of Physics B: Atomic and Molecular Physics*, 8(9):1428, 1975.

[253] Volker Schwarz, Bastian Holst, Thomas Bornath, Carsten Fortmann, Wolf-Dietrich Kraeft, Robert Thiele, Ronald Redmer, Gianluca Gregori, Hae Ja Lee, Tilo Döppner, and Siegfried H. Glenzer. Static ion structure factor for dense plasmas: Semi-classical and ab initio calculations. *High Energy Density Physics*, 6(3):305 – 310, 2010.

[254] G. T. Seidler, M. Haave, J. I. Pacold, R. A. Gordon, and S M Heald. *In prep.* Review of Scientific Instruments (2012).

[255] A. Selchow, G. Röpke, A. Wierling, H. Reinholz, T. Pschiwul, and G. Zwicknagel. Dynamic structure factor for a two-component model plasma. *Phys. Rev. E*, 64:056410, Oct 2001.

[256] A Sengebusch, H Reinholz, G Röpke, U Zastrau, T Kämpfer, I Uschmann, E Förster, E Stambulchik, E Kroupp, and Y Maron. K-line emission profiles with focus on the

self-consistent calculation of plasma polarization. *Journal of Physics A: Mathematical and Theoretical*, 42(21):214061, May 2009.

[257] John Sheffield, Dustin Froula, Siegfried H. Glenzer, and Neville C. Luhmann Jr. *Plasma Scattering of Electromagnetic Radiation, Second Edition: Theory and Measurement Techniques*. Academic Press, 2010.

[258] R. Shepherd, P. Audebert, R. Booth, B. Young, J. Bonlie, D. Nelson, S. Shiromizu, D. Price, D. Norman, J. Dunn, K. Widmann, and P. Springer. Time resolved spectroscopy of ultrashort pulse laser generated x rays using von hamos crystal spectroscopy. *Review of Scientific Instruments*, 75(10):3765, 2004.

[259] A. P. Shevelko, Y. S. Kasyanov, O. F. Yakushev, and L. V. Knight. Compact focusing von hamos spectrometer for quantitative x-ray spectroscopy. *Review of Scientific Instruments*, 73(10):3458, 2002.

[260] Y. Shvyd'ko. *X-Ray Optics: High-Energy-Resolution Applications*. Springer, 2004.

[261] Travis Sjostrom, Frank E. Harris, and S. B. Trickey. Temperature-dependent behavior of confined many-electron systems in the hartree-fock approximation. *Phys. Rev. B*, 85:045125, Jan 2012.

[262] Travis Sjostrom, Frank E. Harris, and S. B. Trickey. Temperature-dependent behavior of confined many-electron systems in the hartree-fock approximation. *Phys. Rev. B*, 85:045125, Jan 2012.

[263] J. A. Soininen, A. L. Ankudinov, and J. J. Rehr. Inelastic scattering from core electrons: A multiple scattering approach. *Physical Review B*, 72:045136, July 2005.

[264] J. A. Soininen, K. Hämäläinen, W. A. Caliebe, C. C. Kao, and Eric L. Shirley. Core-hole-electron interaction in x-ray raman scattering. *Journal of Physics: Condensed Matter*, 13(35):8039, September 2001.

[265] D. Sokaras, T.-C. Weng, D. Nordlund, R. Alonso-Mori, P. Velikov, D. Wenger, A. Garachtchenko, M. George, V. Borzenets, B. Johnson, T. Rabedeau, and

U. Bergmann. A seven-crystal johann-type hard x-ray spectrometer at the stanford synchrotron radiation lightsource. *Review of Scientific Instruments*, 84(5):053102, 2013.

[266] E Stambulchik, V Bernshtam, L Weingarten, E Kroupp, D Fisher, Y Maron, U Zastrau, I Uschmann, F Zamponi, E Förster, A. Sengebusch, H. Reinholz, G. Röpke, and Y. Ralchenko. Progress in line-shape modeling of k-shell transitions in warm dense titanium plasmas. *Journal of Physics A: Mathematical and Theoretical*, 42(21):214056, May 2009.

[267] S. A. Stepanov. Method of transfer matrices and dynamical thick-crystal approximation in surface x-ray diffraction by multilayer structures. *Crystallogr. Reports*, 39:182–187, 1994.

[268] C. Sternemann, T. Buslaps, A. Shukla, P. Suortti, G. Döring, and W. Schülke. Temperature influence on the valence compton profiles of aluminum and lithium. *Physical Review B*, 63:094301, January 2001.

[269] C. Sternemann, M. Volmer, J. A. Soininen, H. Nagasawa, M. Paulus, H. Enkisch, G. Schmidt, M. Tolan, and W. Schülke. Momentum-transfer dependence of x-ray raman scattering at the be k-edge. *Physical Review B*, 68:035111, July 2003.

[270] H. Sternemann, J. A. Soininen, C. Sternemann, K. Hämäläinen, and M. Tolan. Near-edge structure of nonresonant inelastic x-ray scattering from l-shell core levels studied by a real-space multiple-scattering approach. *Phys. Rev. B*, 75:075118, Feb 2007.

[271] H. Sternemann, C. Sternemann, G. T. Seidler, T. T. Fister, A. Sakko, and M. Tolan. An extraction algorithm for core-level excitations in non-resonant inelastic x-ray scattering spectra. *Journal of Synchrotron Radiation*, 15(2):162–169, Mar 2008.

[272] H. Sternemann, C. Sternemann, J. S. Tse, S. Desgreniers, Y. Q. Cai, G. Vankó, N. Hiraoka, A. Schacht, J. A. Soininen, and M. Tolan. Giant dipole resonance of ba in ba_8si_{46}: An approach for studying high-pressure induced phase transitions of nanostructured materials. *Phys. Rev. B*, 75:245102, Jun 2007.

[273] J. C. Stewart and K. D. Pyatt, Jr. Lowering of Ionization Potentials in Plasmas. *Astrophys. J.*, 144:1203, June 1966.

[274] P. Suortti, T. Buslaps, P. Fajardo, V. Honkimäki, M. Kretzschmer, U. Lienert, J. E. McCarthy, M. Renier, A. Shukla, Th, and T. Meinander. Scanning X-ray spectrometer for high-resolution Compton profile measurements at ESRF. *Journal of Synchrotron Radiation*, 6(2):69–80, March 1999.

[275] J. Szlachetko, J.-Cl. Dousse, J. Hoszowska, M. Pajek, R. Barrett, M. Berset, K. Fennane, A. Kubala-Kukus, and M. Szlachetko. High-resolution study of x-ray resonant raman scattering at the k edge of silicon. *Phys. Rev. Lett.*, 97:073001, 2006.

[276] K. Tiedtke, Ch. Gerth, M. Martins, and P. Zimmermann. *Physical Review A*, 64:022705, 2001.

[277] S. Toleikis, T. Bornath, T. Döppner, S. Düsterer, R. R. Fäustlin, E. Förster, C. Fortmann, S. H. Glenzer, S. Göde, G. Gregori, R. Irsig, T. Laarmann, H. J. Lee, B. Li, K. H. Meiwes-Broer, J. Mithen, B. Nagler, A. Przystawik, P. Radcliffe, H. Redlin, R. Redmer, H. Reinholz, G. Röpke, F. Tavella, R. Thiele, J. Tiggesbäumker, I. Uschmann, S. M. Vinko, T. Whitcher, U. Zastrau, B. Ziaja, and T. Tschentscher. Probing near-solid density plasmas using soft x-ray scattering. *Journal of Physics B: Atomic, Molecular and Optical Physics*, 43(19):194017, October 2010.

[278] S. Toleikis, R. R. Fäustlin, L. Cao, T. Döppner, S. Düsterer, E. Förster, C. Fortmann, S. H. Glenzer, S. Göde, and G. Gregori. Soft x-ray scattering using FEL radiation for probing near-solid density plasmas at few electron volt temperatures. *High Energy Density Physics*, 6(1):15–20, January 2010.

[279] I. Uschmann, E. Forster, H. Nishimura, K. Fujita, Y. Kato, and S. Nakai. Temperature mapping of compressed fusion pellets obtained by monochromatic imaging. *Review of Scientific Instruments*, 66(1):734–736, 1995.

[280] Gyorgy Vanko, Franz Renz, Gabor Molnar, Thomas Neisius, and Szilvia Karpati.

Hard-x-ray-induced excited-spin-state trapping. *Angewandte Chemie-International Edition*, 46(28):5306–5309, 2007.

[281] Roberto Verbeni, Tuomas Pylkkänen, Simo Huotari, Laura Simonelli, György Vankó, Keith Martel, Christian Henriquet, and Giulio Monaco. Multiple-element spectrometer for non-resonant inelastic X-ray spectroscopy of electronic excitations. *Journal of Synchrotron Radiation*, 16(4):469–476, July 2009.

[282] Roberto Verbeni, Tuomas Pylkkänen, Simo Huotari, Laura Simonelli, György Vankó, Keith Martel, Christian Henriquet, and Giulio Monaco. Multiple-element spectrometer for non-resonant inelastic x-ray spectroscopy of electronic excitations. *Journal of Synchrotron Radiation*, 16(4):469, 2009.

[283] Roberto Verbeni, Tuomas Pylkkänen, Simo Huotari, Laura Simonelli, György Vankó, Keith Martel, Christian Henriquet, and Giulio Monaco. Multiple-element spectrometer for non-resonant inelastic x-ray spectroscopy of electronic excitations. *Journal of Synchrotron Radiation*, 16(4):469, 2009.

[284] S. M. Vinko, O. Ciricosta, B. I. Cho, K. Engelhorn, H. K. Chung, C. R. D. Brown, T. Burian, J. Chalupsky, R. W. Falcone, C. Graves, V. Hajkova, A. Higginbotham, L. Juha, J. Krzywinski, H. J. Lee, M. Messerschmidt, C. D. Murphy, Y. Ping, A. Scherz, W. Schlotter, S. Toleikis, J. J. Turner, L. Vysin, T. Wang, B. Wu, U. Zastrau, D. Zhu, R. W. Lee, P. A. Heimann, B. Nagler, and J. S. Wark. Creation and diagnosis of a solid-density plasma with an x-ray free-electron laser. *Nature*, advance online publication:–, January 2012.

[285] S. M. Vinko, O. Ciricosta, B. I. Cho, K. Engelhorn, H-K Chung, C. R. D. Brown, T. Burian, J. Chalupsky, R. W. Falcone, C. Graves, V. Hajkova, A. Higginbotham, L. Juha, J. Krzywinski, H. J. Lee, M. Messerschmidt, C. D. Murphy, Y. Ping, A. Scherz, W. Schlotter, S. Toleikis, J. J. Turner, L. Vysin, T. Wang, B. Wu, U. Zastrau, D. Zhu, R. W. Lee, P. A. Heimann, B. Nagler, and J. S. Wark. Creation and diagnosis of a solid-density plasma with an x-ray free-electron laser. *Nature*, 482(7383):59–62, Jan 2012.

[286] S. M. Vinko, U. Zastrau, S. Mazevet, J. Andreasson, S. Bajt, T. Burian, J. Chalupsky, H. N. Chapman, J. Cihelka, D. Doria, T. Döppner, S. Düsterer, T. Dzelzainis, R. R. Fäustlin, C. Fortmann, E. Förster, E. Galtier, S. H. Glenzer, S. Göde, G. Gregori, J. Hajdu, V. Hajkova, P. A. Heimann, R. Irsig, L. Juha, M. Jurek, J. Krzywinski, T. Laarmann, H. J. Lee, R. W. Lee, B. Li, K. H. Meiwes Broer, J. P. Mithen, B. Nagler, A. J. Nelson, A. Przystawik, R. Redmer, D. Riley, F. Rosmej, R. Sobierajski, F. Tavella, R. Thiele, J. Tiggesbäumker, S. Toleikis, T. Tschentscher, L. Vysin, T. J. Whitcher, S. White, and J. S. Wark. Electronic structure of an XUV photogenerated Solid-Density aluminum plasma. *Physical Review Letters*, 104:225001, June 2010.

[287] M. Volmer, C. Sternemann, J. S. Tse, T. Buslaps, N. Hiraoka, C. L. Bull, J. Gryko, P. F. McMillan, M. Paulus, and M. Tolan. Charge transfer in silicon clathrates studied by compton scattering. *Phys. Rev. B*, 76:233104, Dec 2007.

[288] A. von dem Borne, R. L. Johnson, B. Sonntag, M. Talkenberg, A. Verweyen, Ph. Wernet, J. Schulz, K. Tiedtke, Ch. Gerth, B. Obst, P. Zimmermann, and J. E. Hansen. *Physical Review A*, 62:052703, 2000.

[289] L. von Hamos. *Annalen der Physik*, 409:716, 1933.

[290] J. Vorberger and D.O. Gericke. Effective ionion potentials in warm dense matter. *High Energy Density Physics*, 9(1):178 – 186, 2013.

[291] Iradwikanari Waluyo, Congcong Huang, Dennis Nordlund, Uwe Bergmann, Thomas M. Weiss, Lars G. M. Pettersson, and Anders Nilsson. The structure of water in the hydration shell of cations from x-ray raman and small angle x-ray scattering measurements. *The Journal of Chemical Physics*, 134(6):064513, 2011.

[292] Iradwikanari Waluyo, Dennis Nordlund, Uwe Bergmann, Lars G. M. Pettersson, and Anders Nilsson. Increased fraction of weakened hydrogen bonds of water in aerosol OT reverse micelles. *The Journal of Chemical Physics*, 131(3):031103, 2009.

[293] Sanwu Wang. Generalization of the thomas-reiche-kuhn and the bethe sum rules. *Phys. Rev. A*, 60:262–266, Jul 1999.

[294] P Wernet, D Nordlund, U Bergmann, M Cavalleri, M Odelius, H Ogasawara, LA Naslund, TK Hirsch, L Ojamae, P Glatzel, LGM Pettersson, and A Nilsson. The structure of the first coordination shell in liquid water. *Science*, 304(5673):995–999, 2004.

[295] M. West, A. T. Ellis, P. Kregsamer, P. J. Potts, C. Streli, C. Vanhoof, and P. Wobrauschek. Atomic spectrometry update. x-ray fluorescence spectrometry. *Journal of Analytical Atomic Spectrometry*, 22(10):1304, 2007.

[296] M. West, A. T. Ellis, P. Kregsamer, P. J. Potts, C. Streli, C. Vanhoof, and P. Wobrauschek. Atomic spectrometry update. x-ray fluorescence spectrometry. *Journal of Analytical Atomic Spectrometry*, 23(10):1409, 2008.

[297] Hugh F. Wilson and Burkhard Militzer. Rocky core solubility in jupiter and giant exoplanets. *Phys. Rev. Lett.*, 108:111101, Mar 2012.

[298] H. Yamaoka, M. Oura, M. Taguchi, T Morikawa, K. Takahiro, A. Terai, K. Kawatsura, A. M. Vlaicu, Y. Ito, and T. Mukoyama. *J. Phys. Soc. Japan*, 73:3182, 2004.

[299] U. Zastrau, P. Audebert, V. Bernshtam, E. Brambrink, T. Kämpfer, E. Kroupp, R. Loetzsch, Y. Maron, Yu. Ralchenko, H. Reinholz, G. Röpke, A. Sengebusch, E. Stambulchik, I. Uschmann, L. Weingarten, and E. Förster. Temperature and $k\alpha$-yield radial distributions in laser-produced solid-density plasmas imaged with ultrahigh-resolution x-ray spectroscopy. *Phys. Rev. E*, 81:026406, Feb 2010.

[300] G.B. Zimmerman and R.M. More. Pressure ionization in laser-fusion target simulation. *Journal of Quantitative Spectroscopy and Radiative Transfer*, 23(5):517 – 522, 1980.